

THE DETECTABILITY OF  
HABITABLE EXOMOONS WITH  
KEPLER

A THESIS SUBMITTED TO THE UNIVERSITY OF MANCHESTER  
FOR THE DEGREE OF MASTER OF SCIENCE  
IN THE FACULTY OF ENGINEERING AND PHYSICAL SCIENCES

2012

By

Supachai Awiphan

School of Physics and Astronomy

# Contents

|   |           |
|---|-----------|
| <b>Abstract</b>   | <b>10</b> |
| <b>Declaration</b>                                      | <b>11</b> |
| <b>Copyright</b>  | <b>12</b> |
| <b>Acknowledgements</b>                                 | <b>13</b> |
| <b>The Author</b>                                       | <b>15</b> |
| <b>Abbreviations</b>                                    | <b>16</b> |
| <b>1 Introduction</b>                                   | <b>17</b> |
| <b>2 Habitable exoplanets and exomoons</b>              | <b>18</b> |
| 2.1 Historical background . . . . .                     | 18        |
| 2.2 Exoplanet detection methods . . . . .               | 19        |
| 2.2.1 Methods of detecting hot planets . . . . .        | 20        |
| 2.2.2 Methods of detecting cold planets . . . . .       | 21        |
| 2.2.3 Other detection methods . . . . .                 | 24        |
| 2.3 Habitable exoplanets . . . . .                      | 26        |
| 2.3.1 Habitable zone . . . . .                          | 26        |
| 2.3.2 The Earth Similarity Index (ESI) . . . . .        | 28        |
| 2.3.3 The possibility of habitable exoplanets . . . . . | 29        |
| 2.4 Exomoon background and detection methods . . . . .  | 29        |
| 2.5 Habitable exomoons . . . . .                        | 31        |

|          |   |            |
|----------|---|------------|
| <b>3</b> | <b>Transiting technique and application</b>                                 | <b>35</b>  |
| 3.1      | Transiting exoplanets . . . . .   | 35         |
| 3.2      | Timing variation detection techniques . . . . .                             | 37         |
| 3.3      | TTV and TDV exomoon detection techniques . . . . .                          | 38         |
| 3.3.1    | Transit Timing Variation (TTV) . . . . .                                    | 38         |
| 3.3.2    | Transit Duration Variation (TDV) . . . . .                                  | 42         |
| 3.4      | Exoplanet transit surveys . . . . .   | 44         |
| 3.4.1    | Ground-based surveys . . . . .  | 44         |
| 3.4.2    | Space missions . . . . .  | 45         |
| 3.5      | The detectability of exomoons with <i>Kepler</i> class photometry . . . . . | 48         |
| <b>4</b> | <b>Generating and analysing light curve</b>                                 | <b>51</b>  |
| 4.1      | Planet-moon orbit . . . . .   | 51         |
| 4.2      | Planetary transit light curve . . . . .                                     | 56         |
| 4.3      | Planet-moon transit light curve . . . . .                                   | 60         |
| 4.4      | <i>Kepler</i> photometry . . . . .  | 68         |
| 4.5      | Modelling habitable exomoons . . . . .                                      | 70         |
| 4.5.1    | Properties of the host star . . . . .                                       | 71         |
| 4.5.2    | Properties of the host planet . . . . .                                     | 74         |
| 4.5.3    | Properties of the exomoon . . . . .   | 75         |
| 4.6      | Measuring TTV-TDV signals . . . . .   | 76         |
| 4.7      | TTV-TDV correlation testing . . . . .                                       | 77         |
| <b>5</b> | <b>Results and discussion</b>   | <b>82</b>  |
| 5.1      | Detectability of habitable exomoons . . . . .                               | 82         |
| 5.2      | Analysing the correlation structure . . . . .                               | 90         |
| 5.3      | Improving the detectability with long-term observation . . . . .            | 99         |
| <b>6</b> | <b>Conclusion and further work</b>  | <b>102</b> |
| 6.1      | Improvement to simulation . . . . .   | 102        |
| 6.2      | Conclusion . . . . .  | 103        |

A List of parameters 112

B Program 117

**Word count: 28,699**

# List of Tables

|     |   |     |
|-----|---|-----|
| 4.1 | Limb-darkening occultation. . . . .   | 59  |
| 4.2 | Moon active transit component. . . . .  | 62  |
| 4.3 | The actively transiting area of planet and moon. . . . .  | 63  |
| 4.4 | Moon active transit component of Case 14. . . . .   | 68  |
| 4.5 | <i>Kepler</i> photometry properties. . . . .  | 70  |
| 4.6 | The number of highest priority <i>Kepler</i> target stars as a function of<br>effective temperature and apparent magnitude. . . . . | 72  |
| 5.1 | Input parameters for the simulation. . . . .  | 83  |
| 5.2 | The ratios between moon period and planet period. . . . .   | 99  |
| 5.3 | Input parameters for the long-term observation simulation. . . . .  | 100 |
| A.1 | List of important parameters . . . . .  | 112 |

# List of Figures

|     |   |    |
|-----|---|----|
| 2.1 | Observational data of the first detection of an exoplanet via radial velocity technique, 51 Peg b. . . . .                  | 20 |
| 2.2 | Observational data of the first detection of an exoplanet via transit technique, HD 209458b. . . . .                        | 22 |
| 2.3 | The first image of an extra-solar planet, 2M1207b. . . . .  | 23 |
| 2.4 | Observational data of the first detection of exoplanets via pulsar timing technique, PSR 1257+12B and PSR 1257+12C. . . . . | 24 |
| 2.5 | The GHZ in the disk of the Milky Way. . . . .   | 28 |
| 2.6 | The diagram compares the Solar System to Kepler-22 system. . . . .  | 30 |
| 3.1 | Transiting light curve with four contact points and three main parameters. . . . .  | 36 |
| 3.2 | Variation of TTV and TDV signals due to planet and moon positions. . . . .  | 39 |
| 3.3 | The side-on view of the star-planet-moon system. . . . .  | 41 |
| 3.4 | The value of $\Upsilon^{-1}$ versus the planet's position of pericentre, $\varpi_p$ . . . . .                               | 41 |
| 3.5 | The TTV and TDV signal simulated from 1 Earth-mass exomoon orbiting GJ436b. . . . .   | 44 |
| 3.6 | <i>Kepler</i> spacecraft. . . . .   | 46 |
| 3.7 | Planet detection capability of <i>Euclid</i> . . . . .  | 47 |
| 3.8 | The TTV detectability of a $0.2 M_{\oplus}$ exomoon in G2V system around a Jupiter, Saturn and Neptune-like planet. . . . . | 49 |
| 3.9 | The lowest detectable exomoon mass orbiting a Saturn-like planet. . . . .   | 50 |
| 4.1 | Euler angles diagram. . . . .   | 53 |

|      |   |    |
|------|---|----|
| 4.2  | Orbital elements of a transiting planet-star system. . . . .  | 53 |
| 4.3  | Geometry of limb darkening. . . . .   | 57 |
| 4.4  | Diagrams of cases 1-27. . . . .   | 65 |
| 4.5  | Diagrams of cases 14. . . . .   | 66 |
| 4.6  | Decision flow chart of Case 14. . . . .   | 67 |
| 4.7  | Instrument noise, photon noise, stellar variability and total noise of<br><i>Kepler</i> class photometry as a function of apparent magnitude of stars.  | 69 |
| 4.8  | The occurrence of planets with period less than 50 days as a function<br>of stellar effective temperature. . . . .  | 73 |
| 4.9  | The occurrence of planets with radii of 2-32 $R_{\oplus}$ as a function of orbital<br>period. . . . .   | 73 |
| 4.10 | Scatter plot between effective temperature and metallicity for neigh-<br>bouring stars and confirmed giant planet hosts. . . . .  | 74 |
| 4.11 | Planetary radii of coreless planets and planets with a core of 25 $M_{\oplus}$<br>of heavy elements at 4.5 Gyr as a function of orbital distance from<br>the Sun. . . . .   | 75 |
| 4.12 | Planetary radii of rocky planets as a function of masses. . . . .   | 76 |
| 4.13 | Light curves of a 15 $M_{\oplus}$ habitable-zone planet with a 10 $M_{\oplus}$ moon<br>for an M2 host star with planet period 89.35 days and moon period<br>2.24 days. . . . .  | 78 |
| 4.14 | TTV signal, TDV signal and the plots between $TTV^2$ and $TDV^2$ of<br>a 10.0 $M_{\oplus}$ exomoon around 15.0-150.0 $M_{\oplus}$ exoplanet for M-Dwarf<br>star, with planet period 89.35 days and moon period 2.24 days. . . . | 81 |
| 5.1  | Correlation and variance of correlation contours between planet mass<br>and moon mass of the light curves without <i>Kepler</i> photometric noise.  | 83 |
| 5.2  | Correlation and variance of correlation contours between planet sep-<br>aration and moon period of the light curves without <i>Kepler</i> photo-<br>metric noise. . . . .   | 84 |

|      |  |    |
|------|--|----|
| 5.3  | Correlation and variance of correlation contours between planet mass and planet separation of the light curves without <i>Kepler</i> photometric noise. . . . .                                | 84 |
| 5.4  | Correlation and variance of correlation contours between moon mass and planet separation of the light curves without <i>Kepler</i> photometric noise. . . . .                                  | 85 |
| 5.5  | Correlation and variance of correlation contours between planet mass and moon period of the light curves without <i>Kepler</i> photometric noise.  | 85 |
| 5.6  | Correlation and variance of correlation contours between moon mass and moon period of the light curves without <i>Kepler</i> photometric noise.  | 86 |
| 5.7  | Correlation and variance of correlation contours between planet mass and moon mass of the light curves with <i>Kepler</i> photometric noise. . .   | 86 |
| 5.8  | Correlation and variance of correlation contours between planet separation and moon period of the light curves with <i>Kepler</i> photometric noise. . . . .                                   | 87 |
| 5.9  | Correlation and variance of correlation contours between planet mass and planet separation of the light curves with <i>Kepler</i> photometric noise.   | 87 |
| 5.10 | Correlation and variance of correlation contours between moon mass and planet separation of the light curves with <i>Kepler</i> photometric noise.   | 88 |
| 5.11 | Correlation and variance of correlation contours between planet mass and moon period of the light curves with <i>Kepler</i> photometric noise. .   | 88 |
| 5.12 | Correlation and variance of correlation contours between moon mass and moon period of the light curves with <i>Kepler</i> photometric noise. .   | 89 |
| 5.13 | Correlation and variance of correlation contours between planet mass and moon mass of the light curves with <i>Kepler</i> photometric noise, excluding zero-value correlation. . . . .         | 91 |
| 5.14 | Correlation and variance of correlation contours between planet separation and moon period of the light curves with <i>Kepler</i> photometric noise, excluding zero-value correlation. . . . . | 91 |

|      |  |     |
|------|--|-----|
| 5.15 | Correlation and variance of correlation contours between planet mass and planet separation of the light curves with <i>Kepler</i> photometric noise, excluding zero-value correlation. . . . . | 92  |
| 5.16 | Correlation and variance of correlation contours between moon mass and planet separation of the light curves with <i>Kepler</i> photometric noise, excluding zero-value correlation. . . . .   | 92  |
| 5.17 | Correlation and variance of correlation contours between planet mass and moon period of the light curves with <i>Kepler</i> photometric noise, excluding zero-value correlation. . . . .       | 93  |
| 5.18 | Correlation and variance of correlation contours between moon mass and moon period of the light curves with <i>Kepler</i> photometric noise, excluding zero-value correlation. . . . .         | 93  |
| 5.19 | The correlation plots of planet separation versus planet mass contours of the light curves with <i>Kepler</i> photometric noise. . . . .   | 95  |
| 5.20 | The variance of correlation plots of planet separation versus planet mass contours of the light curves with <i>Kepler</i> photometric noise. . . . .   | 96  |
| 5.21 | The correlation plots of planet separation versus moon mass contours of the light curves with <i>Kepler</i> photometric noise. . . . .   | 97  |
| 5.22 | The variance of correlation plots of planet separation versus moon mass contours of the light curves with <i>Kepler</i> photometric noise. . . . .   | 98  |
| 5.23 | Correlation and variance of correlation contours between planet mass and planet separation of the long-term simulation light curves with <i>Kepler</i> photometric noise. . . . .              | 101 |
| 5.24 | Correlation and variance of correlation contours between moon mass and planet separation of the long-term simulation light curves with <i>Kepler</i> photometric noise. . . . .                | 101 |

# Abstract

Over 750 extrasolar planets have been discovered, but none of them have detected moons around them. From recent studies, the applications of transit exoplanet detection techniques called Transit Timing Variation (TTV) and Transit Timing Duration (TDV) have been proposed to use for exomoon detection. Furthermore, from the success of the *Kepler* mission, the number of transiting exoplanets has increased rapidly. Therefore, investigating the detectability of exomoons via TTV and TDV with the *Kepler* mission is timely. In this dissertation, the detectability of a habitable-zone exomoon orbiting around a giant planet in M-Dwarf system is investigated. Light curves of 146,410 systems with various configurations were simulated around M-Dwarf hosts of mass  $0.5 M_{\odot}$  and radius  $0.55 R_{\odot}$ . Jupiter-like giant planets which offer the best potential for hosting habitable exomoons were considered with rocky Earth-mass moons. The detectability is measured by using the phase-correlation between TTV and TDV signals. The *Kepler* photometric noise is all accounted for in the analysis in order to find the exomoon detectability. From simulation results, super-Earth-size habitable exomoons in M-Dwarf systems may be detectable with *Kepler*. The detectability depends on the intensity of the TDV signal more than the TTV signal. High-mass moons orbiting low-mass planets should be the best candidates for detection. However, under certain conditions, aliasing in between the planet period and the moon period may prevent exomoon detection, due to incomplete moon phase information.

University of Manchester,

**Supachai Awiphan**

Master of Science

The detectability of habitable exomoons with *Kepler*

23 August 2012

# Declaration

No portion of the work referred to in the thesis has been submitted in support of an application for another degree or qualification of this or any other university or other institute of learning.

# Copyright

i. The author of this thesis (including any appendices and/or schedules to this thesis) owns certain copyright or related rights in it (the “Copyright”) and s/he has given The University of Manchester certain rights to use such Copyright, including for administrative purposes.

ii. Copies of this thesis, either in full or in extracts and whether in hard or electronic copy, may be made only in accordance with the Copyright, Designs and Patents Act 1988 (as amended) and regulations issued under it or, where appropriate, in accordance with licensing agreements which the University has from time to time. This page must form part of any such copies made.

iii. The ownership of certain Copyright, patents, designs, trade marks and other intellectual property (the “Intellectual Property”) and any reproductions of copyright works in the thesis, for example graphs and tables (“Reproductions”), which may be described in this thesis, may not be owned by the author and may be owned by third parties. Such Intellectual Property and Reproductions cannot and must not be made available for use without the prior written permission of the owner(s) of the relevant Intellectual Property and/or Reproductions.

iv. Further information on the conditions under which disclosure, publication and commercialisation of this thesis, the Copyright and any Intellectual Property and/or Reproductions described in it may take place is available in the University IP Policy (see <http://documents.manchester.ac.uk/DocuInfo.aspx?DocID=487>), in any relevant Thesis restriction declarations deposited in the University Library, The University Library’s regulations (see <http://www.manchester.ac.uk/library/aboutus/regulations>) and in The University’s policy on Presentation of Theses.

# Acknowledgements

This dissertation would not have been possible without the guidance and help of several people. First of all, I would like to thank my beloved country Thailand and acknowledge the Royal Thai Government Scholarship who fully sponsored my Master study at the University of Manchester.

I would like to express my deepest gratitude and indebtedness to my supervisor, Dr. Eamonn Kerins, for his guidance, encouragement and support throughout my Master degree, and for suggesting this interesting project in September, 2011.

I sincerely thank Dr. David Kipping for his guidance in statistical analysis and valuable suggestions with regard to this dissertation. I also like to extend my appreciation to the JBCA exoplanet group, Dr. Iain McDonald and Matthew Penny, for their very valuable suggestions and help.

My sincere appreciation is extended to all the other MSc by Research in Astronomy and Astrophysics students for their kindness and sympathy, and special thanks to course director, Dr. Clive Dickinson, and my advisor, Prof. Albert Zijlstra, for their support during this study. I also wish to thank all the staff and students at JBCA who were very friendly and helpful.

I am extremely grateful to Prof. Boonrucksar Soonthornthum and Dr. Siramas Komonjinda, director of National Astronomical Research Institute of Thailand (NARIT) and my ex-supervisor at Chiang Mai University, Thailand, respectively, who advised me to study at the University of Manchester and always support me. I would also like to express my gratitude to several supportive people back home in Thailand.

Last but not the least I would like to thank and share the honour of having

completed this dissertation with my loving family in gratitude for their unending support and encouragement. Without their support this work would not have been possible.

Finally, I would like to thank everybody who was important to the success of this dissertation, as well as expressing my apology that I could not mention them all personally one by one.

# The Author

The author was born in Thailand and graduated with a Bachelor of Science in Physics (First Class Honours) from Chiang Mai University, Thailand, in 2010. After finishing his undergraduate period, he was awarded a full scholarship from the Royal Thai Government to study in Master degree and Ph.D. in United Kingdom. He commenced studying for a M.Sc. by Research (Astronomy and Astrophysics) in September 2011 at the University of Manchester, the research aspects of which are presented in dissertation. The author's future career plans are to undertake a Ph.D. at the University of Manchester and pursue a career as a researcher at National Astronomical Research Institute of Thailand (NARIT).

# Abbreviations

|       |   |   |
|-------|---|---|
| AU    | : | Astronomical Unit                                 |
| CCD   | : | Charge-coupled device                             |
| CoRoT | : | Convection, Rotation and planetary Transits       |
| EChO  | : | Exoplanet CHaracterisation Observatory            |
| ESA   | : | The European Space Agency                         |
| ESI   | : | Earth Similarity Index                            |
| FOV   | : | Field of view                                     |
| FUV   | : | Far Ultraviolet                                   |
| GHZ   | : | Galactic Habitable Zone                           |
| HAT   | : | Hungarian-made Automated Telescope                |
| HZ    | : | Habitable Zone                                    |
| MOA   | : | Microlensing Observations in Astrophysics         |
| NASA  | : | The National Aeronautics and Space Administration |
| NIR   | : | Near infrared                                     |
| NISP  | : | Near infrared instrument                          |
| OGLE  | : | Optical Gravitational Lensing Experiment          |
| PHI   | : | Planetary Habitability Index                      |
| RMS   | : | Root Mean Square                                  |
| TDV   | : | Transit Duration Variation                        |
| TIP   | : | Transit Impact Parameter                          |
| TOA   | : | Time-of-arrival                                   |
| TTV   | : | Transit Timing Variation                          |
| V     | : | Velocity  |
| VIS   | : | Visual instrument                                 |
| WASP  | : | Wide Angle Search for Planets                     |

# Chapter 1

## Introduction

Today the search for and study of exoplanets is one of the most dynamic research fields of modern astronomy. Over the last decade, our knowledge of extrasolar planets has grown rapidly, not only in the development of different methods to detect them, but also in the understanding of their formation and evolution. The number of detected exoplanets continues to increase steadily. At present, more than 750 planets have been confirmed<sup>1</sup>. As the number of detected exoplanets continues to grow, the potential for detecting satellites orbiting them has become of increasing interest. The best instrument up to this challenge is *Kepler* which is designed to detect small transiting exoplanets with its highly sensitive photometric camera.

In this work, the detectability of habitable exomoons with *Kepler* is assessed. The structure of the dissertation is as follows. In Chapter 2, a historical background of habitable extrasolar planets and moons with various detection techniques, such as radial velocity, transit and microlensing is provided. In Chapter 3, the transiting exoplanet detection technique with its application to detect exomoons is described. The light curve of an exoplanet with an exomoon is described in Chapter 4. The last part of the Chapter is dedicated to analysing the detectability of habitable exomoons with *Kepler* using a detailed numerical simulation. In Chapter 5, simulation results are presented and analysed. Finally, conclusion and further work are discussed in Chapter 6.

---

<sup>1</sup>See <http://exoplanet.eu/>

# Chapter 2

## Habitable exoplanets and exomoons

### 2.1 Historical background

Exoplanets (planets outside the Solar System) are objects of interest for astronomers, because of the potential that living things exist on them. More than 750 planets have been detected by both ground-based and space-based telescopes, including some super-Earth planets (planets with masses between 1 and  $10 M_{\oplus}$ ) which have potential to support life. After NASA launched the *Kepler* space telescope in 2009, the number of planet candidates increased further. The *Kepler* Science Team announced more than 1,200 planet candidates in early 2011 (Borucki et al., 2011a) and added more than 1,000 additional candidates in 2012 (Batalha et al., 2012).

The first published, confirmed discovery was made in 1992 by Wolszczan & Frail. They announced the discovery of planets around a pulsar, PSR 1257+12 (Wolszczan & Frail, 1992). In 1995, Mayor & Queloz announced the first exoplanets orbiting a solar-type star, 51 Peg, using the radial velocity method (Mayor & Queloz, 1995). The first low-mass planets orbiting a solar analogue were found in 2004, 55 Cnc e ( $8.3 M_{\oplus}$ ) (McArthur et al., 2004) and  $\mu$  Ara c ( $10.5 M_{\oplus}$ ) (Santos et al., 2004).

Following on from the discoveries in the 1990s, several different methods have

been developed to discover exoplanets, including gravitational microlensing and direct imaging. To date, the majority of the detected exoplanets have been found using the radial velocity technique. However, the radial velocity method can only obtain orbital parameters and minimum mass. In order to obtain physical parameters, such as exact mass, radius and mean density, additional data from transit and the other methods are often used (Udry & Santos, 2007).

One of the main aims of studying extra-solar planets is to discover habitable exoplanets or exomoons. Habitable planets or moons may be located in the habitable zone (HZ) which was proposed for the first time by Huang (1959). At present, super-Earths located in HZ have been detected, e.g. Gliese 581c (Udry et al., 2007), Gliese 581d (Mayor et al., 2009), HD 85512b (Pepe et al., 2011) and Kepler 22b (Borucki et al., 2012).

## 2.2 Exoplanet detection methods

Exoplanets are objects which are very difficult to detect because they have extremely low emission light compared to their host stars. In order to detect exoplanets, a number of techniques have been developed.

In this work, the detection techniques are separated into three main groups, methods of detecting hot planets, methods of detecting cold planets and other detection methods, such as pulsar timing and astrometry. We define hot and cold planets by using the snow line. The snow line is a particular distance from the star where solid ice grains condense from hydrogen compounds. It divides the system into two regions. On the inside of the snow line, there is a volatile-poor (lack of substances with a low boiling-point) region with rocky planets, and outside of it, a volatile-rich region filled with icy components. Therefore, the snow line can be used to define the boundary between the hot rocky planets and cold gas giant planets (Lin, 2008).

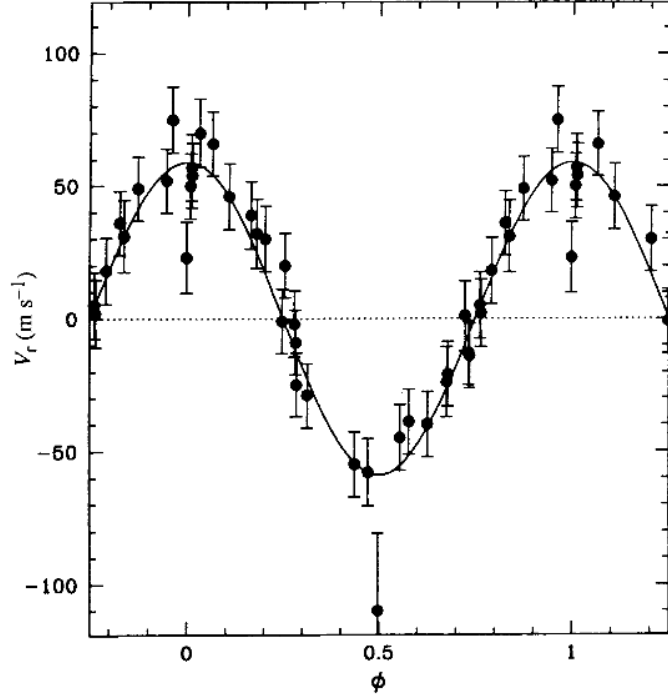


Figure 2.1: Original data of 51 Peg shows variation in orbital motion due to 51 Peg b’s gravitational interaction (Mayor & Queloz, 1995).

## 2.2.1 Methods of detecting hot planets

### Radial velocity

Radial velocity is a technique which detects the star wobble around the system centre-of-mass due to the gravitational interaction of nearby planets. The motion of the star produces the change in velocity along the line-of-sight of the star which causes the periodic shift of absorption lines in the star’s spectrum. It favours massive planets which have a short orbital period, because of the higher amplitude of the radial velocity signal. The amplitude of the radial velocity signal,  $K_*$ , of a star of mass  $M_*$  with planet of mass  $M_p$  orbiting around with period  $P_p$ , is defined by,

$$K_* = \frac{M_p \sin i_p}{M_*} \frac{2\pi a_p}{P_p}, \quad (2.1)$$

where  $a_p$  is the planet separation and  $i_p$  is the orbital inclination of planet. The radial velocity technique has a disadvantage of not being able to provide all information about planets, because it cannot determine the true mass of planets, but can estimate their minimum mass,  $M_p \sin i_p$ . However, this method has proven

to be a successful extra-solar planet detection technique, because it has detected most of the exoplanets discovered from the ground. Since the first detection of an exoplanet via radial velocity in 1995, 51 Peg b, more than 400 planets have been discovered by using this method (Figure 2.1) (Mayor & Queloz, 1995).

Nowadays, with improvements in the sensitivity of the technique and instruments, it can reach a precision of  $1 \text{ m.s}^{-1}$  which can detect close-in planets with masses less than  $2 M_{\oplus}$  and it will detect sub-Earth mass planets in the near future (Mayor et al., 2011).

## Transit

Transit photometry is a method which looks for a periodic dip in the stellar light curve. When a planet passes in front of its host star in the direction of the observer line-of-sight, the star flux temporarily decreases due to blocking by the planet (Section 3.1).

From transit observations, not only orbital parameters but also physics parameters are obtained. However, the transit technique has the problem of a large number of false-positive detections caused by grazing eclipsing binaries, low-mass stellar objects or blended stellar systems (Díaz et al., 2011). In 2000, Charbonneau et al. and Henry et al. detected the first transit exoplanet, HD 209458b, which is a hot-Jupiter (Figure 2.2) (Charbonneau et al., 2000; Henry et al., 2000).

### 2.2.2 Methods of detecting cold planets

#### Gravitational microlensing

Gravitational microlensing was proposed by Mao & Paczynski in 1991. It is the only known method capable of discovering planets at truly great distances from the Earth. It can find planets orbiting stars near the centre of the Galaxy, thousands of light-years away, whereas radial velocity and transit methods can detect planets only in our galactic neighbourhood. Microlensing is most sensitive to cold planets, in outer regions of systems beyond the snow line (Kennedy & Kenyon, 2008; Lecar

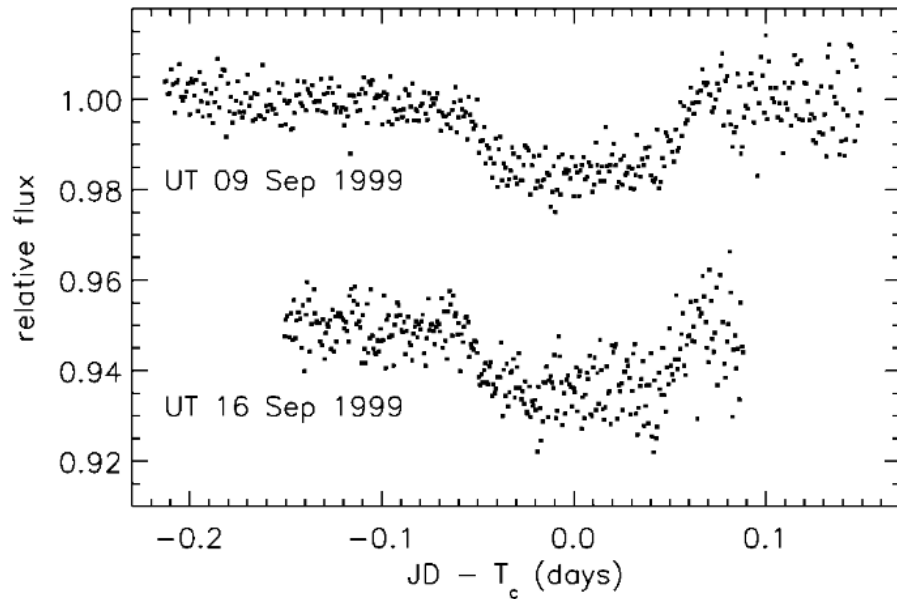


Figure 2.2: Observational data of the photometric dimming of HD 209458, the first transit exoplanet system (Charbonneau et al., 2000).

et al., 2006). Furthermore, microlensing is the only method which can detect free-floating planets.

Microlensing is based on the gravitational lens effect. A microlensing event occurs when a lensing star moves in front of the source star in the direction of the observer line-of-sight. The light paths of the source are bent by the lensing star and focused by the lensing which can magnify and demagnify the image of the source star. If the lensing star has a planet orbiting around it, the planet can perturb the light and lead to additional spikes in the light curve (Mao & Paczynski, 1991).

The first planet which was discovered using microlensing was OGLE 2003-BLG-235/MOA 2003-BLG-53 in 2004 (Bond et al., 2004). Currently, more than 15 planets have been detected using this method, including a Neptune mass ratio planetary companion to the lens star (Gould et al., 2006). However, the number of planet detections using microlensing will increase in the future due to the ongoing main microlensing surveys, MOA (Bond et al., 2002) and OGLE (Udalski et al., 2008).

### Direct imaging

Direct imaging is a one of the oldest techniques which directly detects planets through an image. It seems to be the easiest technique, but in reality, it is one of

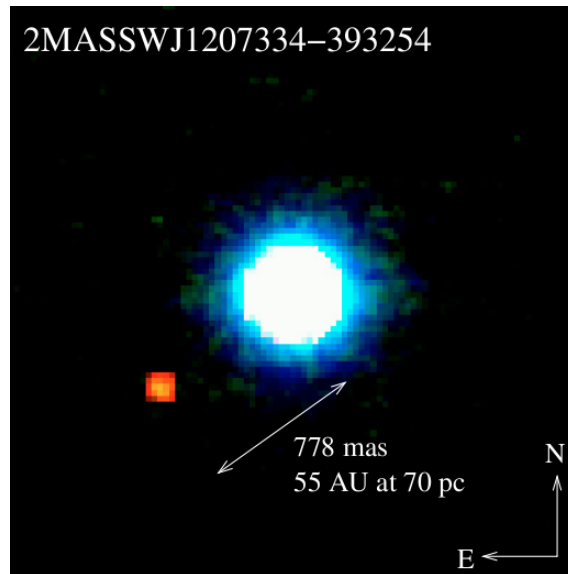


Figure 2.3: The first image of an extra-solar planet, 2M1207b, orbiting 2MASSWJ 1207334-393254 brown dwarf star (Chauvin et al., 2004).

the hardest techniques. It is challenging for two main reasons. First, the planets are extremely faint light sources compared to their host stars. Second, the planets are generally located very close to their parent stars. Currently, special techniques such as coronagraphy and adaptive optics are used to implement this method. They are sensitive to distant hot planets around young, nearby stars which are uncommon (Masciadri & Raga, 2004; Nielsen et al., 2008).

The advantage of direct imaging is it provides interesting information about the planet, including the planet's exact orbital parameters and surface properties. Spectroscopic data could yield information about the chemical composition of the planet's atmosphere or even biological activity.

Chauvin et al. (2004) discovered the first directly imaged exoplanet, 2M1207b, orbiting brown dwarf, 2MASSWJ 1207334-393254 (Figure 2.3). The planet has a mass of 5 Jupiter mass with temperature in the range 1100-1300K (Chauvin et al., 2005). Currently, this technique has detected more than 30 planets, including a multi-planet system, HR 8799 (Marois et al., 2008).

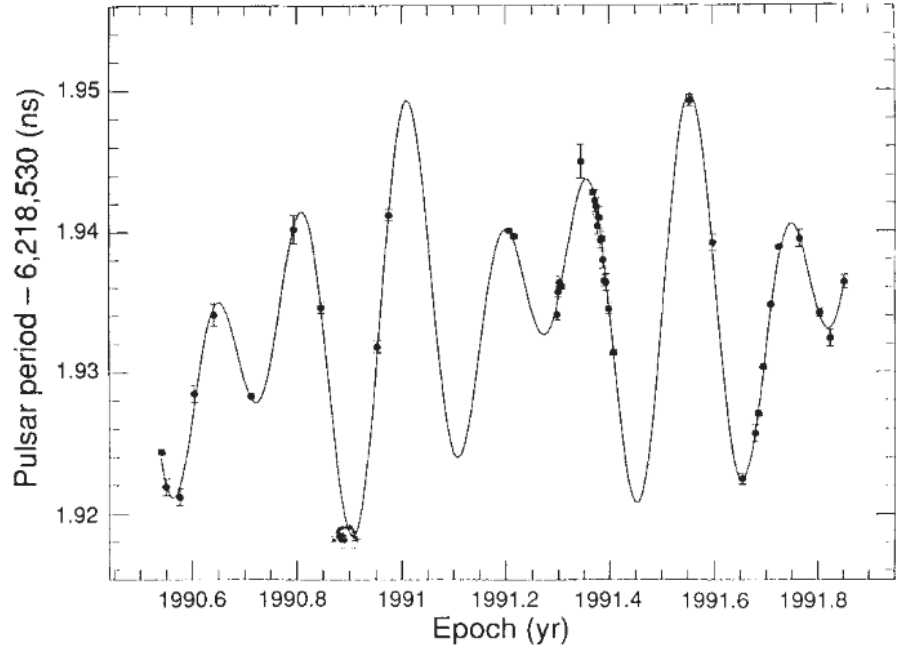


Figure 2.4: Data of pulsar, PSR 1257+12, shows the variation in period due to the interaction of the first two detected exoplanets (Wolszczan & Frail, 1992).

### 2.2.3 Other detection methods

#### Pulsar Timing

The first detection of exoplanets, PSR 1257+12B and PSR 1257+12C was made in 1992 by using pulsar timing (Figure 2.4) (Wolszczan & Frail, 1992). Although this method was not originally designed for the detection of planets, it has a capability to detect smaller planets down to less than Earth’s mass.

The pulsar timing method uses the changing position of the pulsar, as a result of gravitational interaction. The change causes the distance and light travelling time between the pulsar and observer to change periodically and creates the change in time-of-arrival (TOA). TOA can be expressed as,

$$\Delta TOA = \frac{a_p M_p}{c M_*} \sin i_p, \quad (2.2)$$

where  $a_p$  is planet’s semi-major axis and  $c$  is the speed of light in the vacuum. However, since planets orbiting a pulsar are exotic objects and are presumably very rare, the chance of finding large numbers of planets with it seems small.

## Astrometry

Astrometry is one of the oldest astronomical techniques to search extrasolar planets. Ordinarily, it is used for detecting binary stars. This method uses the idea that the gravitational interaction between star and planet causes the star and planet to orbit around their barycentre. It measures a periodic variation in the position of the star on the plane of the sky, subtracting out the star's apparent motion due to the yearly parallax motion and the projection of its real proper motion through space.

The main advantage of the astrometry method is that it provides an accurate estimate of a planet's mass. The relation between the variation in the sky position,  $\alpha_a$ , can be written as,

$$\alpha_a = \frac{M_p a_p}{M_* D}, \quad (2.3)$$

where  $D$  is the distance from the Earth to the star. However, it is most effective when the orbital plane is "face on", or perpendicular to the observer's line of sight.

Strand (1943) and Reuhl & Holmberg (1943) announced the first planet orbiting the stars, 61 Cyg and 70 Oph, by using astrometry. However, the recent ground-based astrometry observation results show that the evidence for planets around 61 Cyg and 70 Oph has been proved incorrect (Heintz, 1978). Nowadays, there are some exoplanets that have their mass determined via the astrometry technique: Gliese 876b (Benedict et al., 2002) HD 136118b (Martini et al., 2010) and HD 38529c (Benedict et al., 2010). However, the first extrasolar planet has been successfully detected astrometrically in 2010 (Bean et al., 2010b; Pravdo & Shaklan, 2009).

For future astrometry missions, SIMLite (Space Interferometry Mission), a NASA astrometric space-based observatory, has been developed to identify exoplanets via the astrometric technique (Unwin et al., 2008). However, in 2010, this mission was not recommended for development in this decade.

## 2.3 Habitable exoplanets

Over the past decade, more than 750 planets have been detected and analysed and more than 2,300 candidate planets have been added to the list by the *Kepler* space mission. In the next decade, attention will be switched from finding exoplanets to characterising them, such as searching for exomoons and analysing planetary atmospheres.

### 2.3.1 Habitable zone

The first definition of habitable zone (HZ) was defined by Huang (1959). The classical definition of circumstellar HZ was defined by Kasting et al. in 1993 as an annulus around a star where a terrestrial planet with an atmosphere can sustain large amounts of liquid water on its surface, a condition necessary for photosynthesis (Kasting et al., 1993).

For a HZ, the planet has to be located close enough to its host to maintain a surface temperature above 273 K and not be too close to initiate a runaway greenhouse condition. Additionally, its location should allow photodissociation of water vapour into hydrogen and oxygen, and loss of hydrogen into space.

If the HZ is defined simply as the distance of a star where the effective temperature is in the range of 0°C to 100°C, the planet's effective temperature,  $T_p$ , can be defined as,

$$L_* = 4\pi a_p^2 \sigma T_p^4, \quad (2.4)$$

where  $L_*$  is the star's bolometric luminosity and  $\sigma$  is Stefan-Boltzmann constant. For Earth-like planets in orbit around a Sun-like star, the HZ will persist for orbital distance between 0.7 and 1.2 AU. From a recent model of HZ proposed by Selsis et al. (2007), the inner  $r_{in}$  and outer  $r_{out}$  boundaries of the HZ in AU units are given by,

$$r_{in} = (r_{in\odot} - a_{in}T_{\star} - b_{in}T_{\star}^2) \left( \frac{L}{L_{\odot}} \right)^{\frac{1}{2}}, \quad (2.5)$$

and

$$r_{out} = (r_{out\odot} - a_{out}T_{\star} - b_{out}T_{\star}^2) \left( \frac{L}{L_{\odot}} \right)^{\frac{1}{2}}, \quad (2.6)$$

where  $r_{in\odot}$  is inner boundaries of the present Solar HZ,  $r_{out\odot}$  is outer boundaries of the present Solar HZ,  $T_{\star}$  is star effective temperature,  $L_{\star}$  is star luminosity,  $L_{\odot}$  is luminosity of the Sun,  $a_{in} = 2.7619 \times 10^{-5} \text{ AU.K}^{-1}$ ,  $b_{in} = 3.8095 \times 10^{-9} \text{ AU.K}^{-2}$ ,  $a_{out} = 1.3786 \times 10^{-4} \text{ AU.K}^{-1}$ ,  $b_{out} = 1.4286 \times 10^{-9} \text{ AU.K}^{-2}$ , and  $T_{\star} = T_{\odot} - 5700 \text{ K}$  (Selsis et al., 2007).

However, there are a number of factors which can alter the boundaries of HZ, such as chemical cycles or the greenhouse effect. This effect can be seen on Venus, which orbits at a distance of 0.72 AU and falls within the Sun's HZ, but it has an average surface temperature above 700K (Kasting et al., 1993).

Due to stellar evolution, the host star becomes brighter and hotter which shifts the HZ outward. The continuously habitable zone, which is the region located in the HZ for longer than 1 Gyr, is interesting because planets located in this region can sustain liquid water long enough for life to form and evolve (Kasting et al., 1993).

For high-mass stars, their HZs are much further and broader which could be the best candidates for finding habitable planets. However, emission in the far ultraviolet (FUV) band which is potentially damaging to life is observed in high-mass stars. Then, solar-like stars which have reasonably broad HZs and do not emit FUV are the best candidates. For low-mass stars, red dwarfs, they have the longest lifetimes. However, in their early age, they have strong magnetic activity and HZ planets could be tidally locked with their hosts. Therefore, if they can hold on to their atmosphere in the early age and are not tidally locked, planets around them could be habitable (Joshi et al., 1997).

Finally, the Galactic Habitable Zone (GHZ) proposed by Gonzalez et al. (2001). is considered. The GHZ is the region where planets can retain liquid water in the

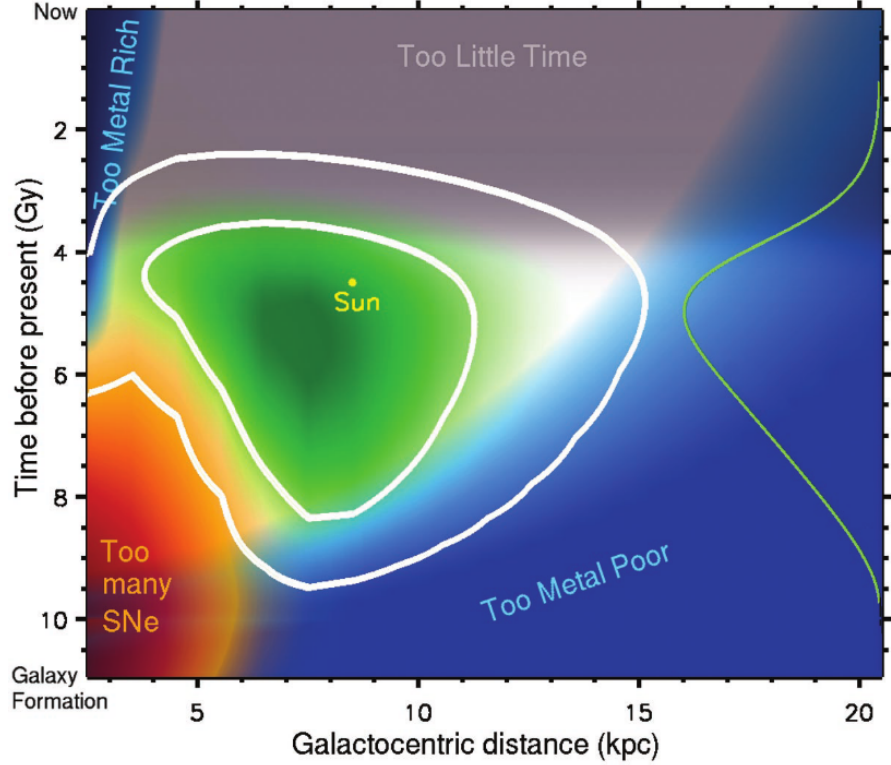


Figure 2.5: The GHZ in the disk of the Milky Way. The white contours encompass 68% (inner) and 95% (outer) of potentially suitable planetary systems (Lineweaver et al., 2004).

Milky Way galaxy. From a recent study, 10% of stars in the Milky Way are in the GHZ which defined as an annular region between 7 and 9 kpc from the galactic centre (Figure 2.5) (Lineweaver et al., 2004).

### 2.3.2 The Earth Similarity Index (ESI)

In 2011, Schulze-Makuch et al. proposed two classification schemes of exoplanet habitability called the Earth Similarity Index (ESI) and the Planetary Habitability Index (PHI) (Schulze-Makuch et al., 2011). We will focus only on the ESI classification due to lack of information on exoplanet PHI parameters. ESI is a multi-parameter measure of Earth-likeness as a number between 0 (no similarity) and 1 (Earth). The basic ESI expression is

$$ESI_{\varrho} = \left( 1 - \left| \frac{\varrho - \varrho_0}{\varrho + \varrho_0} \right| \right)^w, \quad (2.7)$$

where  $\varrho$  is planetary properties (mean radius, bulk density, escape velocity and

surface temperature),  $\varrho_0$  is a terrestrial reference value,  $w$  is a weight exponent (0.57 for the mean radius, 1.07 for the bulk density, 0.7 for the escape velocity and 5.58 for the surface temperature) and  $ESI_\varrho$  is the similarity. ESI can be separated into two values, interior (mean radius and bulk density) and surface (escape velocity and surface temperature) similarity. The single ESI value is obtained by using the geometric mean. The planets with an ESI value over 0.8 can be considered as Earth-like planets.

### 2.3.3 The possibility of habitable exoplanets

In 2007 the first terrestrial exoplanet in the HZ, Gliese 581c ( $5.34 M_\oplus$ ), was detected (Forveille et al., 2011; Udry et al., 2007). Its equilibrium temperature would be  $-3^\circ\text{C}$ , if its albedo is 0.64 (Venus-like), and  $40^\circ\text{C}$  for an Earth-like albedo, in which core liquid water may exist (Udry et al., 2007). However, if it has runaway greenhouse effect, its temperature should be over  $500^\circ\text{C}$  (von Bloh et al., 2007). In 2009, in the same system, Mayor et al. announced that planet Gliese 581d ( $6.06 M_\oplus$ ) is located in the HZ (Forveille et al., 2011; Mayor et al., 2009). Currently, 60 candidates have been found by *Kepler* in the temperature range suitable for habitation (Borucki et al., 2011a), including Kepler-22b, the planet found to orbit in the habitable zone of a star similar to our Sun (Figure 2.6) (Borucki et al., 2012).

Recent work by Mayor et al. shows that about half of solar-type stars are host to low-mass planets ( $<30 M_\oplus$ ). Furthermore, the planetary rate of 3-10 Earth-mass planets is estimated to be 10-16% in the  $\eta$ Earth survey and the HARPS-CORALIE survey (Mayor et al., 2011). From this result, low-mass planets seem to be very frequent around solar analogues, although few habitable extrasolar planets have been detected (Mayor et al., 2011; Pepe et al., 2011). Therefore, more habitable exoplanets should be detected in the future.

## 2.4 Exomoon background and detection methods

An exomoon is a natural satellite that orbits around an extrasolar planet. None

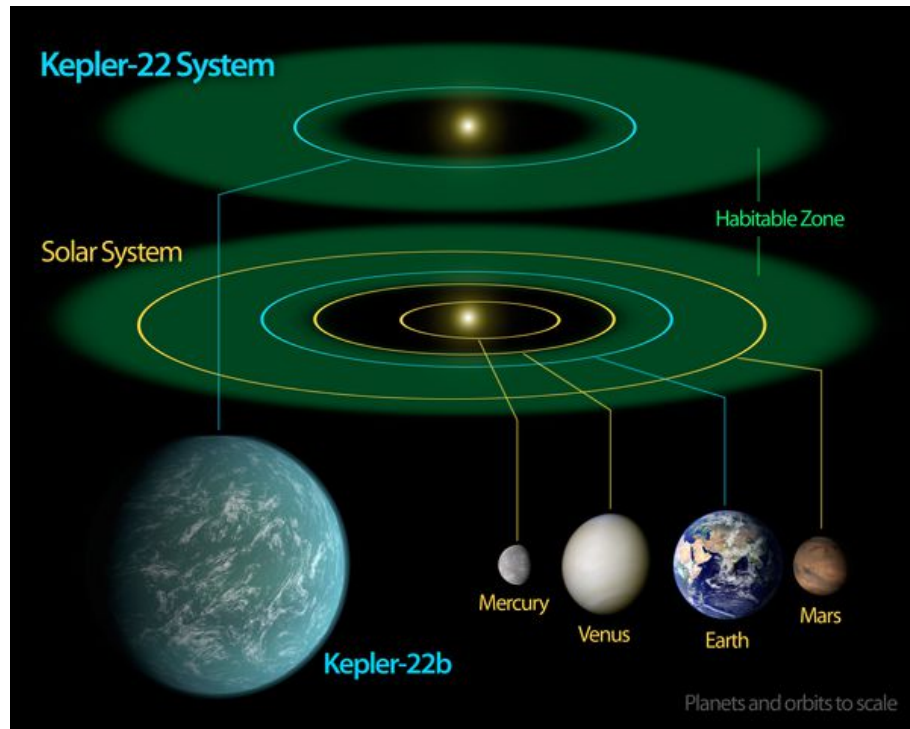


Figure 2.6: The diagram compares the Solar System to Kepler-22 system. The image is courtesy of NASA.

have been discovered to date. The information from the Solar system shows that many of the planets of the Solar system host satellites. In order to detect exomoons, several methods have been developed. Most possible methods for detecting exomoons are extensions of the exoplanet detection technique.

### Transit

The exomoon transit detection method is a method which detects the dip in stellar light curve due the moon passing in front of a host star (Simon et al., 2007). However, it is very challenging to confirm the exomoon signal from the observational data, because the dip may occur due to some form of photometric noise or star spot (Sartoretti & Schneider, 1999). Moreover, when the transit events occur, the exomoon could be behind or in front of the planet. Therefore, in order to detect an exomoon via the transit method, multiple transits events are required.

Although, exomoons are difficult to detect using transit method. TTV and TDV techniques which are the extensions of the transit method have been proposed to detect exomoon systems (Section 3.3). Exomoons should be detected with *Kepler* using

Transit Timing Variation (TTV) and Transit Duration Variation (TDV) methods from the simulation result by Kipping et al. (2009) (Section 3.5).

### **Direct imaging**

Direct imaging of exoplanets is extremely challenging due to the difference in brightness between host star and planet. Detecting exomoons using the direct imaging technique is more difficult, due to a tiny angular separation between the planet and moon. For the Earth-moon system at distance 10 pc, the separation is 0.5 milliarcseconds which is very small compared to the current best interferometric precision, around 25 milliarcseconds (Baines et al., 2007).

### **Microlensing**

Han & Han (2002) proposed that extrasolar moons could be detected using the microlensing technique. However, the problem that microlensing events cannot repeat poses a problem for this technique.

### **Pulsar timing**

The first exoplanet was discovered through the pulsar timing method. In 2008, Lewis et al. proposed that this technique should be able to detect a stable exomoon orbiting a pulsar planet. They applied this method to the case of PSR B1620-26b and found that exomoons with mass larger than 5% of the pulsar planet and a planet-moon separation of 2% of star-planet separation could be detected (Lewis et al., 2008).

## **2.5 Habitable exomoons**

The interest in exomoons comes from the proposition that moons are a factor that improves the probability of the existence of intelligent life on their host planets and the moons themselves also have a potential to host life. The Moon has a stabilising effect on Earth's axis and causes the tides on the Earth. Without the Moon, life on the Earth may be restricted to less complex forms (Laskar et al., 1993). A large

enough moon that can lock the planet and moon together may prevent tidal locking to the star. Moreover, if the mass of a moon is larger than  $0.12 M_{\oplus}$ , it could be habitable itself (Williams et al., 1997).

In 1997, Chyba and Williams et al. proposed the possibility of habitable exomoons. They posited that moons orbiting around giant gas planets' Hill sphere (the region of orbital stability) could host life (Chyba, 1997; Williams et al., 1997). Although moons orbiting giant planets at 1 AU from a solar analogue would become tidally locked within a few billion years after they form, their orbital period on timescales of a few days to a few months could cause temperature fluctuations on them.

Habitable moons need to be large enough to retain water and atmosphere. Although, the moons formed from the planetary disk are unlikely to be greater than 0.01% the mass of the host planet, the moons formed from captures or impacts (Triton and the Moon) have no limit on their mass (Canup & Ward, 2006). Barnes & O'Brien proposed that habitable exomoons should be Earth-like mass moons orbiting around habitable-zone Jupiter-like planets around M-dwarf stars (Barnes & O'Brien, 2002).

The HZ of exomoons can be defined simply as the distance where planets receive the same energy as the Earth,  $r_{hab}$ ,

$$r_{hab} = \sqrt{\frac{L_{*}}{L_{\odot}}} \text{ AU.} , \quad (2.8)$$

where  $L_{\odot}$  is the Sun's luminosity (Kipping et al., 2009). Furthermore, the moon can be lost from the planet due to three-body instability if the distance between the planet and moon is too large. To be retained by the planet, the moon must have an orbit that lies within the region called the Hill sphere. The Hill sphere approximates the gravitational sphere of influence of a smaller body, the planet. The radius of the sphere called the Hill radius ( $R_H$ ) is found by solving the three-body problem and is equal to the distance of the  $L_1$  and  $L_2$  Lagrangian points, which lie along the line of centres of the two bodies.

$$R_H = a_p \left( \frac{M_p}{3M_*} \right)^{1/3} . \quad (2.9)$$

For exomoon orbital eccentricity,  $e_m$ , and planetary eccentricity,  $e_p$ , Barnes & O'Brien (2002) and Domingos et al. (2006) approximated the stability for prograde moons as,

$$a_m = 0.36R_H , \quad (2.10)$$

and

$$a_m = 0.4895R_H(1.0000 - 1.0305e_p - 0.2738e_m) , \quad (2.11)$$

and for retrograde moons as

$$a_m = 0.50R_H , \quad (2.12)$$

and

$$a_m = 0.9309R_H(1.0000 - 1.0764e_p - 0.9812e_m) . \quad (2.13)$$

However, the Hill sphere is only an approximation, and other forces can eventually perturb an object out of the sphere. Therefore, in order to investigate habitable exomoons, the moons have to be stable long enough for life to form. The moons' orbits slowly change due to the perturbation on the orbits caused by the tidal bulge of the planets. On the moon with mass  $M_m$  and semi-major axis  $a_m$ , the tidal bulge causes the torque,

$$\tau_{p-m} = \frac{3}{2} \frac{k_{2p} G M_m^2 R_p^5}{Q_p a_m^6} \text{sgn}(n_p - n_m) , \quad (2.14)$$

where  $G$  is gravitational constant,  $R_p$  is planet radius,  $k_{2p}$  is the tidal Love number of the planets,  $Q_p$  is tidal dissipation parameter,  $\text{sgn}$  is the Signum function,  $n_p$  is the angular velocity of the planet's rotation and  $n_m$  is the angular velocity of

the moon's orbit (Murray & Dermott, 1999). For a Jupiter-like system,  $Q_p$  and  $k_{2p}$  are around  $10^5$  and 0.5 respectively (Barnes & O'Brien, 2002; Kipping et al., 2009).

Additionally, the total lifetime of a moon,  $T_{p-m}$  is defined by the time necessary for the moon orbit in the region between the critical semi-major axis ( $a_{crit}$ ) and the planet's surface ( $a_m$ ) (Barnes & O'Brien, 2002).

$$T_{p-m} = \frac{2}{13} (a_{crit}^{13/2} - a_p^{13/2}) \frac{Q_p}{3k_{2p}M_m R_p^5} \sqrt{\frac{M_p}{G}}. \quad (2.15)$$

In a recent study, Porter & Grundy used the Kocai Cycle and Tidal Friction model to simulate captured exomoons around giants and found that exomoons could stabilise in a few million years, which is very short relative to the life time of the stars (Porter & Grundy, 2011).

# Chapter 3

## Transiting exoplanet technique and application

### 3.1 Transiting exoplanets

The first exoplanet transit event was first announced in 2000 with the transit observation of the planet HD 209458b (Charbonneau et al., 2000; Henry et al., 2000). After the first detection, a large proportion of exoplanet detections have been discovered using the transit method through ground-based transit searches, such as OGLE, WASP and HAT. Nevertheless, major transit discoveries are expected from space, such as the *Kepler* mission, which has discovered more than 70 confirmed exoplanets and 2,300 planetary candidates to date.

The transit method consists of detecting the dip in a stellar light curve when a planet crosses the line of sight towards its host star. Therefore, the perfect alignment between the observer, the planet and the star is required. In the case of a transiting system, edge-on planetary systems are observed. Therefore, transiting observational data provides a great number of physical exoplanet parameters: mass, radius, density and surface gravity.

To investigate the detectability of a transiting exoplanet, the probability of detecting transit events,  $P_{tran}$ , is defined. This probability relates to the star's radius and the distance between star and planet (Borucki & Summers, 1984). For elliptical

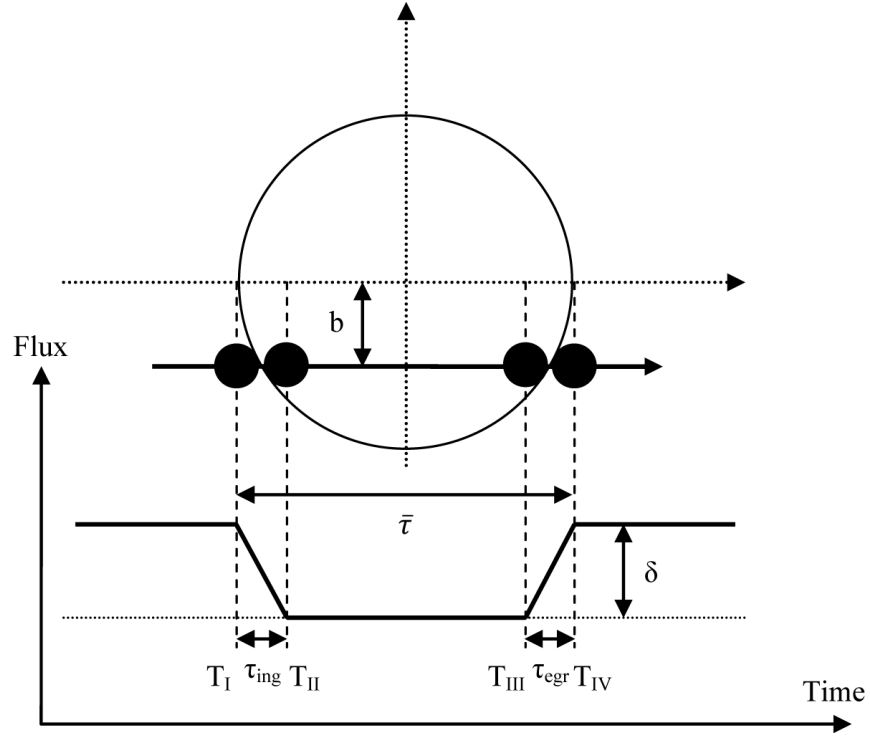


Figure 3.1: Transiting light curve with four contact points and three main parameters: transit depth, transit duration, and ingress and egress durations.

orbit, the geometric probability can be written as,

$$P_{tran} = \frac{R_*}{a_p(1 - e_p \cos f_{tp})}, \quad (3.1)$$

where  $R_*$  is star radius and  $f_{tp}$  is planet true anomaly. Therefore, the close-in planet could have high probability of detection.

The dip in stellar light curve produced by planetary occultation is described by three main parameters: transit depth, transit duration, and ingress and egress durations. These three parameters depend on the size of star and planet, planetary inclination and separation (Figure 3.1).

### Transit depth

The depth of the transit is given by the ratio of projection area of the planet radius,  $R_p$ , and the star,  $R_*$ ,

$$\delta = \left(\frac{R_p}{R_*}\right)^2. \quad (3.2)$$

### Transit duration

The transit duration is the duration between the first contact and last contact. For circular orbit, the duration is defined by,

$$\bar{\tau} = T_{\text{IV}} - T_{\text{I}} = \frac{P_p}{\pi} \arcsin\left(\sqrt{\frac{1 - b^2}{(a_p/R_*)^2 - b^2}}\right), \quad (3.3)$$

where  $P_p$  is planet period and  $b$  is impact parameter (Seager & Mallén-Ornelas, 2003). For eccentric orbit, the transit duration is more challenging. A number of models have been proposed, such as Tingley & Sackett (2005) and Winn (2010).

### Ingress and egress durations

The shape of the dip is defined by ingress ( $\tau_{ing}$ ) and egress durations ( $\tau_{egr}$ ) which are the duration between first and second contact time and third and fourth contact time, respectively. The ingress and egress are equal in circular orbit,

$$\tau_{ing} = \tau_{egr} = T_{\text{II}} - T_{\text{I}} = T_{\text{IV}} - T_{\text{III}} = \bar{\tau} \frac{R_p}{R_*} \sqrt{1 - b^2}. \quad (3.4)$$

However,  $\tau_{ing}$  and  $\tau_{egr}$  are unequal for an eccentric orbit because of the variation in projected speed (Winn, 2010).

## 3.2 Timing variation detection techniques

### Transit Timing Variations (TTV)

The Transit Timing Variations (TTV) is an exoplanet detection technique which measures the variations in the timing of transit of planet which was proposed by Sartoretti & Schneider (1999). The transits of a planet in a Keplerian orbit around its host are exactly periodic. However, in a multi-planet system, the presence of a third body in the system causes the change in planetary orbit. The time between transits varies because the transiting planet and other planets exchange energy and angular momentum. This gravitational interaction perturbs the orbit of the transiting planet and causes a short-period oscillation of the semi-major axes and eccentricities. For a given transiting planet, the TTV signal depends on seven unknown parameters

of the perturbing planet; mass, semi-major axis, eccentricity, inclination, nodal and periapse longitudes and orbital phases of both planets for a given epoch (Holman & Murray, 2005).

TTV provides the capability to discover additional planets around stars with a transiting planet, even if it does not transit the star. Moreover, TTV is a very powerful method for searching for low-mass planets down to Earth-size planets because very small changes in planet's orbital elements can be measured by timing transits. The first detection using TTV was Kepler-19c which was found from the time variation of the transiting planet, Kepler-19b (Ballard et al., 2011).

### **Transit Duration Variation (TDV)**

Similar to the TTV method, Transit Duration Variation (TDV) measures the variation of transit duration due to the mutual gravitational interaction between two or more objects. The TDV signal is predicted to be 90 degrees out-of-phase with TTV which helps us to prove the reliability of the TTV signal (Figure 3.2) (Kipping, 2009a).

## **3.3 TTV and TDV exomoon detection techniques**

In section 2.4, most possible methods for detecting exomoons are described, such as transit (Simon et al., 2007), direct imaging (Baines et al., 2007) and microlensing (Han & Han, 2002). However, the TTV and TDV techniques are focused in this dissertation since they could detect small exomoons.

### **3.3.1 Transit Timing Variation (TTV)**

TTV was presented by Sartoretti & Schneider (1999). They assumed that both the planet and moon have circular orbits and the planet-moon orbital plane is co-aligned with the planet-star orbital plane. The displacement of the planet from the planet-moon barycentre is given by,

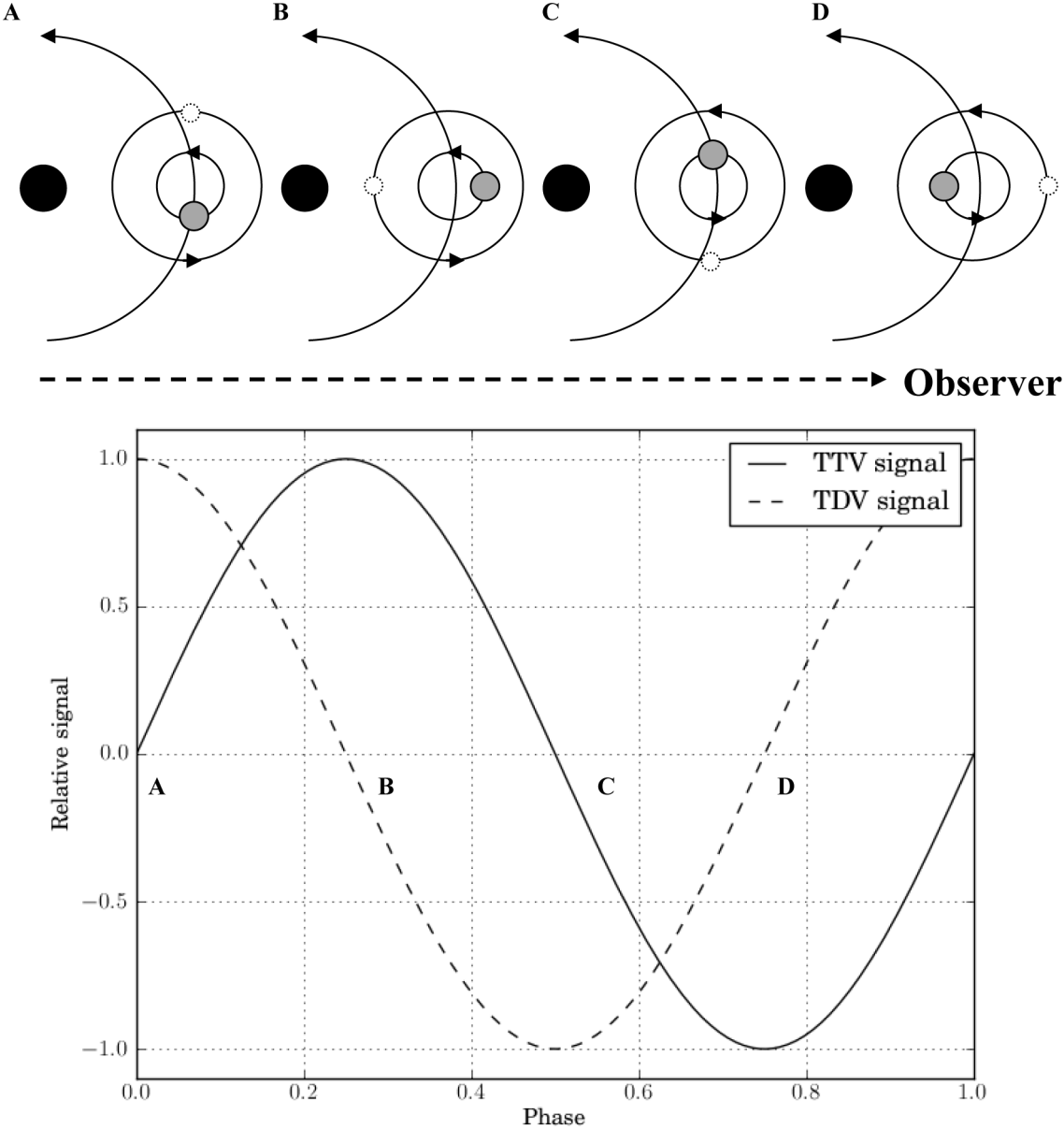


Figure 3.2: Variation of TTV and TDV signals due to planet (gray spheres) and moon (black spheres) positions.

$$a_{pb} = \left(\frac{M_m}{M_p}\right)a_m , \quad (3.5)$$

where  $a_{pb}$  is the semi-major axis of the planet around the planet-moon barycentre. The peak-to-peak amplitude of the TTV signal ( $\Delta t_{TTV}$ ) can be written as,

$$\Delta t_{TTV} \sim 2a_m M_m M_p^{-1} \times P_p (2\pi a_p)^{-1} . \quad (3.6)$$

In the case of eccentric orbits, the waveforms are not sinusoidal. The root-mean-square (RMS) amplitude is used due to validation for all waveforms. The RMS amplitude of the TTV signal is given by,

$$\delta_{TTV} = \frac{1}{\sqrt{2}} \frac{a_p^{1/2} a_m M_m (M_p + M_m)^{-1} \zeta_T(e_m, \varpi_m)}{\sqrt{G(M_* + M_p + M_m)} \Upsilon(e_p, \varpi_p)} \quad (3.7)$$

$$\delta_{TTV} \propto M_m a_m , \quad (3.8)$$

where

$$\zeta_T = \frac{(1 - e_m^2)^{1/4}}{e_m} \sqrt{e_m^2 + \cos(2\varpi_m)(2(1 - e_m^2)^{3/2} - 2 + 3e_m^2)} , \quad (3.9)$$

$$\Upsilon = \cos\left[\arctan\left(\frac{-e_p \cos \varpi_p}{1 + e_p \sin \varpi_p}\right)\right] \cdot \sqrt{\frac{2(1 + e_p \sin \varpi_p)}{1 - e_p^2} - 1} , \quad (3.10)$$

where  $\varpi_p$  and  $\varpi_m$  are the positions of pericentre of planet and moon respectively (Kipping, 2009a). For edge-on circular orbit, the TTV RMS amplitude can be written as,

$$\delta_{TTV} = \frac{a_m M_m P_p}{a_p M_p \sqrt{2\pi}} . \quad (3.11)$$

From studies by Holman & Murray (2005) and Agol et al. (2005), the TTV technique has a sensitivity to detect low-mass planets down to sub Earth-mass. In a recent study, Earth-mass exomoons around Neptune-mass exoplanets could be detected by *Kepler* (Kipping, 2009a).

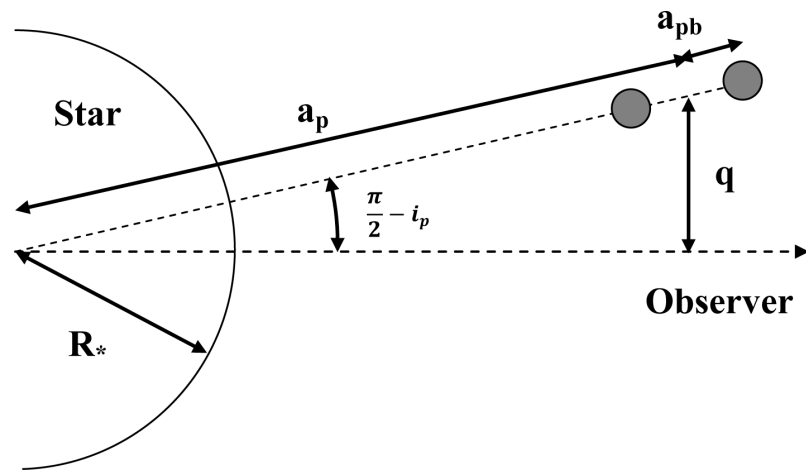


Figure 3.3: The side-on view of the star-planet-moon system shows the distance perturbation of the planet (two grey spheres) caused by the moon.

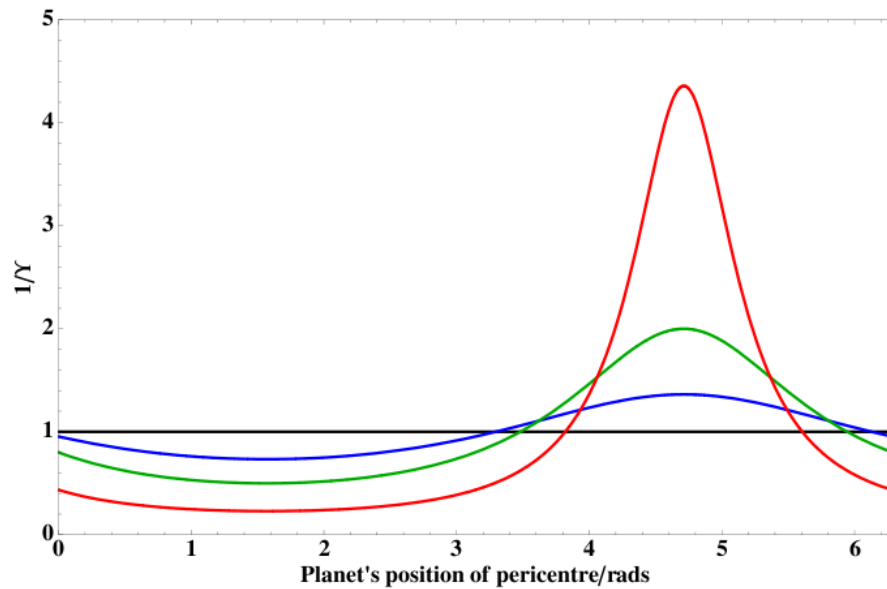


Figure 3.4: The value of  $\Upsilon^{-1}$  versus the planet's position of pericentre,  $\varpi_p$ . The black, blue, green and red lines represent planetary eccentricities ( $e_p$ ) of 0, 0.3, 0.6 and 0.9 respectively (Kipping, 2009a).

Unfortunately, TTV can also be induced by a multitude of phenomena, including general relativistic precession of the orbit, stellar peculiar motion and parallax effects.

### 3.3.2 Transit Duration Variation (TDV)

TDV is the periodic change in the transit duration over many measurements caused by the apparent velocity of the planet which increases and decreases due to the planet-moon interaction. In 2009, Kipping showed that exomoons should induce not only the TTV effect but also the TDV effect on their host planets (Kipping, 2009a).

For the planet's inclination of 90 degrees and the moon's orbit which is coplanar with planet-star orbit case, the TDV amplitude can be written as,

$$\delta_{TDV} = \sqrt{\frac{a_p}{a_m}} \cdot \sqrt{\frac{M_m^2}{(M_p + M_m)(M_* + M_p + M_m)}} \cdot \frac{\bar{\tau}}{\sqrt{2}} \frac{\zeta_D(e_m, \varpi_m)}{\Upsilon(e_p, \varpi_p)} \quad (3.12)$$

$$\delta_{TDV} \propto M_m a_m^{-1/2}, \quad (3.13)$$

where

$$\zeta_D = \sqrt{\frac{1 + e_m^2 - e_m^2 \cos(2\varpi_m)}{1 - e_m^2}}, \quad (3.14)$$

where  $\tau$  is the duration of a transit ( $\tau \propto 1/v_{p\perp}$ ). For the systems with non-coplanar orbits, the TDV effect can be separated into two main constituents, a velocity (V) component and a transit impact parameter (TIP) component (Kipping, 2009b). The V-component is caused by the variation in velocity of the planet due to the moon's gravity. The TIP-component is affected by the planet moving between high and low impact parameters. The function of the impact parameter of the transit,  $b$ , is defined by,

$$b = \frac{r_p \cos(i_p)}{R_*} = \frac{q}{R_*} . \quad (3.15)$$

Where  $e_m = 0$  and Euler angles of the moon orbit with respect to the star-planet plane ( $\alpha$ ,  $\beta$  and  $\gamma$ ) are equal to zero, the RMS amplitude of the TDV signal is given by,

$$\delta_{TDV} = \left[ \underbrace{\frac{a_{pb} a_p \cos^2 i}{(R_* + R_p)^2 - a_p^2 \cos^2 i}}_{\text{TIP-Component}} \pm \underbrace{\frac{2\pi a_{pb}}{P_m} \frac{1}{v_{B\perp}}}_{\text{V-Component}} \right] \cdot \frac{\bar{\tau}}{\sqrt{2}} , \quad (3.16)$$

where  $P_m$  is moon period and  $v_{B\perp}$  is the projected velocity of the planet-moon barycentre across the face of the star during transit. The positive sign refers to prograde moon orbits and the negative sign refers to retrograde orbits. In the system with 90 degrees orbital inclination and circular orbit, the TDV-TIP component will be zero and the RMS amplitude of the TDV signal is

$$\delta_{TDV} = \bar{\tau} \frac{a_m M_m P_p}{a_p M_p P_m \sqrt{2\pi}} , \quad (3.17)$$

where

$$\bar{\tau} = \frac{P_p}{\pi} \arcsin \left[ \left( \frac{R_*}{a_p} \right)^2 \right] . \quad (3.18)$$

The TDV technique cannot detect habitable exomoons alone because the TDV signals are relatively weak compared with the TTV signals (Porter & Grundy, 2011). However, combined with the TTV signals, the orbital separation and mass of exomoons can be obtained by using equation (3.8) and (3.13) and the signals have  $\frac{\pi}{2}$  phase difference which provide a unique exomoon signature (Figure 3.5).

The TDV signal can also be induced by parallax effects. This effect should be taken into account for high-precision, long timeline transit observations (Scharf, 2007).

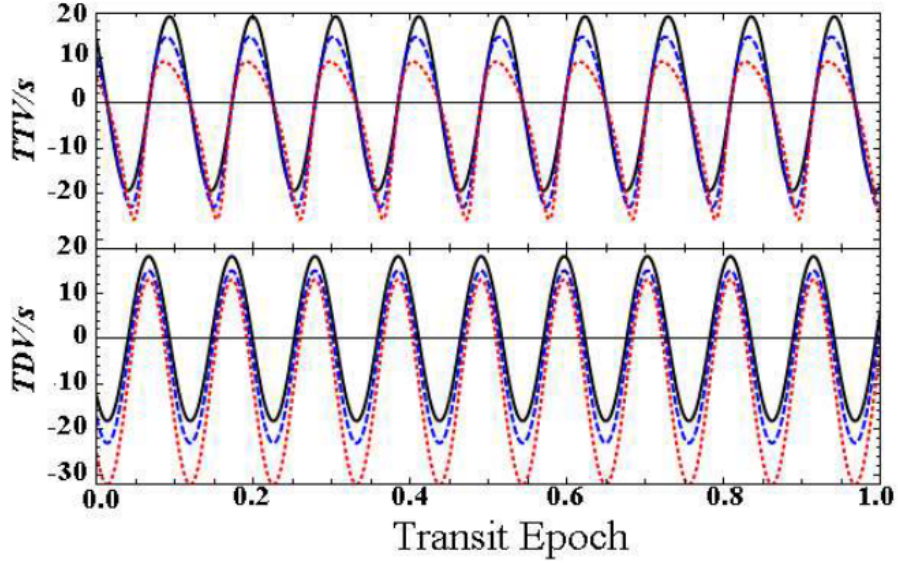


Figure 3.5: The TTV and TDV signal simulated from 1 Earth-mass exomoon orbiting GJ436b. TTV leads TDV by a  $\pi/2$  phase difference. The solid line represents  $e_p = 0$ , the dashed line  $e_p = 0.3$  and the dotted line  $e_p = 0.6$  (Kipping, 2009a).

## 3.4 Exoplanet transit surveys

At present, a great number of exoplanet detection surveys have been started or will be started in the near future. From the previous section, exomoons could be detected by using the TTV and TDV techniques in addition to the transit technique. Therefore, in this section, transit missions are focused upon. Both current ground-based and space-based surveys are described. Furthermore, potential future space-based missions are discussed.

### 3.4.1 Ground-based surveys

#### WASP

The WASP (Wide Angle Search for Planets) is the United Kingdom's leading exoplanet detection program via the transit technique. The WASP observatories consist of two eight lens robotic telescopes located at both hemispheres. Each telescope has a field of view  $7.8 \times 7.8$  degrees. In the north hemisphere, the telescope (SuperWASP-North) is located at the Observatorio del Roque de los Muchacho, La Palma. SuperWASP-South is located at the South African Astronomical Observatory (SAAO), South Africa. Each night, the two SuperWASP telescopes survey 6-8

fields at similar declination covering one hour in right ascension (Pollacco et al., 2006). In 2010, the first WASP public data was released. This data contains light curves, raw and calibrated images of the first three observing seasons (2004-2008) containing more than 30 detected exoplanets (Butters et al., 2010).

### **HATNet**

The HATNet (Hungarian-made Automated Telescope Network) was developed in 1991 by Hungarian astronomers. The network of 6 small fully automated telescopes (4 at Fred Lawrence Whipple Observatory, Arizona, and 2 at Mauna Kea, Hawaii) was established in 2003 (Bakos et al., 2004, 2011). Since 2009, the HAT-South project, with 2 identical telescopes sited at Las Campanas, Chile and Siding Springs, Australia, along with the HESS site in Namibia, have been operational (Bakos et al., 2009). HATNet discovered its first transiting exoplanet in 2006, HAT-P-1b (Bakos et al., 2007). To date, HATNet has discovered about 100 confirmed transiting exoplanets (Bakos et al., 2011).

### **3.4.2 Space missions**

#### **CoRoT**

The CoRoT (Convection, Rotation and planetary Transits) is a space-based project focused on asteroseismology of variable stars. However, after the discovery of the first hot Jupiter, CoRoT now includes exoplanet detection in the programme. The 27-cm telescope with a  $2.8 \times 2.8$  degrees camera was launched in December 2006. The telescope has 4 CCDs, two are for the exoplanet program and two are for the seismology program. CoRoT can detect stars with magnitude between  $12^{th}$  and  $16^{th}$ . At present, CoRoT has detected more than 15 exoplanets (Hébrard et al., 2011), including the first transiting super-Earth, CoRoT-7b (Léger et al., 2009).



Figure 3.6: The *Kepler* photometer instrument mounted on the *Kepler* spacecraft. The image is courtesy of NASA.

## Kepler

*Kepler* is a NASA space mission designed to determine the frequency of extra-solar planets, their characteristics and association with host star characteristics using the transit method. It is a 0.95-metre telescope with 42 CCDs (field of view of 105 deg<sup>2</sup>) and was launched in March 2009. It can detect star-planet systems brighter than  $V=14$ . In February 2011, the *Kepler* mission released data for 156,453 stars, including 1,235 planetary candidates in 997 systems. 68 candidates are Earth-size planets ( $R_p < 1.25R_{\oplus}$ ) and 288 planets are super-Earth size ( $1.25R_{\oplus} \leq R_p < 2R_{\oplus}$ ) (Borucki et al., 2011a). In early 2012, more than 1,000 additional candidates were announced (Batalha et al., 2012). These results provide a better understanding of exoplanets. At present, more than 25 *Kepler* exoplanets, including Kepler-22b, have been confirmed (Borucki et al., 2012).

## Euclid

*Euclid* is an ESA observatory probe to understand dark matter and dark energy which will be launched in 2019. However, *Euclid* has sensitivity for detecting exoplanets using transit and microlensing techniques. *Euclid* will have two instruments, a visual instrument (VIS) and a near infrared instrument (NISP). The VIS will be

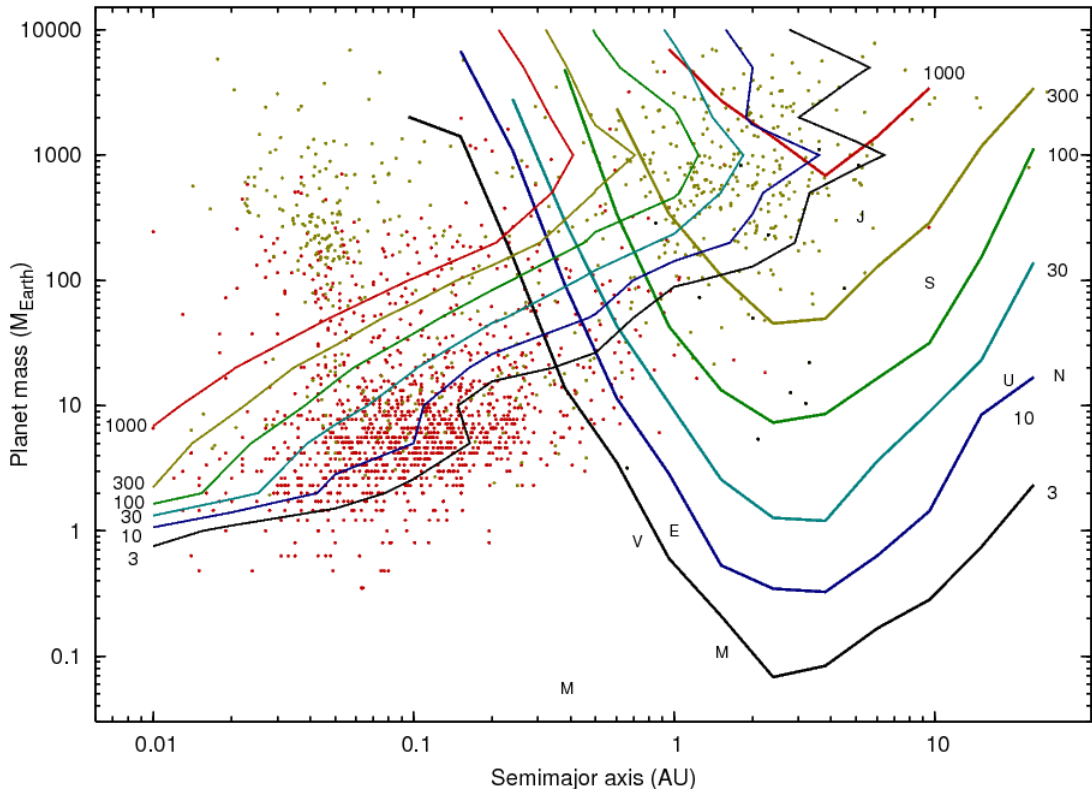


Figure 3.7: Planet detection capability of *Euclid*. The contours indicate the number of detections using transit (left) and microlensing (right) techniques, assuming one planet per star at each point in the planet mass-semi-major axis plane. The yellow dots are published planet detections and the red dots are the published *Kepler* candidates (McDonald & et al, 2012; Penny et al., 2012).

equipped with 36 CCDs in broad band (R+I+Z) which will be used for measuring the shape of galaxies. The NISP is equipped with 16 HgCdTe NIR detectors with Y, J, H bands and a field of view of  $0.55 \text{ deg}^2$ , and a resolution better than 0.3 arcseconds. There are two primary cosmology surveys in this mission, a wide survey which covers  $15,000 \text{ deg}^2$  of extragalactic sky and a deep survey which covers  $40 \text{ deg}^2$  at ecliptic poles. The additional science surveys, including a microlensing exoplanet survey, can be added. In this survey, *Euclid* could detect not only microlensing exoplanets, but also transiting exoplanets (Laureijs et al., 2011).

## WFIRST

The WFIRST (Wide-Field Infrared Survey Telescope) is a NASA mission designed to detect exoplanets using the gravitational microlensing technique and dark

energy with weak lensing. WFIRST will be a 1.5-metre class wide field space telescope. It will have a potential to detect exoplanets with masses greater than  $0.1 M_{\oplus}$  at distances more than 0.5 AU using the microlensing technique, which will develop upon exoplanet statistics from the *Kepler* mission. In this mission, transiting exoplanets could also be detected (Green et al., 2011).

## PLATO

The PLATO (PLANetary Transit and Oscillations of stars), an ESA Medium class mission, has been proposed for M2 and M3 launch slots for the Cosmic Visions 2015-2025 programme. It has a primary goal to discover and characterize exoplanets with high precision using 34 wide-field telescopes. It can be detected planets down to Earth-size orbiting F to M main sequence stars in their habitable zone. Moreover, it can determine the radius and mass of the host stars and the planets with accuracy of 1% and the age of the systems with accuracy better than 10% (Catala et al., 2011).

## EChO

The Exoplanet CHaracterisation Observatory (EChO) is an ESA M-class candidate mission for the Cosmic Vision 2015-2025 programme. The mission has a main aim to investigate exoplanetary atmospheres. The 1-metre telescope will observe the exoplanets at different points in their orbit to determine the spectrum of the planetary atmosphere. The main target list for the mission includes Jupiter-size to super-Earth sized planet orbiting F to M type stars (Tinetti et al., 2011).

## 3.5 The detectability of exomoons with *Kepler* class photometry

The *Kepler* mission is a space mission designed to detect habitable exoplanets (Section 3.4.2). In order to calculate the detectability of exomoons, TTV and

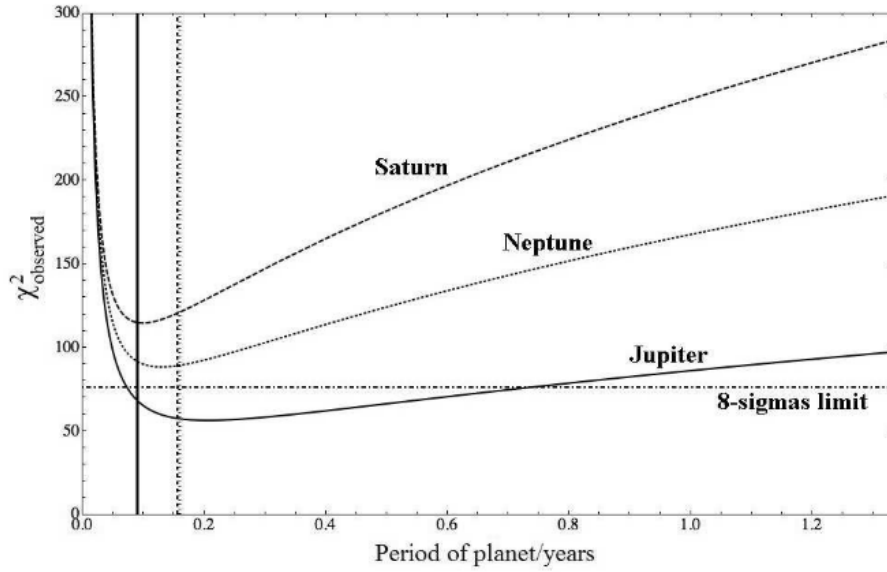


Figure 3.8: The TTV detectability of a  $0.2 M_{\oplus}$  exomoon in G2V system around a Jupiter, Saturn and Neptune-like planet. The vertical lines show the stability limit of Barnes & O’Brien (Barnes & O’Brien, 2002) and horizontal line shows the  $8\text{-}\sigma$  confidence level. (Kipping et al., 2009).

TDV signal amplitudes, times of transit minimum and transit duration errors and confidence of detection were studied by Kipping et al. (2009).

In order to define detectable exomoons, Kipping used an  $8\text{-}\sigma$  confidence level. From his simulation result, Jupiter’s exomoons are the hardest to detect and Saturn’s exomoons are the easiest because of its low density (Figure 3.8). For exomoons around a Saturn-like planet, the minimum habitable exomoon mass which could be detected with *Kepler* around an M5V star would be  $0.09 M_{\oplus}$  (the stable mass limit from Barnes & O’Brien (2002) is  $0.008 M_{\oplus}$ ) and  $0.18 M_{\oplus}$  for M2V star systems (the stable mass limit is  $0.41 M_{\oplus}$ ). Due to the limitation of *Kepler* target stars, the minimum detectable habitable exomoon mass with *Kepler* is  $0.2 M_{\oplus}$  (Figure 3.9).

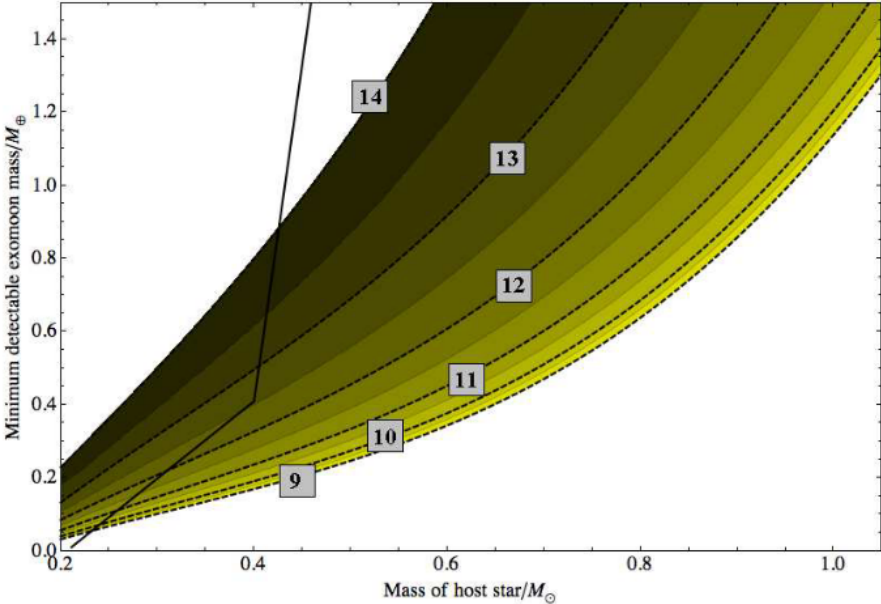


Figure 3.9: The lowest detectable exomoon mass orbiting a Saturn-like planet. The solid line shows the mass stability limit from Barnes & O’Brien (Barnes & O’Brien, 2002) and the dot line shows the magnitude limit to 25% of the exomoons in the sample (Kipping et al., 2009).

# Chapter 4

## Generating and analysing light curves of an exoplanet with exomoon

### 4.1 Planet-moon orbit

In this section, the coordinate system and fundamental parameters which form the basis of exomoon light curve calculations are defined. Transiting exoplanets are detected from the variation in the light curve of the host stars. Information from transit light curves helps astronomers to obtain direct estimates of the exoplanet mass and radius which reveal the physical nature of the exoplanet, such as its average density and surface gravity. A very high precision light curve can be used to detect multi-planetary systems or star spots (Charbonneau et al., 2007). Moreover, perturbations in the timing of exoplanet transits may be used to detect the planet's satellites or additional planets (Sartoretti & Schneider, 1999).

The first step to generating a transiting exomoon light curve is to define the planet and moon positions with respect to the host star. However, the star, planet and moon are a three-body problem which has no exact analytical solution. Therefore, in this work, the planet's orbit and moon's orbit are created using a Keplerian orbit of star-planet and planet-moon, separately, and then perturbing the planet's

position with planet-moon interaction.

Firstly, a planetary orbit with a centre at the origin of an  $(x_1, y_1, z_1)$  co-ordinate system is considered. The position of the planet can be written as,

$$\begin{aligned} x_1 &= a_p e_p + r_p \cos f_{tp} , \\ y_1 &= r_p \sin f_{tp} , \\ z_1 &= 0 , \end{aligned} \tag{4.1}$$

where  $a_p$  is planet's semi-major axis,  $e_p$  is planet's eccentricity,  $r_p$  is the distance of planet from the origin,

$$r_p = \frac{a_p(1 - e_p^2)}{1 + e_p} \cos(f_{tp}) , \tag{4.2}$$

and true anomaly,  $f_{tp}$ , is defined by,

$$\tan\left(\frac{f_{tp}}{2}\right) = \sqrt{\frac{1 + e_p}{1 - e_p}} \cdot \tan\left(\frac{f_{mp}}{2}\right) . \tag{4.3}$$

$f_{mp}$  is the mean anomaly which may be written as a function of the time elapsed since the planet's periapsis,  $t - t_p$ ,

$$f_{mp} - e_p \cos f_{mp} = \frac{2\pi}{P_p} (t - t_p) . \tag{4.4}$$

In the second step, the coordinates  $(x_1, y_1, z_1)$  are transformed to star planet barycentre coordinates  $(x_2, y_2, z_2)$  lying at  $(a_p e_p, 0, 0)$  in the  $(x_1, y_1, z_1)$  co-ordinate system:

$$\begin{aligned} x_2 &= r_p \cos(f_{tp}) , \\ y_2 &= r_p \sin(f_{tp}) , \\ z_2 &= 0 . \end{aligned} \tag{4.5}$$

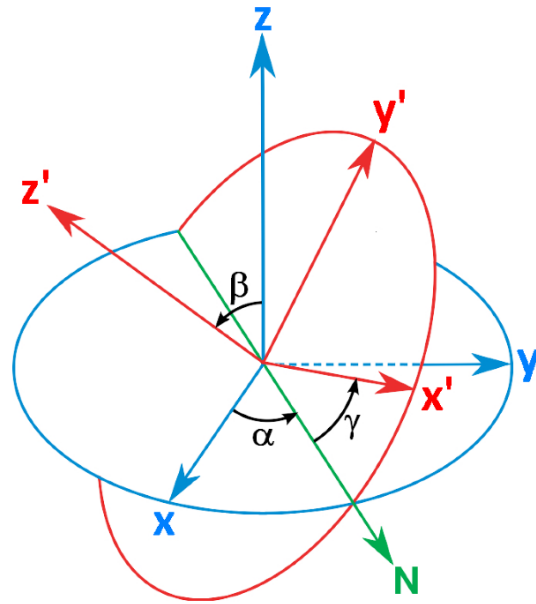


Figure 4.1: Euler angles where  $x - y - z$  system (Blue) is fixed,  $X - Y - Z$  system (Red) is rotated and  $N$  (Green) is the reference direction (Kipping, 2009b).

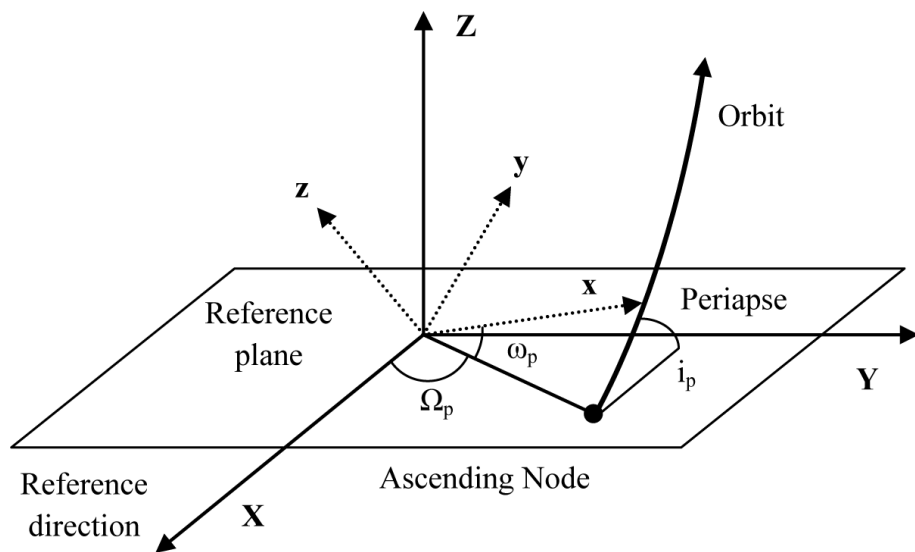


Figure 4.2: Orbital elements of a transiting planet-star system.

From Figure 4.1 and 4.2, the orbital arrangement of the planet is rotated by the Euler angles,  $\alpha$  (Longitude of ascending node,  $\Omega_p$ ),  $\beta$  (Inclination,  $i_p$ ) and  $\gamma$  (Argument of periapsis,  $\omega_p$ ), with respect to the plane of reference (the reference direction lies at  $x = +\infty$ ) which can be written as,

$$\begin{aligned} x_3 &= r_p [\cos(\Omega_p) \cos(\omega_p + f_{tp}) + \sin(i_p) \sin(\Omega_p) \sin(\omega_p + f_{tp})] , \\ y_3 &= r_p [\sin(\Omega_p) \cos(\omega_p + f_{tp}) + \sin(i_p) \cos(\Omega_p) \sin(\omega_p + f_{tp})] , \\ z_3 &= r_p [\cos(i_p) \sin(\omega_p + f_{tp})] . \end{aligned} \quad (4.6)$$

If the planet has a moon, the moon's orbit can be defined in a similar manner to the planet's orbit. From here onwards, unless otherwise stated, quantities with subscript  $p$  denote planet parameters and those with subscript  $m$  denote moon parameters. The presence of the moon perturbs the planetary orbit. The planet's reflex motion from the moon's perturbation can be written as,

$$\mathbf{r}_{\mathbf{bp}} M_p = \mathbf{r}_{\mathbf{bm}} M_m , \quad (4.7)$$

where  $\mathbf{r}_{\mathbf{bp}}$  and  $\mathbf{r}_{\mathbf{bm}}$  are distance between planet-moon barycentre and planet and moon, respectively (where hereafter bold typeface denotes a vector). Finally, the position of the planet and moon with respect to star-planet reference plane,  $\mathbf{r}_{\mathbf{sp}}$  and  $\mathbf{r}_{\mathbf{sm}}$ , are

$$\mathbf{r}_{\mathbf{sp}} = \mathbf{r}_{\mathbf{p}} + \mathbf{r}_{\mathbf{bp}} , \quad (4.8)$$

$$\mathbf{r}_{\mathbf{sm}} = \mathbf{r}_{\mathbf{p}} + \mathbf{r}_{\mathbf{bm}} . \quad (4.9)$$

For an observer at  $z = +\infty$ ,  $\Omega_p$  has no effect on the transit since the light curve is defined by the separation only. The planet position can be defined as,

$$\begin{aligned}
x_p &= r_p \cos(\omega_p + f_{tp}) \\
&\quad - r_{bp} \cos(\omega_m + f_{tm}) \cos(\omega_p + \Omega_m) \\
&\quad + r_{bp} \sin(i_m) \sin(\omega_m + f_{tm}) \sin(\omega_p + \Omega_m) ,
\end{aligned} \tag{4.10}$$

$$\begin{aligned}
y_p &= r_p \cos(i_p) \sin(\omega_p + f_{tp}) \\
&\quad + r_{bp} \sin(i_p) \cos(i_m) \sin(\omega_m + f_{tm}) \\
&\quad - r_{bp} \cos(i_p) \sin(i_m) \sin(\omega_m + f_{tm}) \cos(\omega_p \\
&\quad + \Omega_m) - r_{bp} \cos(i_p) \cos(\omega_m + f_{tm}) \sin(\omega_p + \Omega_m) ,
\end{aligned} \tag{4.11}$$

$$\begin{aligned}
z_p &= r_p \sin(i_p) \sin(\omega_p + f_{tp}) \\
&\quad - r_{bp} \cos(i_p) \cos(i_m) \sin(\omega_m + f_{tm}) \\
&\quad - r_{bp} \sin(i_p) \sin(i_m) \sin(\omega_m + f_{tm}) \cos(\omega_p + \Omega_m) \\
&\quad - r_{bp} \sin(i_p) \cos(\omega_m + f_{tm}) \sin(\omega_p + \Omega_m) ,
\end{aligned} \tag{4.12}$$

and moon position can be written as,

$$\begin{aligned}
x_m &= r_p \cos(\omega_p + f_{tp}) \\
&\quad + r_{bm} \cos(\omega_m + f_{tm}) \cos(\omega_p + \Omega_m) \\
&\quad - r_{bm} \sin(i_m) \sin(\omega_m + f_{tm}) \sin(\omega_p + \Omega_m) ,
\end{aligned} \tag{4.13}$$

$$\begin{aligned}
y_m &= r_p \cos(i_p) \sin(\omega_p + f_{tp}) \\
&\quad - r_{bm} \sin(i_p) \cos(i_m) \sin(\omega_m + f_{tm}) \\
&\quad + r_{bm} \cos(i_p) \sin(i_m) \sin(\omega_m + f_{tm}) \cos(\omega_p + \Omega_m) \\
&\quad + r_{bm} \cos(i_p) \cos(\omega_m + f_{tm}) \sin(\omega_p + \Omega_m) ,
\end{aligned} \tag{4.14}$$

$$\begin{aligned}
z_m &= r_p \sin(i_p) \sin(\omega_p + f_{tp}) \\
&\quad + r_{bm} \cos(i_p) \cos(i_m) \sin(\omega_m + f_{tm}) \\
&\quad + r_{bm} \sin(i_p) \sin(i_m) \sin(\omega_m + f_{tm}) \cos(\omega_p + \Omega_m) \\
&\quad + r_{bm} \sin(i_p) \cos(\omega_m + f_{tm}) \sin(\omega_p + \Omega_m) .
\end{aligned} \tag{4.15}$$

The star-moon sky-projected distance ( $S_{sm}$ ), the star-planet sky-projected distance ( $S_{sp}$ ) and the separation between the planet and the moon ( $S_{pm}$ ) can be written as,

$$S_{sm}^2 = \frac{x_m^2 + y_m^2}{R_*^2} , \tag{4.16}$$

$$S_{sp}^2 = \frac{x_p^2 + y_p^2}{R_*^2} , \tag{4.17}$$

$$S_{pm}^2 = \frac{(x_p - x_m)^2 + (y_p - y_m)^2}{R_*^2} , \tag{4.18}$$

where  $R_*$  is star radius.

## 4.2 Planetary transit light curve

In order to generate light curves of transiting systems, the limb darkening effect of the host star which causes the star's surface brightness peak at the centre is

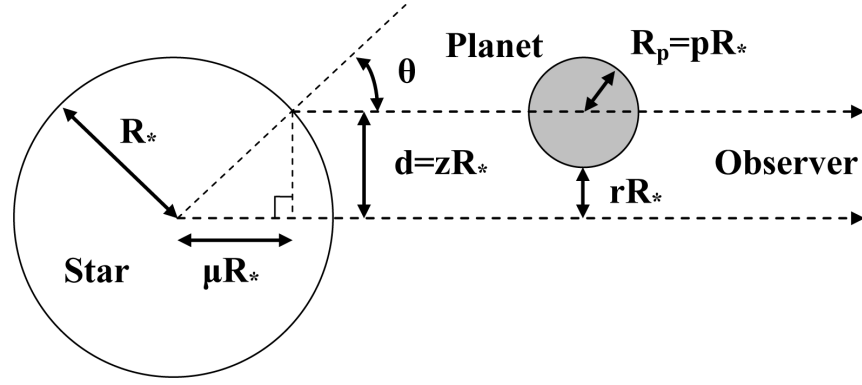


Figure 4.3: Geometry of limb darkening.

considered. The nonlinear limb-darkening in a transit light curve which is first presented by Mandel & Agol (2002). The function of the star's intensity,  $I$ , with nonlinear limb-darkening is defined by,

$$I(r) = 1 + \sum_{n=1}^4 c_n (1 - \mu^{n/2}), \quad (4.19)$$

where  $c_n$  are coefficients and  $\mu$  is the normalised radial coordinate of the star,

$$\mu = \cos \theta = (1 - r^2)^{1/2}, 0 \leq r \leq 1, \quad (4.20)$$

where  $\theta$  is the angle between a line normal to the stellar surface and the line of sight of the observer and  $r$  is radial distance from the centre of the star. In this dissertation, the quadratic limb darkening,  $I(r) = 1 - \gamma_1(1 - \mu) - \gamma_2(1 - \mu)^2$ , where  $\gamma_1 + \gamma_2 < 1$ , is used. From equation 4.19, the constant  $c_n$  in the quadratic limb darkening model can be written as,

$$\begin{aligned} c_1 &= 0 \\ c_2 &= \gamma_1 + 2\gamma_2 \\ c_3 &= 0 \\ c_4 &= -\gamma_2, \end{aligned} \quad (4.21)$$

and

$$c_0 \equiv 1 - c_1 - c_2 - c_3 - c_4 . \quad (4.22)$$

In what follows,  $R_*$  is the star radius,  $R_p$  is the planet radius,  $d$  is the center-to-center distance between the star and the planet,  $z = d/R_*$  is the normalized separation, and  $p = R_p/R_*$  is the size ratio. The light curve with quadratic limb darkening of the system can be written as,

$$F = 1 - \frac{1}{4\Omega} \left\{ (1 - c_2)\lambda^e + c_2 \left[ \lambda^d + \frac{2}{3}\Theta(p - z) \right] - c_4 \eta^d \right\} . \quad (4.23)$$

where  $\Omega = \sum_{n=0}^4 c_n (n + 4)^{-1}$  and  $\Theta(p - z)$  is heaviside step function,

$$\Theta(p - z) = \begin{cases} 0, & p - z < 0 , \\ \frac{1}{2}, & p - z = 0 , \\ 1, & p - z > 0 , \end{cases} \quad (4.24)$$

and  $\lambda^e$  is defined by

$$\lambda^e(p, z) = \begin{cases} 0, & 1 + p < z , \\ \frac{1}{\pi}(p^2 \kappa_0 + \kappa_1 - \kappa_2), & |1 - p| < z \leq 1 + p , \\ p^2, & z \leq 1 - p , \\ 1, & z \leq p - 1 , \end{cases} \quad (4.25)$$

$$\kappa_0 = \cos^{-1} \frac{-1 + p^2 + z^2}{2pz} , \quad (4.26)$$

$$\kappa_1 = \cos^{-1} \frac{1 - p^2 + z^2}{2z} , \quad (4.27)$$

$$\kappa_2 = \sqrt{\frac{4z^2 - (1 + z^2 - p^2)^2}{4}} . \quad (4.28)$$

Finally, the value of  $\lambda^d$  and  $\eta^d$  are defined in Table 4.1 and Equation 4.29 (Mandel & Agol, 2002).

Table 4.1: Limb-darkening occultation (Mandel &amp; Agol, 2002).

| Case | $\mathbf{p}$            | $\mathbf{z}$                               | $\lambda^{\mathbf{d}}(\mathbf{z})$ | $\eta^{\mathbf{d}}(\mathbf{z})$ |
|------|-------------------------|--|------------------------------------|---------------------------------|
| 1    | $(0, \infty)$           | $[1 + p, \infty)$                          | 0                                  | 0                               |
|      | 0                       | $[0, \infty)$                              | 0                                  | 0                               |
| 2    | $(0, \infty)$           | $(\frac{1}{2} +  p - \frac{1}{2} , 1 + p)$ | $\lambda_1$                        | $\eta_1$                        |
| 3    | $(0, \frac{1}{2})$      | $(p, 1 - p)$                               | $\lambda_2$                        | $\eta_2$                        |
| 4    | $(0, \frac{1}{2})$      | $1 - p$                                    | $\lambda_5$                        | $\eta_2$                        |
| 5    | $(0, \frac{1}{2})$      | $p$  | $\lambda_4$                        | $\eta_2$                        |
| 6    | $\frac{1}{2}$           | $\frac{1}{2}$                              | $\frac{1}{3} - \frac{4}{9}\pi$     | $\frac{3}{32}$                  |
| 7    | $(\frac{1}{2}, \infty)$ | $p$  | $\lambda_3$                        | $\eta_1$                        |
| 8    | $(\frac{1}{2}, \infty)$ | $[ 1 - p , p)$                             | $\lambda_1$                        | $\eta_1$                        |
| 9    | $(0, 1)$                | $(0, \frac{1}{2} -  p - \frac{1}{2} )$     | $\lambda_2$                        | $\eta_2$                        |
| 10   | $(0, 1)$                | 0  | $\lambda_6$                        | $\eta_2$                        |
| 11   | $(1, \infty)$           | $[0, p - 1)$                               | 1                                  | 1                               |

$$\begin{aligned}
\lambda_1 &= \frac{1}{9\pi\sqrt{pz}} \left( [(1-b)(2b+a-3) - 3q(b-2)] K(k) \right. \\
&\quad \left. + \frac{4pz}{9\pi\sqrt{pz}} (z^2 + 7p^2 - 4)E(k) - \frac{3}{9\pi\sqrt{pz}} \frac{q}{a} \Pi\left(\frac{a-1}{a}, k\right) \right), \\
\lambda_2 &= \frac{2}{9\pi\sqrt{1-a}} \left[ q^2 K(k^{-1}) + (1-a)(z^2 + 7p^2 - 4)E(k^{-1}) \right] \\
&\quad + \frac{2}{9\pi\sqrt{1-a}} \left[ (1 - 5z^2 + p^2) - \frac{2}{3\pi\sqrt{1-a}} \left[ \frac{q}{a} \Pi\left(\frac{a-b}{a}, k^{-1}\right) \right] \right], \\
\lambda_3 &= \frac{1}{3} + \frac{16p}{9\pi} (2p^2 - 1)E\left(\frac{1}{2k}\right) - \frac{(1-4p^2)(3-8p^2)}{9\pi p} K\left(\frac{1}{2k}\right), \\
\lambda_4 &= \frac{1}{3} + \frac{2}{9\pi} \left[ 4(2p^2 - 1)E(2k) + (1-4p^2)K(2k) \right], \\
\lambda_5 &= \frac{2}{3\pi} \cos^{-1}(1-2p) - \frac{4}{9\pi} (3+2p-8p^2), \\
\lambda_6 &= -\frac{2}{3} (1-p^2)^{\frac{3}{2}}, \\
\eta_1 &= \frac{1}{2\pi} \left[ \kappa_1 + 2\eta_2 \kappa_0 - \frac{1}{4} (1+5p^2+z^2) \sqrt{(1-a)(b-1)} \right], \\
\eta_2 &= \frac{p^2}{2} (p^2 + 2z^2), \tag{4.29}
\end{aligned}$$

where  $E(k)$ ,  $K(k)$  and  $\Pi(n, k)$  is the complete elliptic integral of the first kind, second kind and third kind, respectively.

$$E(k) = \int_0^{\frac{\pi}{2}} \frac{1}{\sqrt{1 - k^2 \sin^2(x)}} dx \quad (4.30)$$

$$K(k) = \int_0^{\frac{\pi}{2}} \sqrt{1 - k^2 \sin^2(x)} dx \quad (4.31)$$

$$\Pi(n, k) = \int_0^{\frac{\pi}{2}} \frac{1}{(1 - n \sin^2(x)) \sqrt{1 - k^2 \sin^2(x)}} dx \quad (4.32)$$

### 4.3 Planet-moon transit light curve

The algorithms of Kipping (2011) are used to create planet-moon light curve. For the moon which transit the star with the area,  $A_{m,t}$ , its actively transit component is assumed to equal to the actively transit component of the planet with equal area. Therefore, the flux due to the planet-moon projection,  $F_{transit}$ , can be written as,

$$F_{transit} = F_{planet} - A_{m,t} \frac{F_{area}}{F_{total}}, \quad (4.33)$$

where  $F_{planet}$  is the flux of planetary transit and  $F_{total}$  is the total stellar flux,

$$\begin{aligned} F_{total} &= \int_0^1 2rI(r)dr \\ &= 1 - \sum_{n=1}^4 \frac{nc_n}{n+4} \\ &= 1 - \frac{1}{5}c_1 - \frac{1}{3}c_2 - \frac{3}{7}c_3 - \frac{1}{2}c_4, \end{aligned} \quad (4.34)$$

where  $I(r)$  is the intensity at the center-to-center distance between the star and the planet,  $r$ . The value of area flux,  $F_{area}$ , and ratio of area,  $A_m$ , depend on the moon-star separation (Table 4.2).

#### Case I

If the moon is outside the star. The area flux and ratio of area are set to be zero.

**Case II**

If the moon is in the ingress or egress portion,  $1 - s < S_{sm} < 1 + s$ , then,

$$\begin{aligned}
 F_{area,II} &= \int_{S_{sm}-s}^1 2rI(r)dr \\
 &= (a_m - 1)(c_1 + c_2 + c_3 + c_4 - 1) \\
 &\quad + \frac{4}{5}c_1(1 - a_m)^{\frac{5}{4}} + \frac{2}{3}c_2(1 - a_m)^{\frac{3}{2}} \\
 &\quad + \frac{4}{7}c_3(1 - a_m)^{\frac{7}{4}} + \frac{1}{2}c_4(1 - a_m)^2, \tag{4.35}
 \end{aligned}$$

where  $a_m = (S_{sm} - s)^2$  and  $s = R_m/R_*$  is the moon size ratio.

**Case III**

If the moon is inside the star but does not cover the centre of the star,  $s < S_{sm} < 1 - s$ , then,

$$\begin{aligned}
 F_{area,III} &= \int_{S_{sm}-s}^{S_{sm}+s} 2rI(r)dr \\
 &= (a_m - b_m)(c_1 + c_2 + c_3 + c_4 - 1) \\
 &\quad + \frac{4}{5}c_1(1 - a_m)^{\frac{5}{4}} + \frac{2}{3}c_2(1 - a_m)^{\frac{3}{2}} \\
 &\quad + \frac{4}{7}c_3(1 - a_m)^{\frac{7}{4}} + \frac{1}{2}c_4(1 - a_m)^2 \\
 &\quad - \frac{4}{5}c_1(1 - b_m)^{\frac{5}{4}} - \frac{2}{3}c_2(1 - b_m)^{\frac{3}{2}} \\
 &\quad - \frac{4}{7}c_3(1 - b_m)^{\frac{7}{4}} - \frac{1}{2}c_4(1 - b_m)^2, \tag{4.36}
 \end{aligned}$$

where  $b_m = (S_{sm} + s)^2$ .

**Case IV**

If the moon is inside the star and cover the centre of the star,  $0 < S_{sm} < s$ , then,

$$\begin{aligned}
F_{area,IV} &= \int_0^{S_{sm}+s} 2rI(r)dr \\
&= -b_m(c_1 + c_2 + c_3 + c_4 - 1) \\
&\quad + \frac{4}{5}c_1 + \frac{2}{3}c_2 + \frac{4}{7}c_3 + \frac{1}{2}c_4 \\
&\quad - \frac{4}{5}c_1(1 - b_m)^{\frac{5}{4}} - \frac{2}{3}c_2(1 - b_m)^{\frac{3}{2}} \\
&\quad - \frac{4}{7}c_3(1 - b_m)^{\frac{7}{4}} - \frac{1}{2}c_4(1 - b_m)^2 .
\end{aligned} \tag{4.37}$$

Table 4.2: Moon active transit component (Kipping, 2011).

| Case | Condition                 | Area flux ( $F_{area}$ ) | Ratio of Area ( $A_m$ )    |
|------|---------------------------|--------------------------|----------------------------|
| I    | $1 + s < S_{sm} < \infty$ | 0                        | 0                          |
| II   | $1 - s < S_{sm} < 1 + s$  | Equation 4.35            | $A_{m,t}/(\pi(1 - a_m))$   |
| III  | $s < S_{sm} < 1 - s$      | Equation 4.36            | $A_{m,t}/(\pi(b_m - a_m))$ |
| IV   | $0 < S_{sm} < s$          | Equation 4.37            | $A_{m,t}/(\pi b_m)$        |

### The actively transiting area of moon

The actively transiting area of moon can be described by 3 parameters;  $S_{sp}$ ,  $S_{sm}$  and  $S_{pm}$ . There are 27 principal cases including some unphysical cases which listed in Table 4.3 (Kipping, 2011).

Table 4.3: The actively transiting area of planet and moon (Kipping, 2011).

| Case | $S_{sp}$             | $S_{sm}$             | $S_{pm}$             | Physical | $A_{p,t}$     | $A_{m,t}$                   |
|------|----------------------|----------------------|----------------------|----------|---------------|-----------------------------|
| 1    | $S_{sp} \geq 1+p$    | $S_{sm} \geq 1+s$    | $S_{pm} \geq p+s$    | ✓        | 0             | 0                           |
| 2    | $S_{sp} \geq 1+p$    | $S_{sm} \geq 1+s$    | $p-s < S_{pm} < p+s$ | ✓        | 0             | 0                           |
| 3    | $S_{sp} \geq 1+p$    | $S_{sm} \geq 1+s$    | $S_{pm} \leq p-s$    | ✓        | 0             | 0                           |
| 4    | $S_{sp} \geq 1+p$    | $1-s < S_{sm} < 1+s$ | $S_{pm} \geq p+s$    | ✓        | 0             | $\alpha_{sm}$               |
| 5    | $S_{sp} \geq 1+p$    | $1-s < S_{sm} < 1+s$ | $p-s < S_{pm} < p+s$ | ✓        | 0             | $\alpha_{sm}$               |
| 6    | $S_{sp} \geq 1+p$    | $1-s < S_{sm} < 1+s$ | $S_{pm} \leq p-s$    | ×        | –             | –                           |
| 7    | $S_{sp} \geq 1+p$    | $S_{sm} \leq 1-s$    | $S_{pm} \geq p+s$    | ✓        | 0             | $\pi s^2$                   |
| 8    | $S_{sp} \geq 1+p$    | $S_{sm} \leq 1-s$    | $p-s < S_{pm} < p+s$ | ×        | –             | –                           |
| 9    | $S_{sp} \geq 1+p$    | $S_{sm} \leq 1-s$    | $S_{pm} \leq p-s$    | ×        | –             | –                           |
| 10   | $1-p < S_{sp} < 1+p$ | $S_{sm} \geq 1+s$    | $S_{pm} \geq p+s$    | ✓        | $\alpha_{sp}$ | 0                           |
| 11   | $1-p < S_{sp} < 1+p$ | $S_{sm} \geq 1+s$    | $p-s < S_{pm} < p+s$ | ✓        | $\alpha_{sp}$ | 0                           |
| 12   | $1-p < S_{sp} < 1+p$ | $S_{sm} \geq 1+s$    | $S_{pm} \leq p-s$    | ✓        | $\alpha_{sp}$ | 0                           |
| 13   | $1-p < S_{sp} < 1+p$ | $1-s < S_{sm} < 1+s$ | $S_{pm} \geq p+s$    | ✓        | $\alpha_{sp}$ | $\alpha_{sm}$               |
| 14   | $1-p < S_{sp} < 1+p$ | $1-s < S_{sm} < 1+s$ | $p-s < S_{pm} < p+s$ | ✓        | $\alpha_{sp}$ | $\S$ Fewell                 |
| 15   | $1-p < S_{sp} < 1+p$ | $1-s < S_{sm} < 1+s$ | $S_{pm} \leq p-s$    | ✓        | $\alpha_{sp}$ | 0                           |
| 16   | $1-p < S_{sp} < 1+p$ | $S_{sm} \leq 1-s$    | $S_{pm} \geq p+s$    | ✓        | $\alpha_{sp}$ | $\pi s^2$                   |
| 17   | $1-p < S_{sp} < 1+p$ | $S_{sm} \leq 1-s$    | $p-s < S_{pm} < p+s$ | ✓        | $\alpha_{sp}$ | $\pi s^2 - \alpha_{pm}$     |
| 18   | $1-p < S_{sp} < 1+p$ | $S_{sm} \leq 1-s$    | $S_{pm} \leq p-s$    | ✓        | $\alpha_{sp}$ | 0                           |
| 19   | $S_{sp} \leq 1+p$    | $S_{sm} \geq 1+s$    | $S_{pm} \geq p+s$    | ✓        | $\pi p^2$     | 0                           |
| 20   | $S_{sp} \leq 1+p$    | $S_{sm} \geq 1+s$    | $p-s < S_{pm} < p+s$ | ✓        | –             | –                           |
| 21   | $S_{sp} \leq 1+p$    | $S_{sm} \geq 1+s$    | $S_{pm} \leq p-s$    | ✓        | –             | –                           |
| 22   | $S_{sp} \leq 1+p$    | $1-s < S_{sm} < 1+s$ | $S_{pm} \geq p+s$    | ✓        | $\pi p^2$     | $\alpha_{sm}$               |
| 23   | $S_{sp} \leq 1+p$    | $1-s < S_{sm} < 1+s$ | $p-s < S_{pm} < p+s$ | ✓        | $\pi p^2$     | $\alpha_{sm} - \alpha_{pm}$ |
| 24   | $S_{sp} \leq 1+p$    | $1-s < S_{sm} < 1+s$ | $S_{pm} \leq p-s$    | ✓        | –             | –                           |
| 25   | $S_{sp} \leq 1+p$    | $S_{sm} \leq 1-s$    | $S_{pm} \geq p+s$    | ✓        | $\alpha_{sp}$ | $\pi s^2$                   |
| 26   | $S_{sp} \leq 1+p$    | $S_{sm} \leq 1-s$    | $p-s < S_{pm} < p+s$ | ✓        | $\alpha_{sp}$ | $\pi s^2 - \alpha_{pm}$     |
| 27   | $S_{sp} \leq 1+p$    | $S_{sm} \leq 1-s$    | $S_{pm} \leq p-s$    | ✓        | $\alpha_{sp}$ | 0                           |

For some cases, the transiting areas are described by the area of intersection between any two circles,  $\alpha$ . The area of transit caused by an object of radius  $r$  transiting an object of radius  $R$ , with separation  $S$ , is

$$\alpha(R, r, S) = r^2 \kappa_0(R, r, S) + R^2 \kappa_1(R, r, S) - \kappa_2(R, r, S), \quad (4.38)$$

$$\kappa_0(R, r, S) = \cos^{-1} \frac{S^2 + r^2 - R^2}{2Sr}, \quad (4.39)$$

$$\kappa_1(R, r, S) = \cos^{-1} \frac{S^2 - r^2 + R^2}{2SR}, \quad (4.40)$$

$$\kappa_2(R, r, S) = \sqrt{\frac{4S^2R^2 - (R^2 + S^2 - r^2)^2}{4}} . \quad (4.41)$$

### Case 14 (Fewell case)

Case 14 is the most complicated case to consider, because the planet's shadow and moon's shadow do not completely eclipse the star and there is possibility that they overlap each other. Therefore, the transiting area is described by area of intersection of three circles. Fewell (2006) presented the solution showing that the intersection points of three circles can be written as,

#### Star-planet intersection

$$x_{sp} = \frac{1 - p^2 + S_{sp}^2}{2S_{sp}} . \quad (4.42)$$

$$y_{sp} = \frac{1}{2S_{sp}} \sqrt{2S_{sp}^2(1 + p^2) - (1 - p^2)^2 - S_{sp}^4} . \quad (4.43)$$

#### Star-moon intersection

$$x_{sm} = x'_{sm} \cos \theta' - y'_{sm} \sin \theta' . \quad (4.44)$$

$$y_{sm} = x'_{sm} \sin \theta' + y'_{sm} \cos \theta' . \quad (4.45)$$

where

$$x'_{sm} = \frac{1 - s^2 + S_{sm}^2}{2S_{sm}} . \quad (4.46)$$

$$y'_{sm} = \frac{-1}{2S_{sm}} \sqrt{2S_{sm}^2(1 + s^2) - (1 - s^2)^2 - S_{sm}^4} . \quad (4.47)$$

$$\cos \theta' = \frac{S_{sp}^2 + S_{sm}^2 - S_{pm}^2}{2S_{sp}S_{sm}} . \quad (4.48)$$

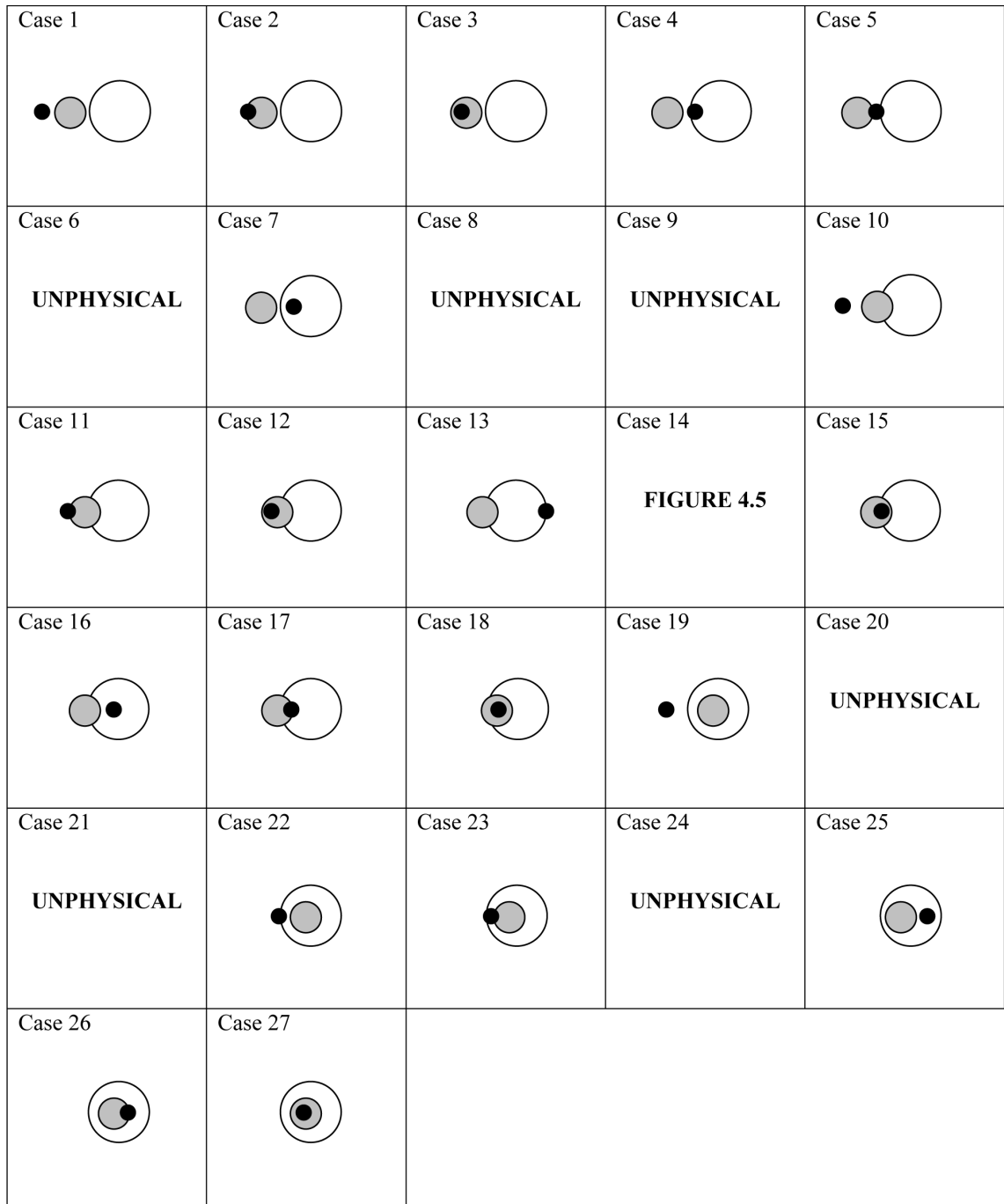


Figure 4.4: Diagrams of cases 1-27 show star (white sphere), planet (gray sphere) and moon (black sphere).

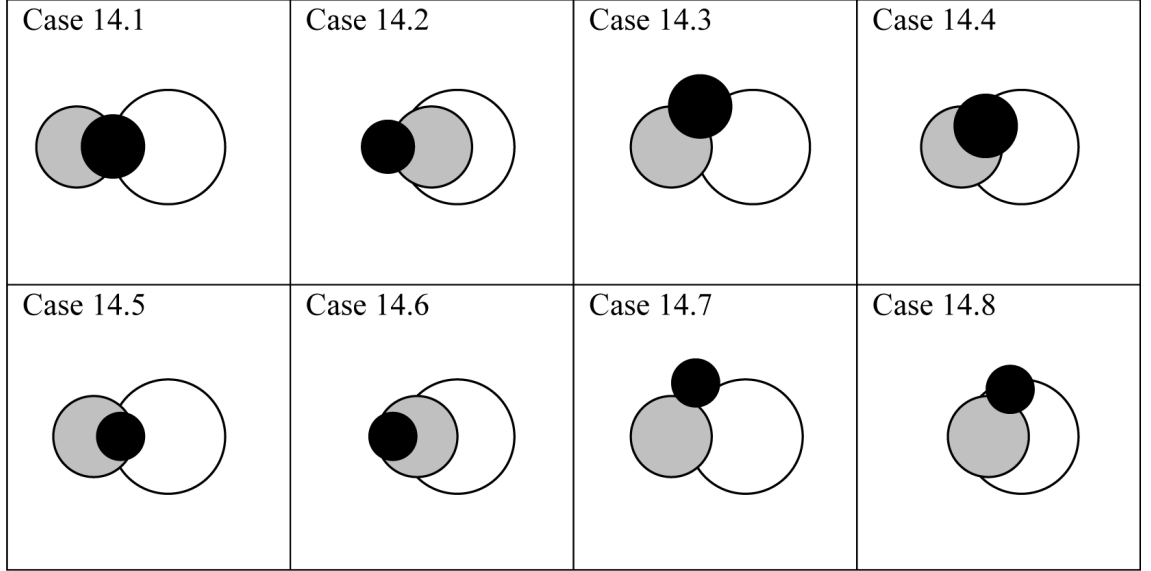


Figure 4.5: Diagrams of cases 14 show star (white sphere), planet (gray sphere) and moon (black sphere).

$$\sin \theta' = \sqrt{1 - \cos^2 \theta'} . \quad (4.49)$$

### Planet-moon intersection

$$x_{pm} = x''_{pm} \cos \theta'' - y''_{pm} \sin \theta'' + S_{sp} . \quad (4.50)$$

$$y_{pm} = x''_{pm} \sin \theta'' + y''_{pm} \cos \theta'' . \quad (4.51)$$

where

$$x''_{pm} = \frac{p^2 - s^2 + S_{pm}^2}{2S_{pm}} . \quad (4.52)$$

$$y''_{pm} = \frac{1}{2S_{pm}} \sqrt{2S_{pm}^2(p^2 + s^2) - (p^2 - s^2)^2 - S_{pm}^4} . \quad (4.53)$$

$$\cos \theta'' = -\frac{S_{sp}^2 + S_{pm}^2 - S_{sm}^2}{2S_{sp}S_{pm}} . \quad (4.54)$$

$$\sin \theta'' = \sqrt{1 - \cos^2 \theta''} . \quad (4.55)$$

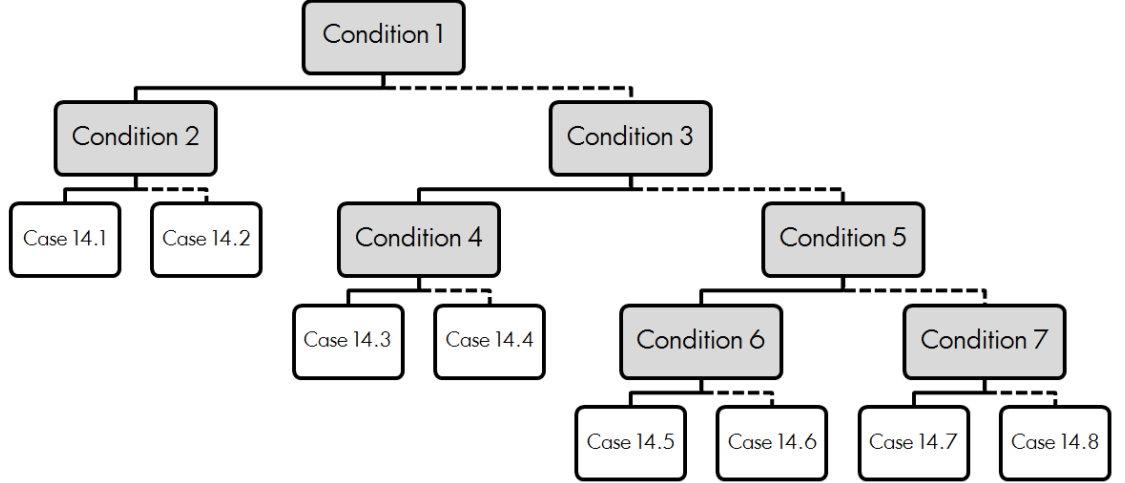


Figure 4.6: Decision flow chart of Case 14. Gray boxes are the decision conditions and white boxes are subcases of Case 14. The solid lines indicate a true statement and the dashed lines indicate a false statement.

In order to calculate the transit area of the moon, there are seven conditions that the simulation may take into account. The list of conditions is shown in Equation 4.56.

$$\begin{aligned}
 \text{Condition 1} & \quad (x_{sp} - S_{sm} \cos \theta')^2 + (y_{sp} + S_{sm} \sin \theta')^2 < s^2 \\
 \text{Condition 2} & \quad S_{sp} > 1 \\
 \text{Condition 3} & \quad (x_{sp} - S_{sm} \cos \theta')^2 + (y_{sp} - S_{sm} \sin \theta')^2 < s^2 \\
 \text{Condition 4} & \quad S_{sm} \sin \theta' > y_{sm} + \frac{y_{pm} - y_{sm}}{x_{pm} - x_{sm}} (S_{sm} \cos \theta' - x_{sm}) \\
 \text{Condition 5} & \quad (x_{sm} - S_{sp})^2 + y_{sm}^2 < p^2 \\
 \text{Condition 6} & \quad (S_{sm} - s) < (S_{pm} - p) \\
 \text{Condition 7} & \quad x_{pm}^2 + y_{pm}^2 < 1 \tag{4.56}
 \end{aligned}$$

The decision flow chart for calculating moon's transiting area of Case 14 is shown in Figure 4.6. In Table 4.4, the transiting areas of the moon in each subcase of Case 14 are listed.

Table 4.4: Moon active transit component of Case 14 (Kipping, 2011).

| Case | Ratio of Area ( $A_m$ )                             |
|------|---|
| 14.1 | $\alpha_{sm} - \alpha_{sp}$                         |
| 14.2 | $\pi p^2 - \alpha_{pm} - \alpha_{sp} + \alpha_{sm}$ |
| 14.3 | $\alpha_{sm} - \alpha_{14.3}$                       |
| 14.4 | $\alpha_{sm} - \alpha_{14.4}$                       |
| 14.5 | $\pi s^2 - \alpha_{pm}$                             |
| 14.6 | 0   |
| 14.7 | $\alpha_{sm}$                                       |
| 14.8 | $\alpha_{sm} - \alpha_{pm}$                         |

$$\begin{aligned}
\alpha_{14.3} = & \frac{1}{4} \sqrt{(c_1 + c_2 + c_3)(-c_1 + c_2 + c_3)(c_1 - c_2 + c_3)(c_1 + c_2 - c_3)} \\
& + \sum_{k=1}^3 \left( R_k^2 \arcsin \frac{c_k}{2R_k} \right) - \frac{c_1}{4} \sqrt{4R_1^2 - c_1^2} \\
& - \frac{c_2}{4} \sqrt{4R_2^2 - c_2^2} - \frac{c_3}{4} \sqrt{4R_3^2 - c_1^2} , \tag{4.57}
\end{aligned}$$

and

$$\begin{aligned}
\alpha_{14.4} = & \frac{1}{4} \sqrt{(c_1 + c_2 + c_3)(-c_1 + c_2 + c_3)(c_1 - c_2 + c_3)(c_1 + c_2 - c_3)} \\
& + \sum_{k=1}^3 \left( R_k^2 \arcsin \frac{c_k}{2R_k} \right) - \frac{c_1}{4} \sqrt{4R_1^2 - c_1^2} \\
& - \frac{c_2}{4} \sqrt{4R_2^2 - c_2^2} + \frac{c_3}{4} \sqrt{4R_3^2 - c_1^2} , \tag{4.58}
\end{aligned}$$

where  $R_k$  is radius of object and  $c_k$  is chord lengths,

$$c_k^2 = (x_{ik} - x_{jk})^2 + (y_{ik} - y_{jk})^2 . \tag{4.59}$$

## 4.4 Kepler photometry

The *Kepler* mission has been observing a 105 square degree field of view (FOV) in

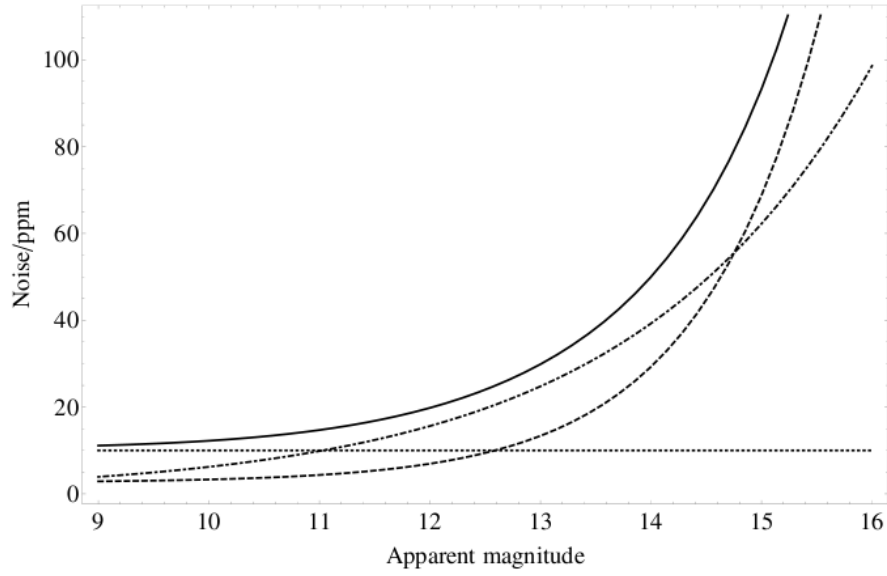


Figure 4.7: Instrument noise (dashed), photon noise (dot-dashed), stellar variability (dotted) and total noise (solid) of *Kepler* class photometry as a function of apparent magnitude of stars (Kipping et al., 2009).

Cygnus in search for Earth-size transit planets in habitable zones of main-sequence stars. The mission is designed to monitor 150,000 stars brighter than 16<sup>th</sup> magnitude in *Kepler* the passband with 20 parts per million photometric precision at 12<sup>th</sup> magnitude in 6.5 hours (Batalha et al., 2010; Caldwell et al., 2010b). In order to meet this requirement, the estimated photon collection rate of *Kepler* is (Borucki et al., 2005; Kipping et al., 2009; Yee & Gaudi, 2008),

$$\Gamma_{ph} = 6.3 \times 10^8 \text{ h}^{-1} 10^{-0.4(m-12)} \text{ photons/hours}, \quad (4.60)$$

where  $m$  is the apparent magnitude. However, *Kepler* photometry is also affected by shot noise, background flux and instrumental noise.

### Shot noise

Shot noise or Poisson noise comes from the discrete nature of photons. At 12<sup>th</sup> magnitude, the largest noise component is the Poisson noise of the target (Caldwell et al., 2010b). In order to generate this noise, the Poisson distribution is used in this dissertation.

## Background flux

The background flux for *Kepler* comes from zodiacal light from the solar system and diffuse starlight from background stars. In pre-launch prediction, the background flux is estimated at around  $334 \text{ e}^- \text{ sec}^{-1}$  or 22 magnitudes per square arc-second (Caldwell et al., 2010b). However, in real observations, the background flux varies across detectors and with orientation of the telescope. Therefore, the pre-launch background flux is used to generate background flux of the light curves in this work.

## Instrumental noise

There are two main instrumental noises for *Kepler*: read noise and dark current. From in-flight measurement, the read noise median value is  $95 \text{ e}^- \text{ read}^{-1}$  and dark current is  $0.25 \text{ e}^- \text{ pixel}^{-1} \text{ s}^{-1}$  which is quite low compared to the photons collected from the targets (Caldwell et al., 2010a).

Table 4.5: *Kepler* photometry properties.

| Parameter   | Value  |
|---|--------|
| Exposure time (s)   | 6.02 * |
| Plate scale (arcseconds/pixel)                                  | 3.98 † |
| Background flux ( $\text{e}^- \text{ s}^{-1}$ )                 | 334 †  |
| Read Noise ( $\text{e}^- \text{ read}^{-1}$ )                   | 95 ‡   |
| Dark Current ( $\text{e}^- \text{ pixel}^{-1} \text{ s}^{-1}$ ) | 0.25 ‡ |

\* : Van Cleve & Caldwell (2009)

‡ : Caldwell et al. (2010a)

† : Caldwell et al. (2010b)

## 4.5 Modelling habitable exomoons

Although no exomoons have yet been discovered, there have been a number of studies on habitable exomoons. In this work, the assumptions of Barnes & O'Brien (2002) are followed. They proposed that habitable exomoons should be Earth-like

mass moons orbiting around habitable-zone Jupiter-like planets around M-dwarf stars.

### 4.5.1 Properties of the host star

In this analysis, M-Dwarf stars are selected to be the exoplanet host stars. Very cool (late K and early M type) dwarf stars have become popular targets of planet searches because of easy planet detection, because the amplitudes of the transits generated by small planets in M-dwarfs are larger than those generated by hotter stars (Bean et al., 2010a; Charbonneau et al., 2009; Mann et al., 2012; Vogt et al., 2010). Therefore, the detectable planets in M-Dwarf systems can still orbit within the HZ (Gaidos et al., 2007).

For the *Kepler* mission, a region of the extended solar neighbourhood in the Cygnus region along the Orion arm centred in the 105 deg<sup>2</sup> FOV is chosen. In this region, there are about 0.5 million stars brighter than 16<sup>th</sup> magnitude in the *Kepler* passband, however, only 10<sup>5</sup> stars with magnitude less than 16<sup>th</sup> were expected to be exoplanet hosts. In 2010, the *Kepler* mission announced 150,000 highest priority target stars, but only 2% of these target stars have effective temperature less than 3500 K which might be M-Dwarfs (Table 4.6) (Batalha et al., 2010), whereas > 70% of all stars within 20 pc are M-Dwarfs (Chabrier, 2003; Henry et al., 1994; Reid et al., 2004). However, in 2011, the team released additional exoplanet data, including 997 planet-candidate host stars in which 74 (> 5%) have effective temperature less than 4400 K in the *Kepler* Input Catalog (Batalha et al., 2010; Borucki et al., 2011b; Brown et al., 2011).

Although, the statistics of planets around late-type stars remain poorly established within the *Kepler* target list (Mann et al., 2012). Two important conclusions can be drawn about late-type exoplanet hosts from recent *Kepler* results. First, the frequency of stars with planets on close-in ( $P_p < 50$  days) orbits decreases with stellar effective temperature (Howard et al., 2012). More than 15% of dwarf hosts have planets with orbital periods less than 50 days (Figure 4.8) (Howard et al., 2010,

Table 4.6: The number of highest priority *Kepler* target stars as a function of effective temperature and apparent magnitude (Batalha et al., 2010).

| Mag              | 10500 | 9500 | 8500 | 7500 | 6500  | 5500  | 4500  | 3500 | Total  |
|------------------|-------|------|------|------|-------|-------|-------|------|--------|
| $\log g \gg 3.5$ |       |      |      |      |       |       |       |      |        |
| 6.50             | 1     | 0    | 1    | 2    | 0     | 1     | 0     | 0    | 5      |
| 7.50             | 1     | 8    | 9    | 6    | 8     | 6     | 0     | 0    | 38     |
| 8.50             | 8     | 20   | 25   | 24   | 49    | 15    | 7     | 8    | 156    |
| 9.50             | 9     | 31   | 81   | 66   | 116   | 88    | 11    | 4    | 406    |
| 10.50            | 27    | 37   | 100  | 209  | 405   | 359   | 40    | 9    | 1186   |
| 11.50            | 24    | 58   | 171  | 398  | 1499  | 1356  | 158   | 37   | 3701   |
| 12.50            | 30    | 44   | 231  | 676  | 4146  | 4760  | 626   | 62   | 10575  |
| 13.50            | 34    | 53   | 170  | 747  | 9279  | 15866 | 2213  | 157  | 28519  |
| 14.50            | 3     | 0    | 0    | 0    | 4855  | 29352 | 4227  | 554  | 38991  |
| 15.50            | 7     | 4    | 0    | 0    | 4449  | 42627 | 12093 | 1961 | 61141  |
| Total            | 144   | 255  | 788  | 2128 | 24806 | 94430 | 19375 | 2792 | 144718 |
| $\log g < 3.5$   |       |      |      |      |       |       |       |      |        |
| 6.50             | 0     | 0    | 0    | 0    | 0     | 0     | 0     | 0    | 0      |
| 7.50             | 0     | 0    | 1    | 1    | 2     | 2     | 7     | 0    | 13     |
| 8.50             | 0     | 0    | 1    | 2    | 2     | 9     | 80    | 2    | 96     |
| 9.50             | 0     | 0    | 2    | 15   | 2     | 27    | 220   | 1    | 267    |
| 10.50            | 1     | 0    | 5    | 21   | 7     | 99    | 452   | 2    | 587    |
| 11.50            | 0     | 0    | 1    | 25   | 11    | 186   | 674   | 2    | 899    |
| 12.50            | 0     | 0    | 1    | 12   | 14    | 347   | 626   | 62   | 1488   |
| 13.50            | 0     | 0    | 0    | 6    | 5     | 518   | 1403  | 0    | 1932   |
| 14.50            | 0     | 0    | 0    | 0    | 0     | 0     | 0     | 0    | 0      |
| 15.50            | 0     | 0    | 0    | 0    | 0     | 0     | 0     | 0    | 0      |
| Total            | 1     | 0    | 11   | 82   | 43    | 1188  | 3950  | 7    | 5282   |

2012). Second, the number of planets per star increases with orbital period (Figure 4.9) (Howard et al., 2012). Therefore, researching M-Dwarfs planetary systems is important.

The M-dwarf stars with mass  $0.5 M_{\odot}$  and radius  $0.55 R_{\odot}$  are chosen to be the target in this work. Their effective temperature, microturbulent velocity and  $\log g$  are set to be 3500 K,  $1 \text{ km.s}^{-1}$  and 4.5, respectively. In order to calculate the limb darkening coefficient, the metallicity of M-dwarfs has to be defined.

However, determining the metallicity of M-dwarfs is very difficult because of the existence of many molecules in their cool atmospheres (Schlaufman & Laughlin, 2010). There have been several attempts to obtain the metallicity of M-Dwarfs using their photometric properties. In 2010, Schlaufman & Laughlin used the calibration samples of Bonfils et al. (2005) and Johnson & Apps (2009) to plot the distribution of residuals between each model and observation. They found that the mean value of the Bonfils et al. (2005) residuals is 0.12 dex with standard deviation 0.16 dex

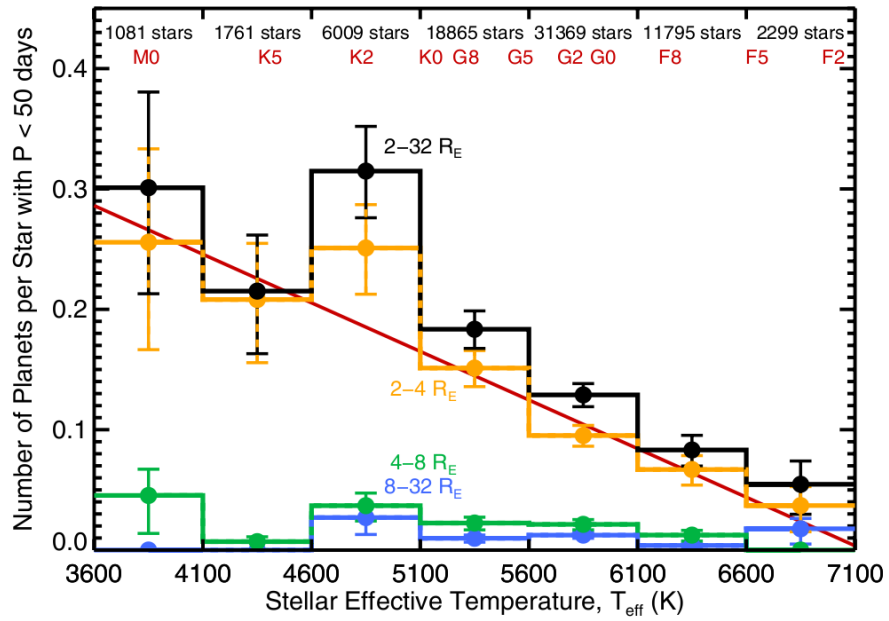


Figure 4.8: The occurrence of planets with period less than 50 days as a function of stellar effective temperature (Howard et al., 2012).

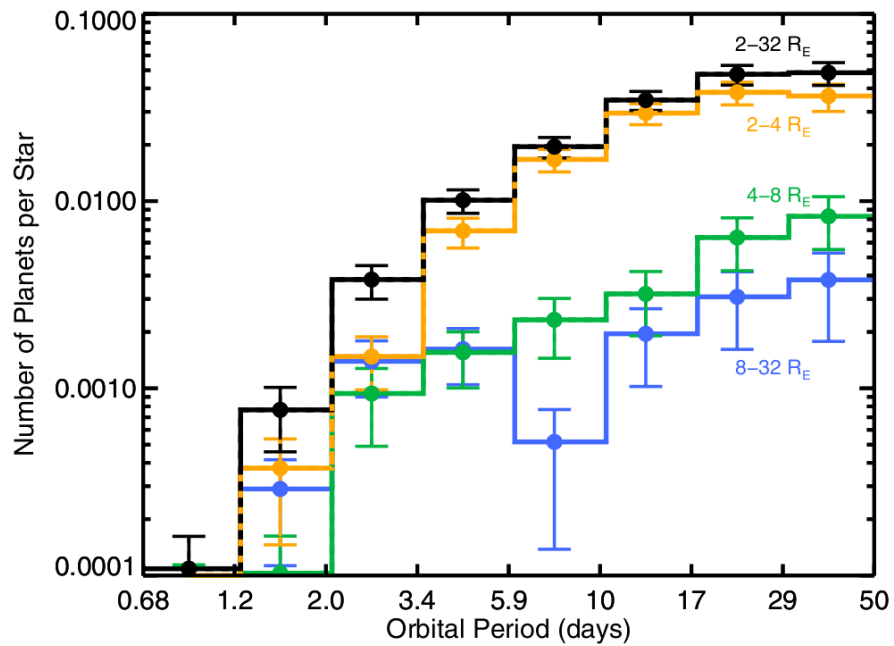


Figure 4.9: The occurrence of planets with radii of  $2-32 R_{\oplus}$  as a function of orbital period (Howard et al., 2012).

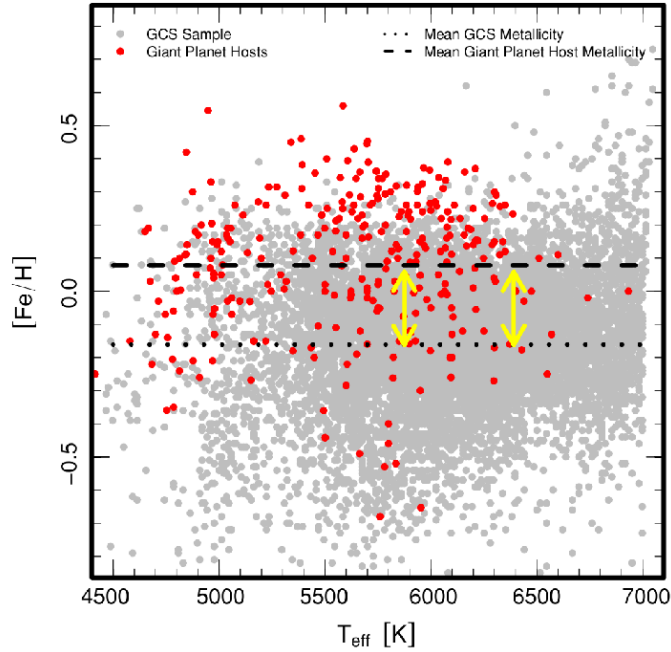


Figure 4.10: Scatter plot between effective temperature and metallicity for neighbouring stars and confirmed giant planet hosts (Schlaufman & Laughlin, 2011).

and the mean value of the Johnson & Apps (2009) residuals is -0.12 dex with standard deviation 0.12 dex (Bonfils et al., 2005; Johnson & Apps, 2009; Schlaufman & Laughlin, 2010). In 2011, Schlaufman & Laughlin found that the host stars of the *Kepler* planet candidates are preferentially metal-rich, including the low-mass stars with small radius planet. In Figure 4.10, the plot between effective temperature and metallicity for neighbouring stars and confirmed giant planet hosts are shown (Holmberg et al., 2007, 2009; Schlaufman & Laughlin, 2011; Wright et al., 2011). In conclusion, the solar-metallicity stars are chosen in this work.

Finally, in this work, a quadratic limb-darkening model is used. The values of quadratic limb-darkening coefficients of host stars for the transmission curves of *Kepler* are obtained from Claret & Bloemen (2011). For M-Dwarfs hosts, the value of  $\gamma_1$  and  $\gamma_2$  are 0.4042 and 0.3268, respectively<sup>2</sup>.

## 4.5.2 Properties of the host planet

For the host planet, Jupiter-like giant planets which offer the best potential for hosting habitable exomoons are considered (Barnes & O’Brien, 2002). Giant planets

<sup>2</sup>See <http://cdsarc.u-strasbg.fr/viz-bin/qcat?J/A+A/529/A75>

with masses ranging logarithmically from  $15.0$  to  $150.0 M_{\oplus}$  and with circular orbits are chosen. In order to investigate habitable exoplanets and exomoons, the planet-star separations are set to be in the HZ of an M-Dwarf, starting at a separation of  $0.10$  AU and increasing in logarithmic increments to a separation of  $0.66$  AU.

In 2007, Fortney et al. found that the radii of giant planets depend on their masses, core masses and separations. For giant planets at  $4.5$  Gyr, their radii fall between  $1.0$  and  $1.2 R_J$  (Figure 4.11) (Fortney et al., 2007b). In conclusion,  $1.2$  Jupiter radius planets are chosen in the simulation.

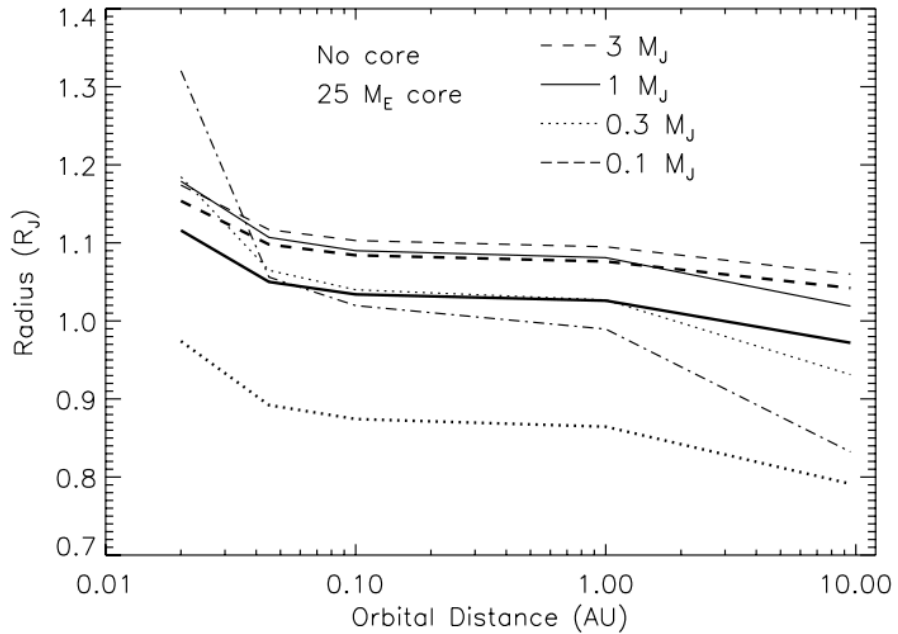


Figure 4.11: Planetary radii of coreless planets (thin lines) and planets with a core of  $25 M_{\oplus}$  of heavy elements (thick lines) at  $4.5$  Gyr as a function of orbital distance from the Sun (Fortney et al., 2007b).

### 4.5.3 Properties of the exomoon

No exomoons have yet been discovered, therefore, the properties of Earth-like planets in this work are used for the properties of a habitable exomoon. Rocky planets with logarithmic mass between  $1.0$  and  $10.0 M_{\oplus}$  are chosen. The radius of the moon is calculated from Fortney's model, using rock mass fraction (rmf) equal to  $0.66$  (Earth-like planet).

$$\begin{aligned}
 R_m = & (0.0592\text{rmf} + 0.0975)(\log M_m)^2 \\
 & + 0.2337\text{rmf} + 0.4938) \log M_m + 0.3102\text{rmf} + 0.7932 , \quad (4.61)
 \end{aligned}$$

where  $M_m$  and  $R_m$  are the moon's mass and moon's radius in  $M_\oplus$  and  $R_\oplus$ , respectively (Fortney et al., 2007a,b). Finally, only a moon within the planet's Hill sphere with an orbital period between 1.00 to 3.16 days is considered. For simplicity, circular orbits are assumed.

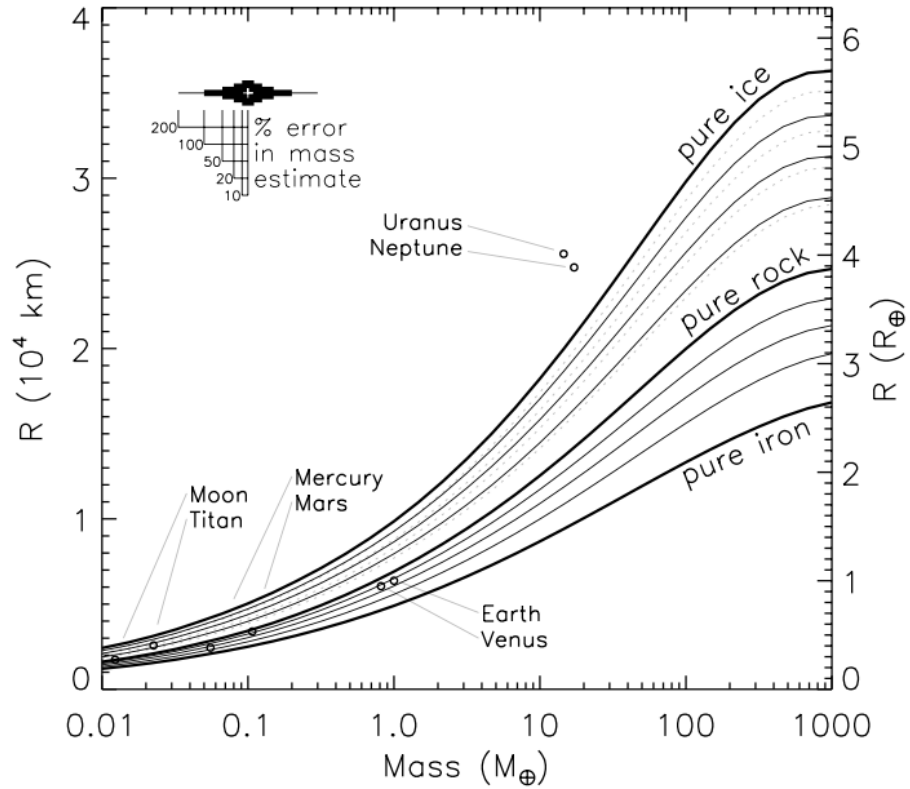


Figure 4.12: Planetary radii of rocky planets as a function of masses (Fortney et al., 2007b).

## 4.6 Measuring TTV-TDV signals

In order to find the transit time of minima and transit duration, the simulated light curves are fitted. The light curves are divided into phase bins using the period. A straight line is fitted to every three points of phased data. The fits with minimum

and maximum slopes are chosen to define the start and end of the transit. The intersection between the median of data and the minimum and maximum slopes are used to define ingress ( $t_{ing}$ ) and egress ( $t_{egr}$ ) times, respectively (Figure 4.13). The time of minimum light ( $t_0$ ) and the transit duration ( $\bar{\tau}$ ) are defined as,

$$t_0 = \frac{t_{ing} + t_{egr}}{2} , \quad (4.62)$$

and

$$\bar{\tau} = t_{egr} - t_{ing} . \quad (4.63)$$

Using mid-transit time, the new ephemeris as a function of epoch is derived. The new ephemeris is determined by fitting a linear function to the mid-transit points.

$$T_0(n) = T_0(0) + nP , \quad (4.64)$$

where  $n$  is epoch and  $T_0$  is time of minimum light as a function of epoch. The residual of transit time of minima and transit duration are used to be the TTV and TDV signal of the system.

## 4.7 TTV-TDV correlation testing

Holman & Murray (2005) showed that planetary bodies could induce TTV on a transiting planet. Therefore, the TTV signal alone cannot distinguish between the effect of other planets and the effect of its satellite. In order to detect the exomoon, TDV signals must also be detected. From Section 3.2, TTV and TDV are sinusoidal functions and the TTV signal is 90 degrees out-of-phase with the TDV signal. However, in coplanar systems, the TDV signal is produced by only the TDV-V signal, because TDV-TIP does not exist (Section 3.3.2) (Kipping, 2009b). Therefore, in theory, the plot between the square of the TTV signal and square of the TDV signal should show a perfect linear relationship with negative slope. However, there are other effects, such as star spots, instrument noise and observation cadence

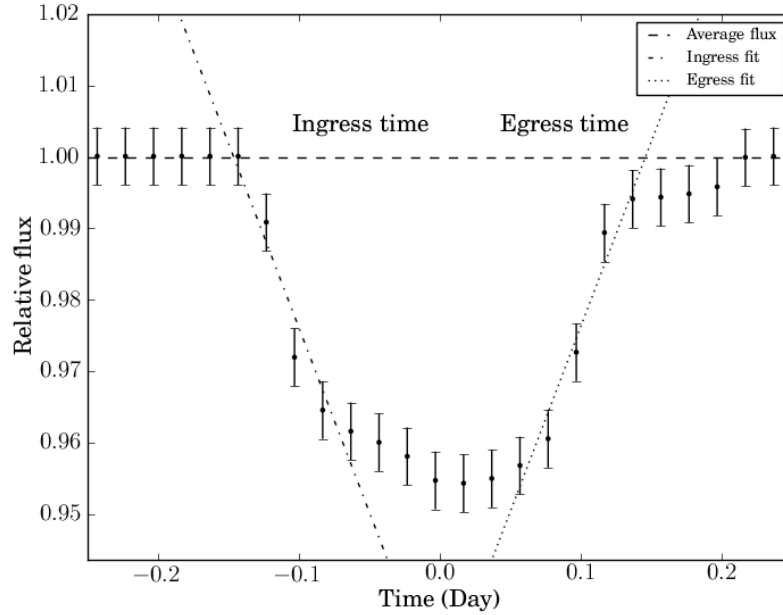


Figure 4.13: Light curves of a  $15 M_{\oplus}$  habitable-zone planet with a  $10 M_{\oplus}$  moon for an M2 host star with planet period 89.35 days and moon period 2.24 days. Error bars are shown at 1,000 times their true size. The fits show ingress time and egress time of transit, and average flux (median of flux data).

which could perturb the transiting light curve and produce false positive TTV and TDV signatures.

In this simulation, the instrument noise and observation cadence both affect the TTV and TDV signal. Thus, the plot between  $TTV^2$  and  $TDV^2$  may not show a clear linear relationship. In order to check this relationship, the Pearson product-moment correlation coefficient was calculated to test the correlation between  $TTV^2$  and  $TDV^2$  and defined as a detectability coefficient. The coefficient is

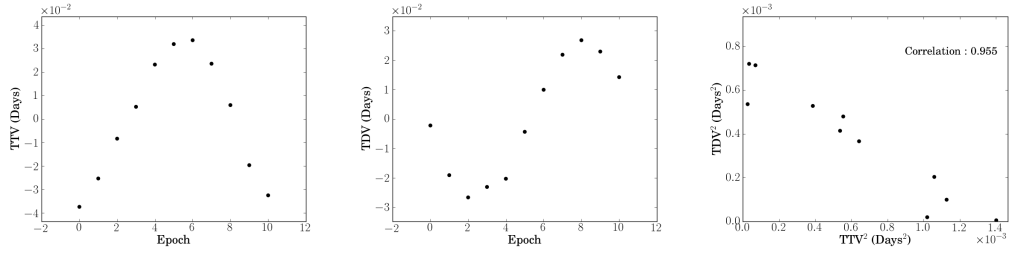
$$\chi = \frac{\sum_{i=1}^n (TTV_i^2 - \overline{TTV^2})(TDV_i^2 - \overline{TDV^2})}{\sqrt{\sum_{i=1}^n (TTV_i^2 - \overline{TTV^2})^2} \sqrt{\sum_{i=1}^n (TDV_i^2 - \overline{TDV^2})^2}}, \quad (4.65)$$

where  $TTV$  and  $TDV$  are the TTV and TDV signal, respectively. The negative coefficient is produced by an inverse or negative relationship between the two variables and a positive coefficient means there is a positive linear relationship between the two variables.

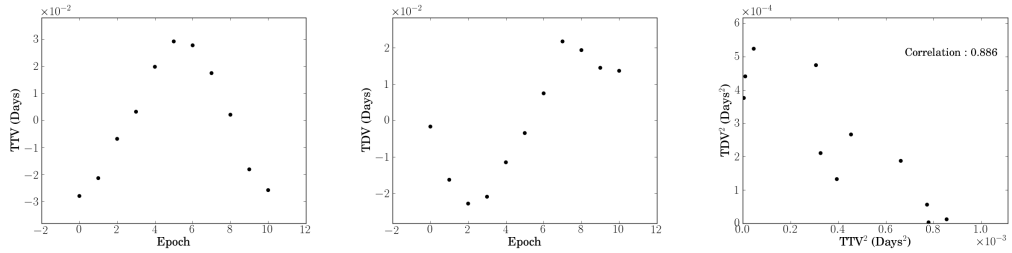
The plots between  $TTV^2$  and  $TDV^2$  of a  $10.0 M_{\oplus}$  exomoon around  $15.0$ - $150.0 M_{\oplus}$  exoplanet for M-Dwarf star, with planet period 89.35 days and moon period

2.24 days, and their TTV and TDV signals are shown in Figure 4.14. The plots with correlation less than -0.8 show stronger relationship between  $TTV^2$  and  $TDV^2$  signals which is good enough to provide reliable detection of exomoon.

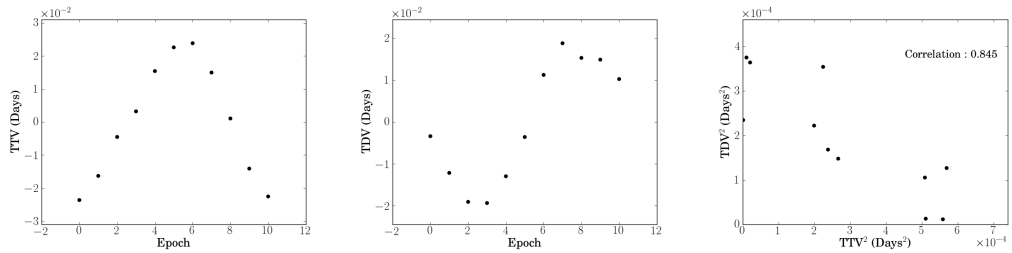
In this study, the positive coefficient will be set to be zero, because the positive slope of  $TTV^2$  and  $TDV^2$  plot means the TTV and TDV signal are not consistent with sinusoidal functions with 90 degrees phase difference. After the processing, the absolute values of coefficients are going to be considered.



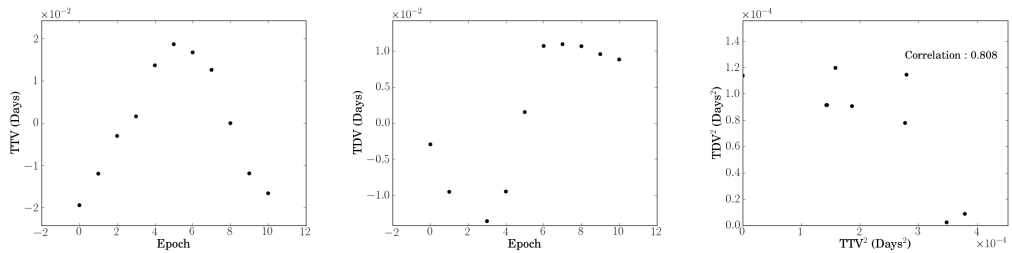
(a) 15.0 Earth-mass planet



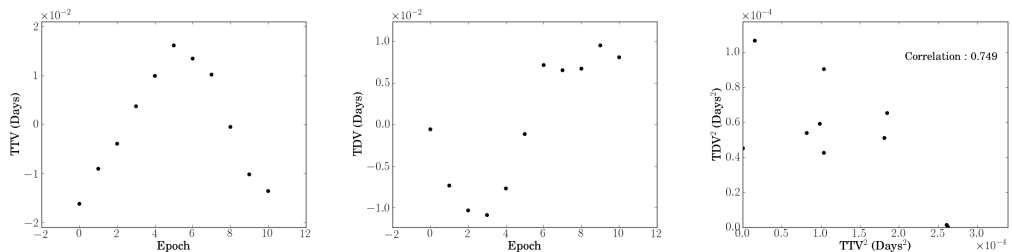
(b) 18.9 Earth-mass planet



(c) 23.8 Earth-mass planet

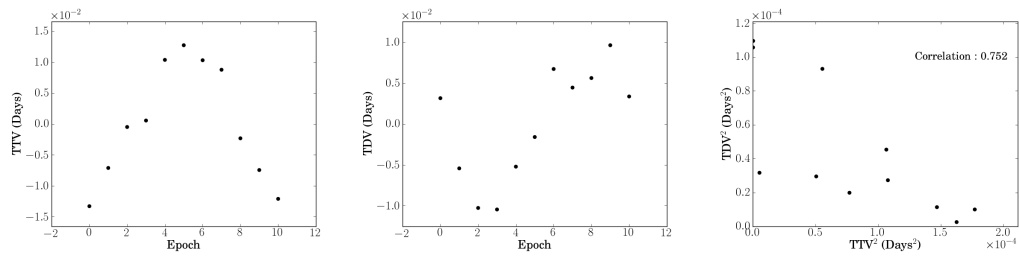


(d) 29.9 Earth-mass planet

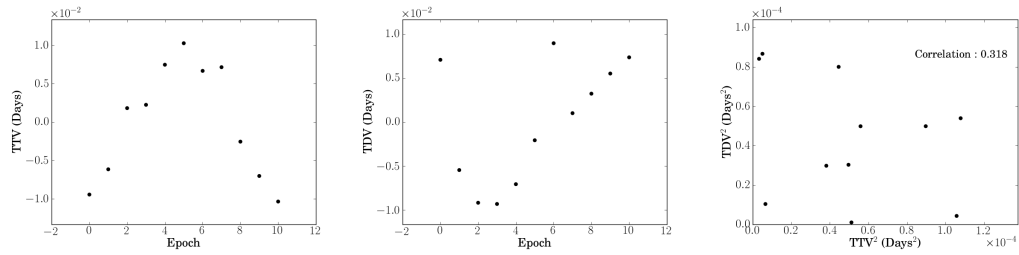


(e) 37.7 Earth-mass planet

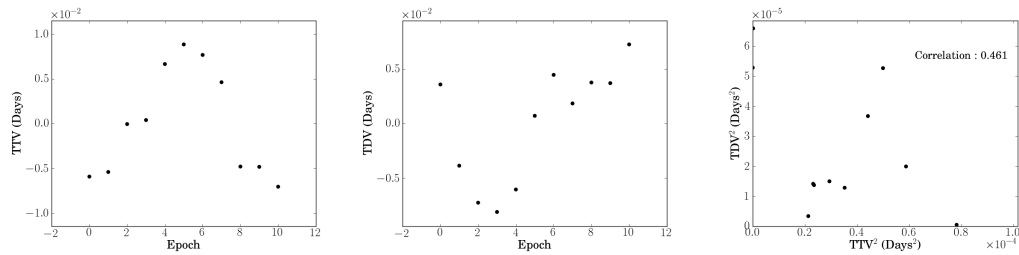
Figure 4.14: TTV signal (left), TDV signal (middle) and the plots between  $TTV^2$  and  $TDV^2$  (right) of a  $10.0 M_{\oplus}$  exomoon around  $15.0$ - $150.0 M_{\oplus}$  exoplanet for M-Dwarf star, with planet period 89.35 days and moon period 2.24 days.



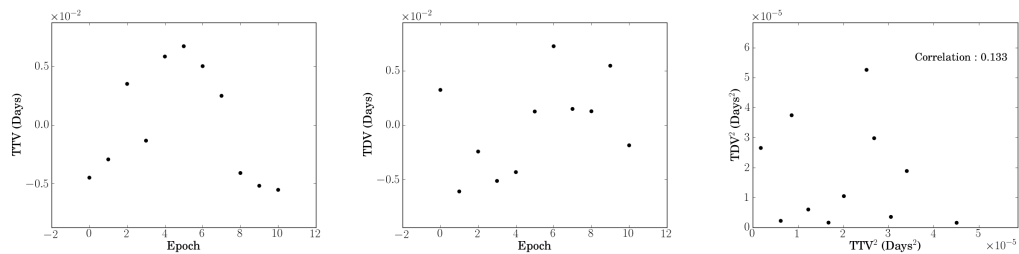
(f) 47.4 Earth-mass planet



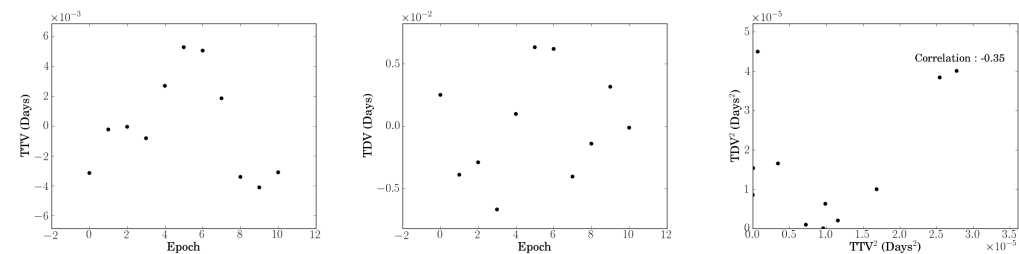
(g) 59.7 Earth-mass planet



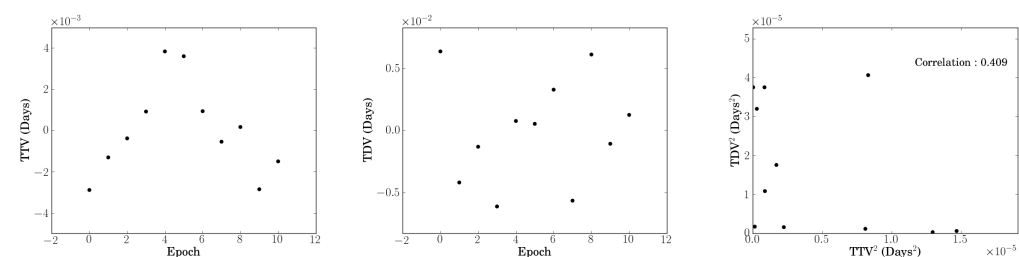
(h) 75.2 Earth-mass planet



(i) 94.6 Earth-mass planet



(j) 119.1 Earth-mass planet



(k) 150.0 Earth-mass planet

Figure 4.14: Continued

# Chapter 5

## Results and discussion

### 5.1 Detectability of habitable exomoons

The light curves are generated with and without *Kepler* photometric noise.  $11 \times 11 \times 11 \times 10$  light curves are simulated with 11 values of each four variable input parameters; planet mass, planet separation, moon mass and moon period, and 10 random initial phases. The host stars are assumed to be M-Dwarf stars of 12.5<sup>th</sup> magnitude in *Kepler* pass-bands. The cadence of this simulation is 50 data point per day (every 28.8 mins) which corresponds to *Kepler* long cadence (every 29.4 mins) (Gilliland et al., 2010). In order to simulate the current *Kepler* data, 3-years simulation of a transiting giant extrasolar planet with a rocky extrasolar moon was run to find out the detectability of an exomoon in the M-Dwarf habitable zone. The details of physical parameters of the systems are listed in Table 5.1.

In this simulation, there are four variable parameters; planet mass, planet separation, moon mass and moon period. The correlation projected on to a two parameter plane is plotted in order to find the relation between two variables. Light curves without photometric noise (From Figure 5.1 to Figure 5.6) and with *Kepler* noise (From Figure 5.7 to Figure 5.12) are simulated. The TTV and TDV signals of the light curve with noise are more scattered and their correlations are lower than correlations of noiseless light curves with the same input parameters. However, the correlation contours of the light curves without photometric noise and the light curves based

Table 5.1: Input parameters for the simulation.

| <b>Star parameters</b>                       |               |
|--|---------------|
| Star mass ( $M_{\odot}$ )                    | 0.5           |
| Star radius ( $R_{\odot}$ )                  | 0.55          |
| Star apparent magnitude ( $K_p$ )            | 12.5          |
| Quadratic limb-darkening coefficient 1       | 0.4042        |
| Quadratic limb-darkening coefficient 2       | 0.3268        |
| <b>Planet parameters</b>                     |               |
| Planet mass ( $M_{\oplus}$ )                 | 15.0-150.0    |
| Planet radius ( $R_{\oplus}$ )               | 10.97         |
| Planet separation (AU)                       | 0.10-0.66     |
| Planet eccentricity                          | 0.0           |
| Planet inclination (degrees)                 | 90.0          |
| Planet argument of periapsis (degrees)       | 0.0           |
| Planet longitude of ascending node (degrees) | 0.0           |
| <b>Moon parameters</b>                       |               |
| Moon mass ( $M_{\oplus}$ )                   | 1.0-10.0      |
| Moon radius ( $R_{\oplus}$ )                 | Equation 4.61 |
| Moon period (days)                           | 1.00-3.16     |
| Moon eccentricity                            | 0.0           |
| Moon inclination (degrees)                   | 90.0          |
| Moon argument of periapsis (degrees)         | 0.0           |
| Moon longitude of ascending node (degrees)   | 0.0           |

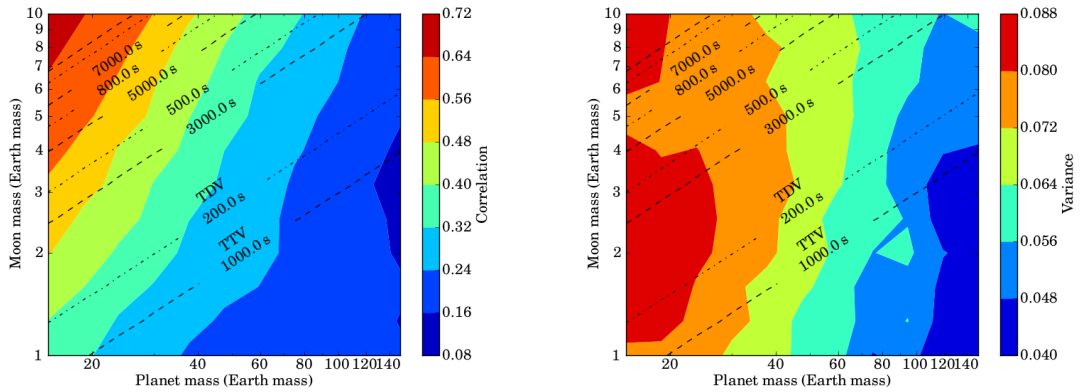


Figure 5.1: Correlation (left) and variance of correlation (right) contours between planet mass and moon mass of the light curves without *Kepler* photometric noise. The contour is averaged over logarithmic planet separation and moon period. The RMS amplitude of the TTV signal (dashed) and RMS amplitude of the TDV signal (dot-dashed) in units of seconds are presented.

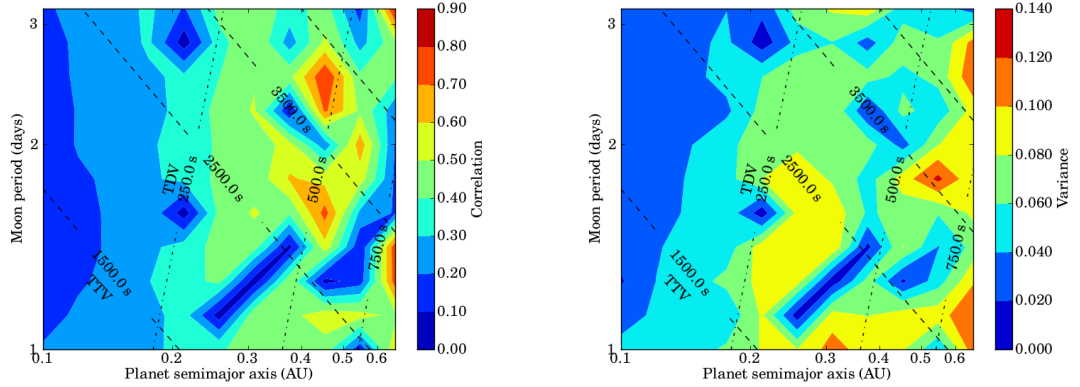


Figure 5.2: Correlation (left) and variance of correlation (right) contours between planet separation and moon period of the light curves without *Kepler* photometric noise. The contour is averaged over logarithmic planet mass and moon mass. The RMS amplitude of the TTV signal (dashed) and RMS amplitude of the TDV signal (dot-dashed) in units of seconds are presented.

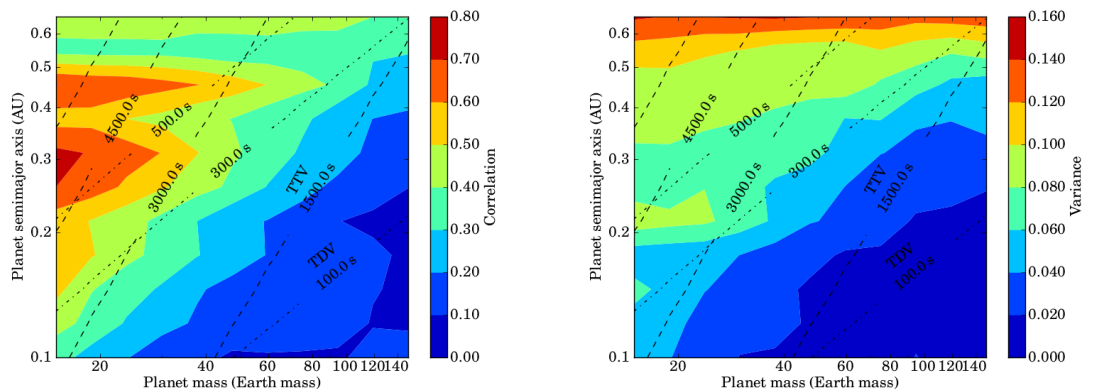


Figure 5.3: Correlation (left) and variance of correlation (right) contours between planet mass and planet separation of the light curves without *Kepler* photometric noise. The contour is averaged over logarithmic moon mass and moon period. The RMS amplitude of the TTV signal (dashed) and RMS amplitude of the TDV signal (dot-dashed) in units of seconds are presented.

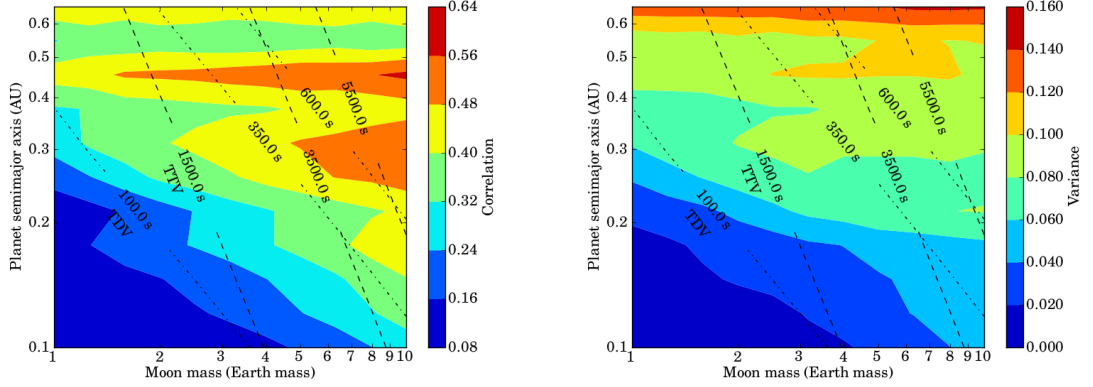


Figure 5.4: Correlation (left) and variance of correlation (right) contours between moon mass and planet separation of the light curves without *Kepler* photometric noise. The contour is averaged over logarithmic planet mass and moon period. The RMS amplitude of the TTV signal (dashed) and RMS amplitude of the TDV signal (dot-dashed) in units of seconds are presented.

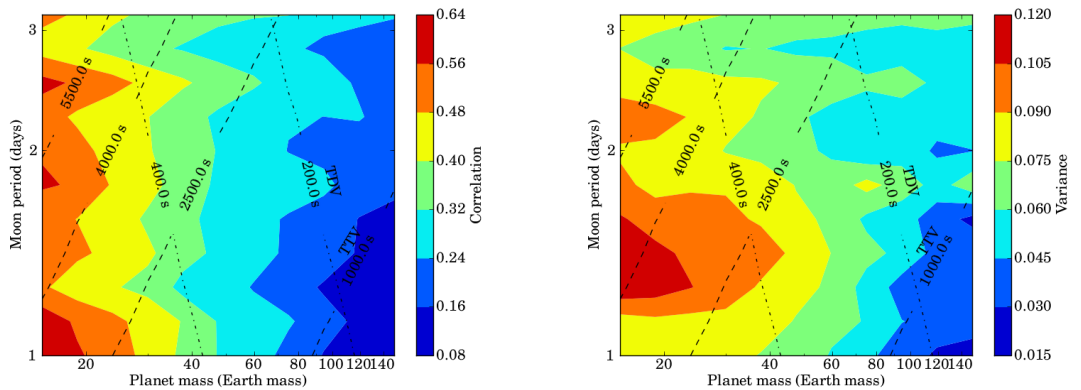


Figure 5.5: Correlation (left) and variance of correlation (right) contours between planet mass and moon period of the light curves without *Kepler* photometric noise. The contour is averaged over logarithmic planet separation and moon mass. The RMS amplitude of the TTV signal (dashed) and RMS amplitude of the TDV signal (dot-dashed) in units of seconds are presented.

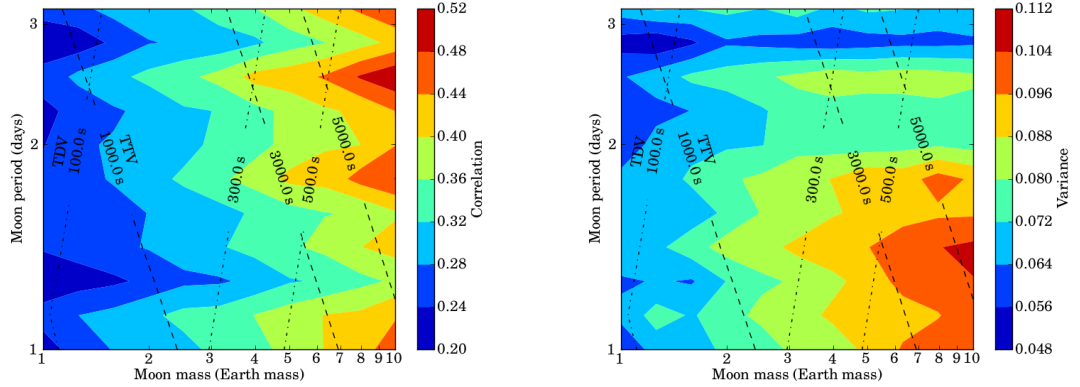


Figure 5.6: Correlation (left) and variance of correlation (right) contours between moon mass and moon period of the light curves without *Kepler* photometric noise. The contour is averaged over logarithmic planet mass and planet separation. The RMS amplitude of the TTV signal (dashed) and RMS amplitude of the TDV signal (dot-dashed) in units of seconds are presented.

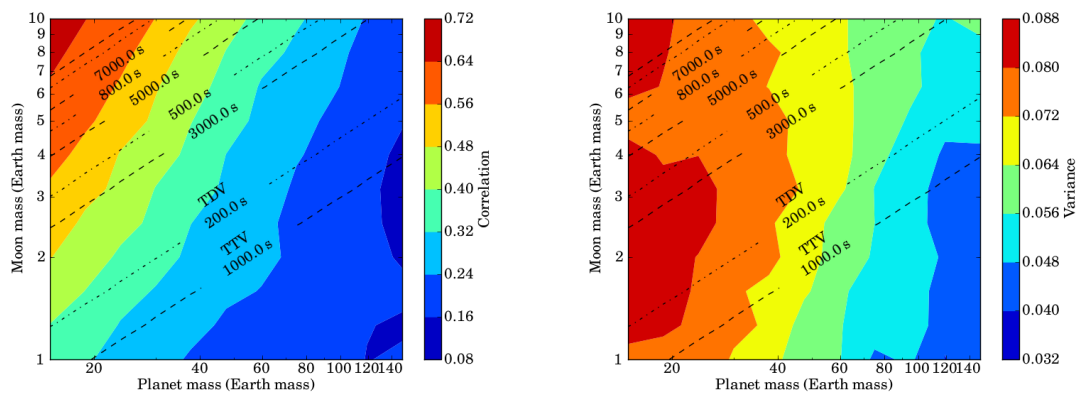


Figure 5.7: Correlation (left) and variance of correlation (right) contours between planet mass and moon mass of the light curves with *Kepler* photometric noise. The contour is averaged over logarithmic planet separation and moon period. The RMS amplitude of the TTV signal (dashed) and RMS amplitude of the TDV signal (dot-dashed) in units of seconds are presented.

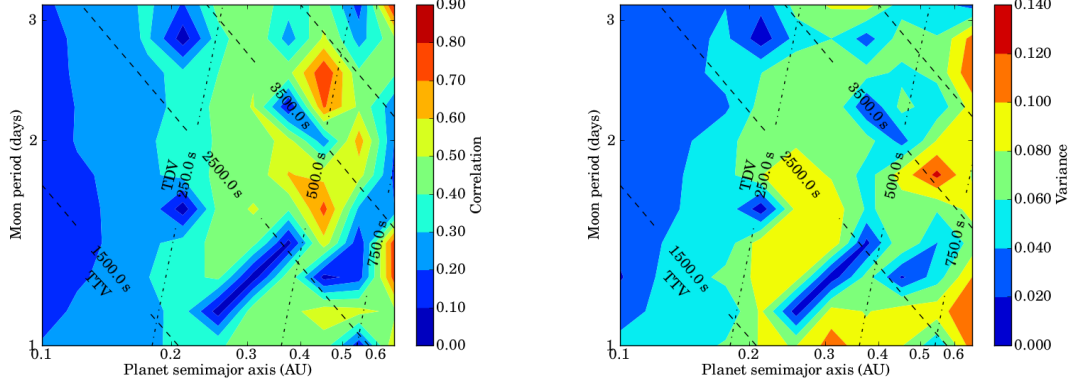


Figure 5.8: Correlation (left) and variance of correlation (right) contours between planet separation and moon period of the light curves with *Kepler* photometric noise. The contour is averaged over logarithmic planet mass and moon mass. The RMS amplitude of the TTV signal (dashed) and RMS amplitude of the TDV signal (dot-dashed) in units of seconds are presented.

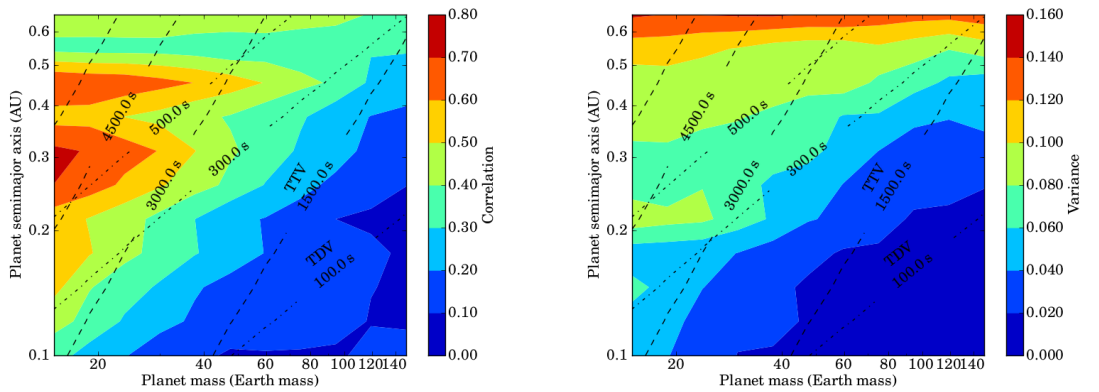


Figure 5.9: Correlation (left) and variance of correlation (right) contours between planet mass and planet separation of the light curves with *Kepler* photometric noise. The contour is averaged over logarithmic moon mass and moon period. The RMS amplitude of the TTV signal (dashed) and RMS amplitude of the TDV signal (dot-dashed) in units of seconds are presented.

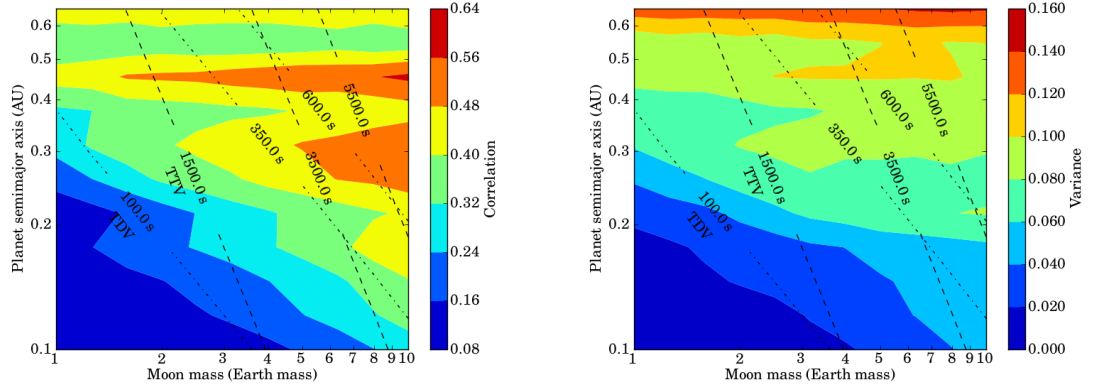


Figure 5.10: Correlation (left) and variance of correlation (right) contours between moon mass and planet separation of the light curves with *Kepler* photometric noise. The contour is averaged over logarithmic planet mass and moon period. The RMS amplitude of the TTV signal (dashed) and RMS amplitude of the TDV signal (dot-dashed) in units of seconds are presented.

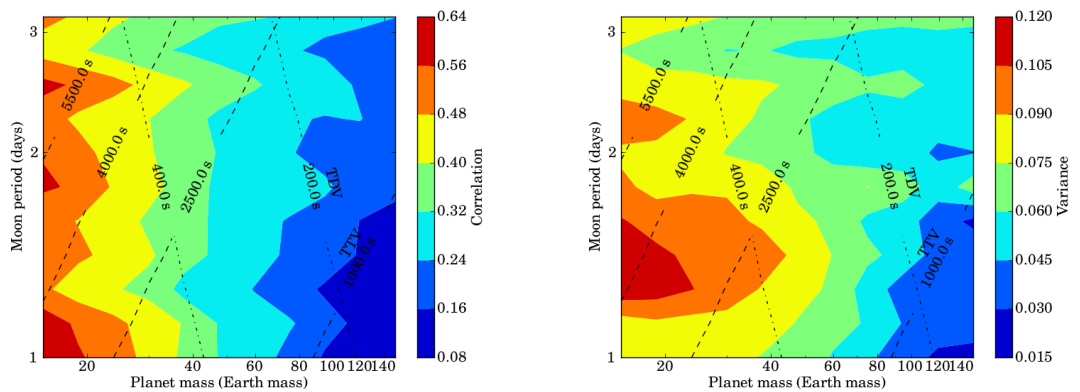


Figure 5.11: Correlation (left) and variance of correlation (right) contours between planet mass and moon period of the light curves with *Kepler* photometric noise. The contour is averaged over logarithmic planet separation and moon mass. The RMS amplitude of the TTV signal (dashed) and RMS amplitude of the TDV signal (dot-dashed) in units of seconds are presented.

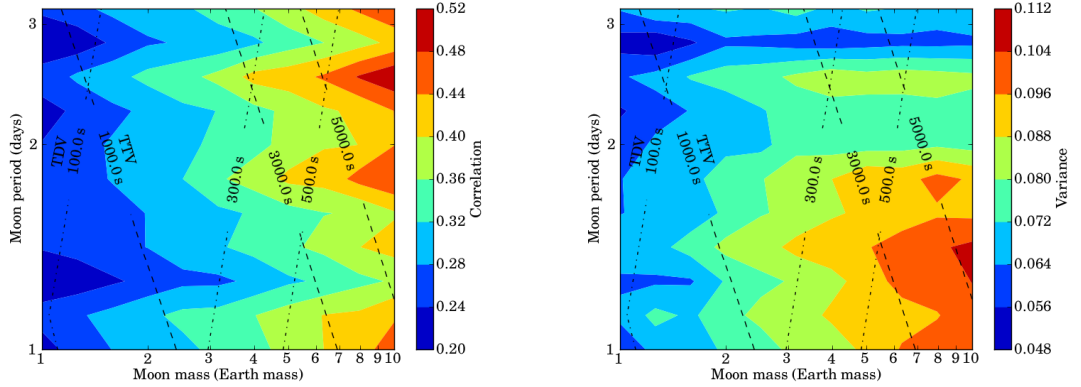


Figure 5.12: Correlation (left) and variance of correlation (right) contours between moon mass and moon period of the light curves with *Kepler* photometric noise. The contour is averaged over logarithmic planet mass and planet separation. The RMS amplitude of the TTV signal (dashed) and RMS amplitude of the TDV signal (dot-dashed) in units of seconds are presented.

on *Kepler* photometry show the same features. Therefore, the detectability of light curves with *Kepler* noise can represent the detectability of noiseless light curves. In order to investigate the detectability of the *Kepler* mission, only simulated *Kepler* data is analysed in this work.

In Figure 5.7, the plot between planet mass and moon mass with *Kepler* photometric noise shows that a high-mass moon hosted by a low-mass planet is likely to be detected. This result agrees with the moon period versus planet mass and moon mass plots (Figure 5.11 and Figure 5.12). However, in these two plots, the changes in moon period do not affect the correlation. In Figure 5.8, the projection plot between separation of planet and period of moon also does not show any significant meaning.

Figure 5.9 shows the detectability coefficient plot between mass and separation of the planet. Planets with high separation have higher detectability than close-in planets with the same mass. This result correlates with the result of moon mass versus planet separation plot (Figure 5.10) which shows that, in the systems with equal satellite mass, the outer planet hosts have larger correlation coefficients. These features may be produced by only a few transit events in high planet separation systems, because, at 0.6 AU separations, only three transit events are detected in

the simulation. Therefore, we now check the reliability of correlation.

The analysis of correlations is meaningful when the correlations are not dominated by noise. The variance of correlation is plotted in order to check the reliability of testing. From Figure 5.7 to Figure 5.12, the variance plots show that the systems with a small number of transit events (high planet's period systems) have higher variance. However, the value of variance is still low compared to the correlation coefficient.

From Figure 5.13 to Figure 5.18, we exclude zero-value correlations to investigate only possible moon-detected systems. The filtered contours present the same map structure as the contours which include zero-value. Thus, the structures of the contours are also not affected by the non-detected systems. In conclusion, the assumption that moons of outer planets should be easier to detect than moons of inner planets is confirmed by our simulations.

The theoretical lines of RMS amplitude of the TTV and TDV signals are shown to investigate the features of the contours. For the plot between the planet and their satellite masses (Figure 5.7), the high amplitude of TTV and TDV signals produced the high coefficient of detection with the same slope. Moreover, the features in Figure 5.9 and Figure 5.10 are also well-correlated with TDV RMS amplitude signals which can be explained by the relative weakness of TDV signals compared with TTV signals. In conclusion, the detectability of exomoons is dominated by the amplitude of TDV signals.

## 5.2 Analysing the correlation structure

The structures of correlation plots are explained by the magnitude of the TDV signal. However, in Figure 5.9 and Figure 5.10, gap structures at planets' semi-major axes 0.4 and 0.5 AU are shown. The variance plots show that there is no difference in variance between the area of background structures and gap structure. Therefore the features in Figure 5.9 and Figure 5.10 are real. To solve the problem of strange structures, the contours of all simulations are investigated separately.

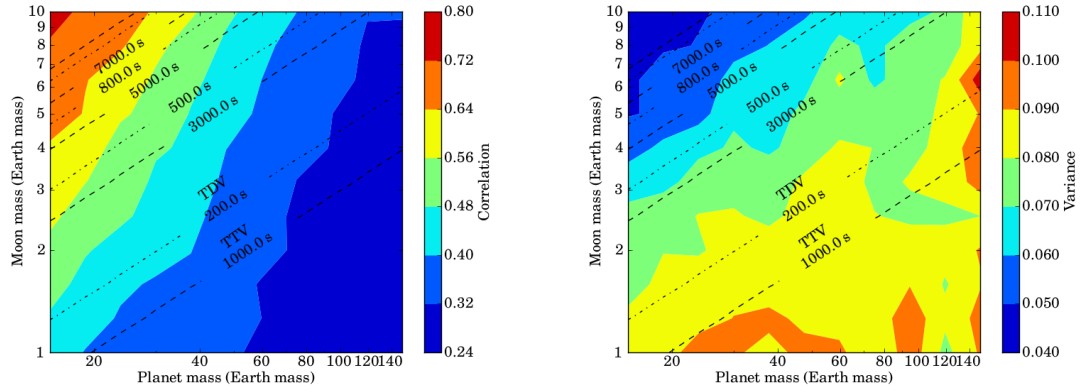


Figure 5.13: Correlation (left) and variance of correlation (right) contours between planet mass and moon mass of the light curves with *Kepler* photometric noise, excluding zero-value correlation. The contour is averaged over logarithmic planet separation and moon period. The RMS amplitude of the TTV signal (dashed) and RMS amplitude of the TDV signal (dot-dashed) in units of seconds are presented.

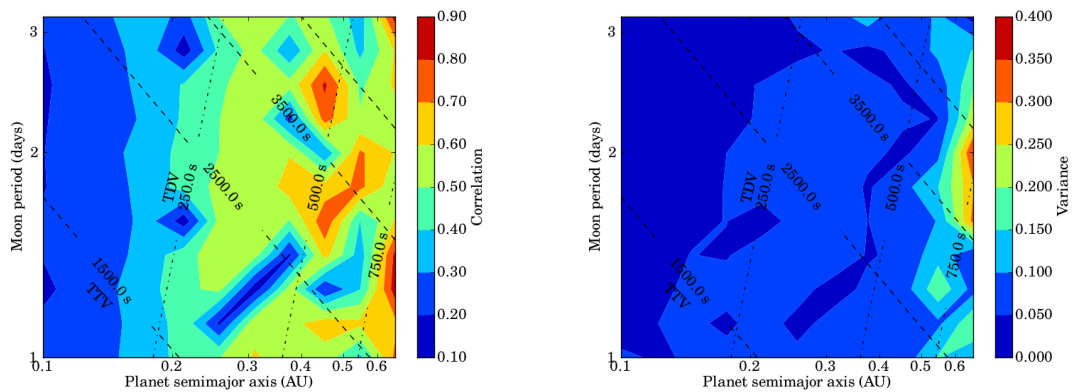


Figure 5.14: Correlation (left) and variance of correlation (right) contours between planet separation and moon period of the light curves with *Kepler* photometric noise, excluding zero-value correlation. The contour is averaged over logarithmic planet mass and moon mass. The RMS amplitude of the TTV signal (dashed) and RMS amplitude of the TDV signal (dot-dashed) in units of seconds are presented.

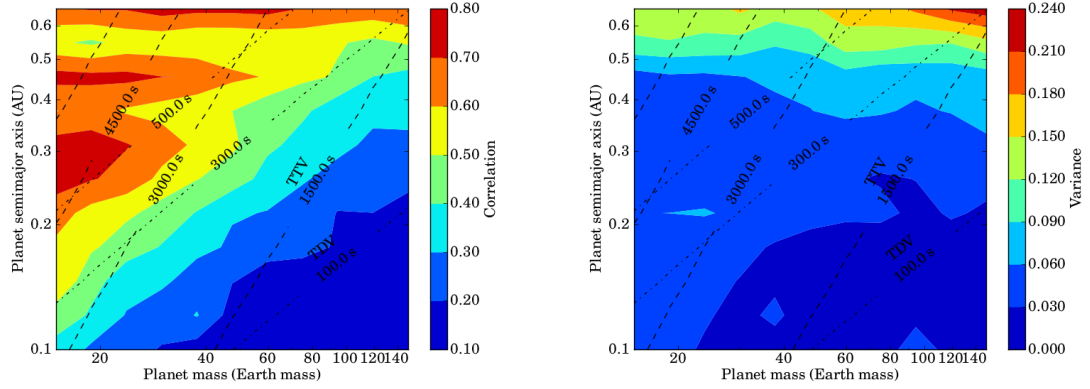


Figure 5.15: Correlation (left) and variance of correlation (right) contours between planet mass and planet separation of the light curves with *Kepler* photometric noise, excluding zero-value correlation. The contour is averaged over logarithmic moon mass and moon period. The RMS amplitude of the TTV signal (dashed) and RMS amplitude of the TDV signal (dot-dashed) in units of seconds are presented.

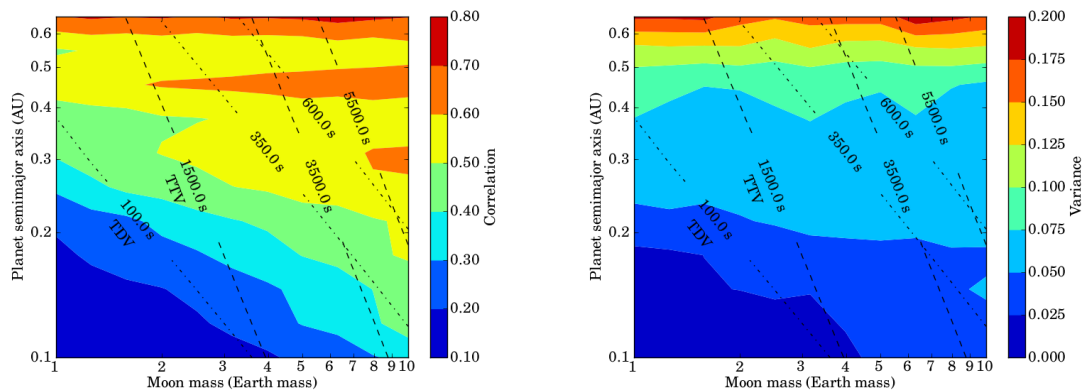


Figure 5.16: Correlation (left) and variance of correlation (right) contours between moon mass and planet separation of the light curves with *Kepler* photometric noise, excluding zero-value correlation. The contour is averaged over logarithmic planet mass and moon period. The RMS amplitude of the TTV signal (dashed) and RMS amplitude of the TDV signal (dot-dashed) in units of seconds are presented.

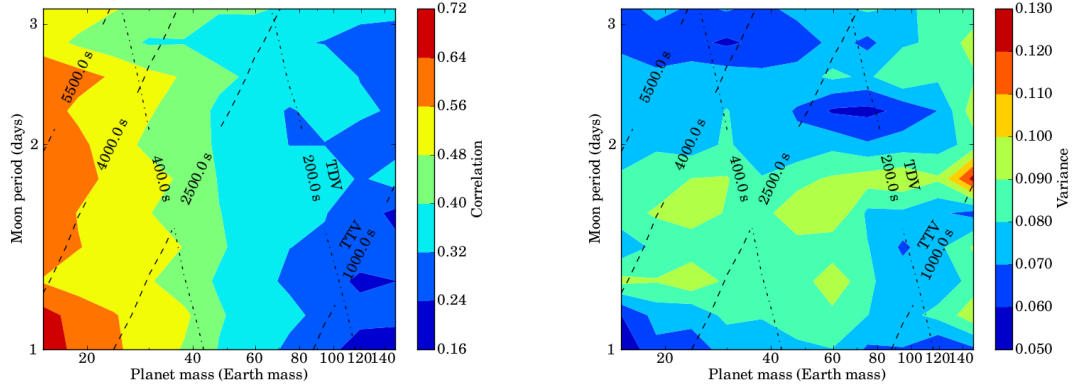


Figure 5.17: Correlation (left) and variance of correlation (right) contours between planet mass and moon period of the light curves with *Kepler* photometric noise, excluding zero-value correlation. The contour is averaged over logarithmic planet separation and moon mass. The RMS amplitude of the TTV signal (dashed) and RMS amplitude of the TDV signal (dot-dashed) in units of seconds are presented.

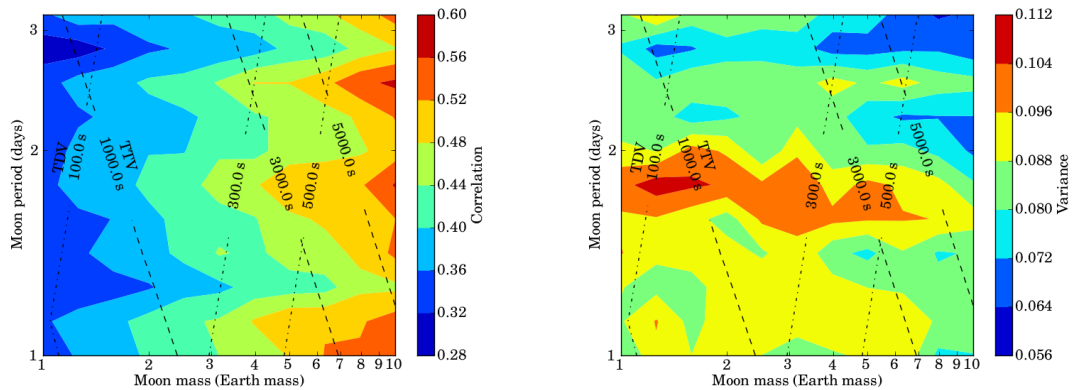


Figure 5.18: Correlation (left) and variance of correlation (right) contours between moon mass and moon period of the light curves with *Kepler* photometric noise, excluding zero-value correlation. The contour is averaged over logarithmic planet mass and planet separation. The RMS amplitude of the TTV signal (dashed) and RMS amplitude of the TDV signal (dot-dashed) in units of seconds are presented.

The correlation plots of planet separation versus planet mass and planet separation versus moon mass contours are shown in Figure 5.19 and Figure 5.21. Systems with high moon mass and low planet mass have a high value of correlation and the features in these contours correspond to the projected contour's features, including the gap structures.

In Figure 5.19 and Figure 5.21, the maps with similar a moon period show gap features at the same planet separation, but they shift with a different moon period. The ratios between moon period and planet which produce the gap are calculated (Table 5.2). The numbers in bold font indicate the ratios of planet period to moon period where the gaps are produced. They are nearly-integer value. This means the same moon orbital phase when transit events are detected. Therefore, the gap structures can be explained by the resonance between planet and moon period which produces the constant detected TTV and TDV signals. However, they also depend on the number of detected transit events. In short period systems which have a larger number of transits, the gap structures are more difficult to produce due to the larger range of detected planetary phases.

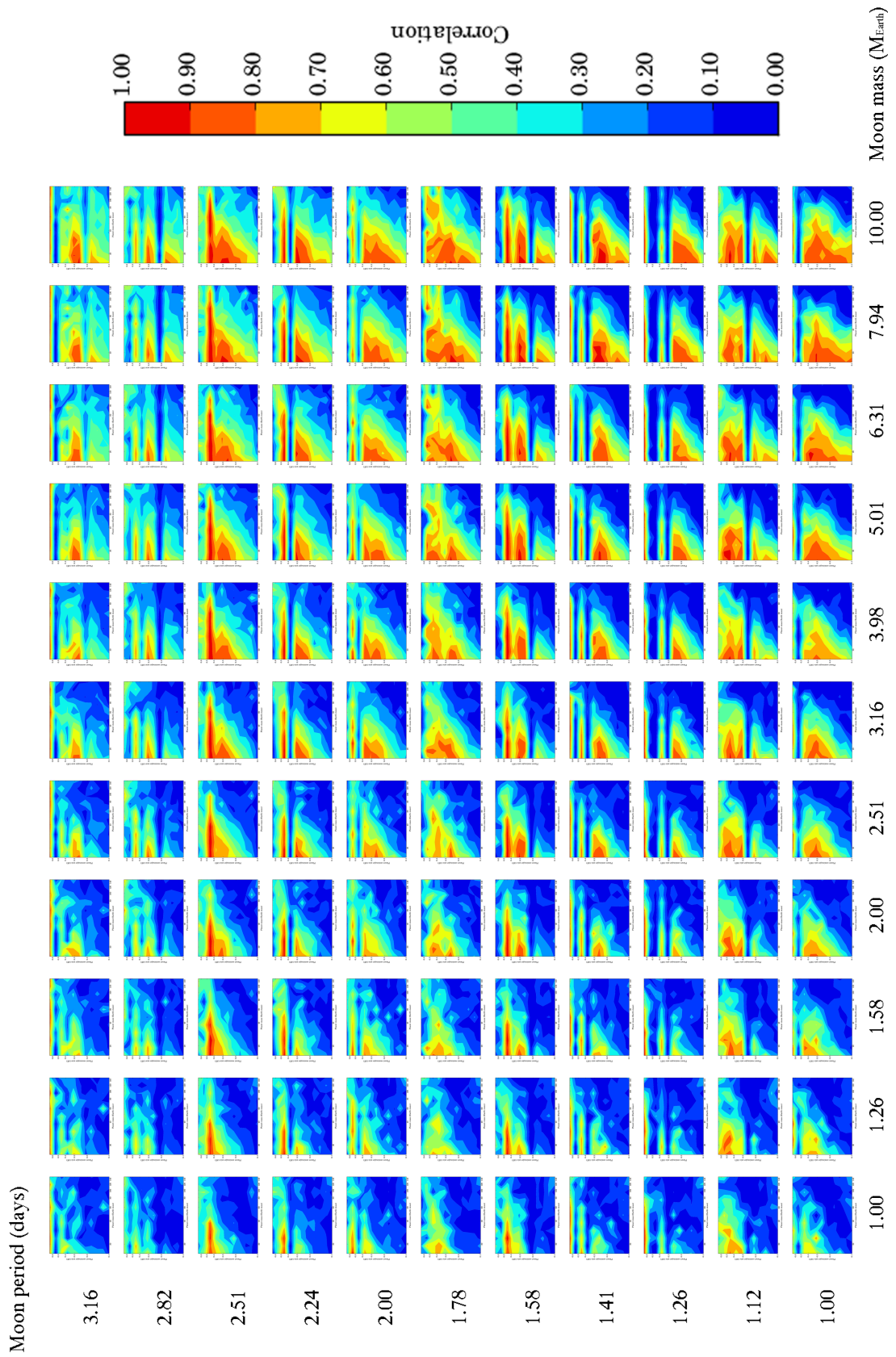


Figure 5.19: The correlation plots of planet separation versus planet mass contour of the light curves with *Kepler* photometric noise.

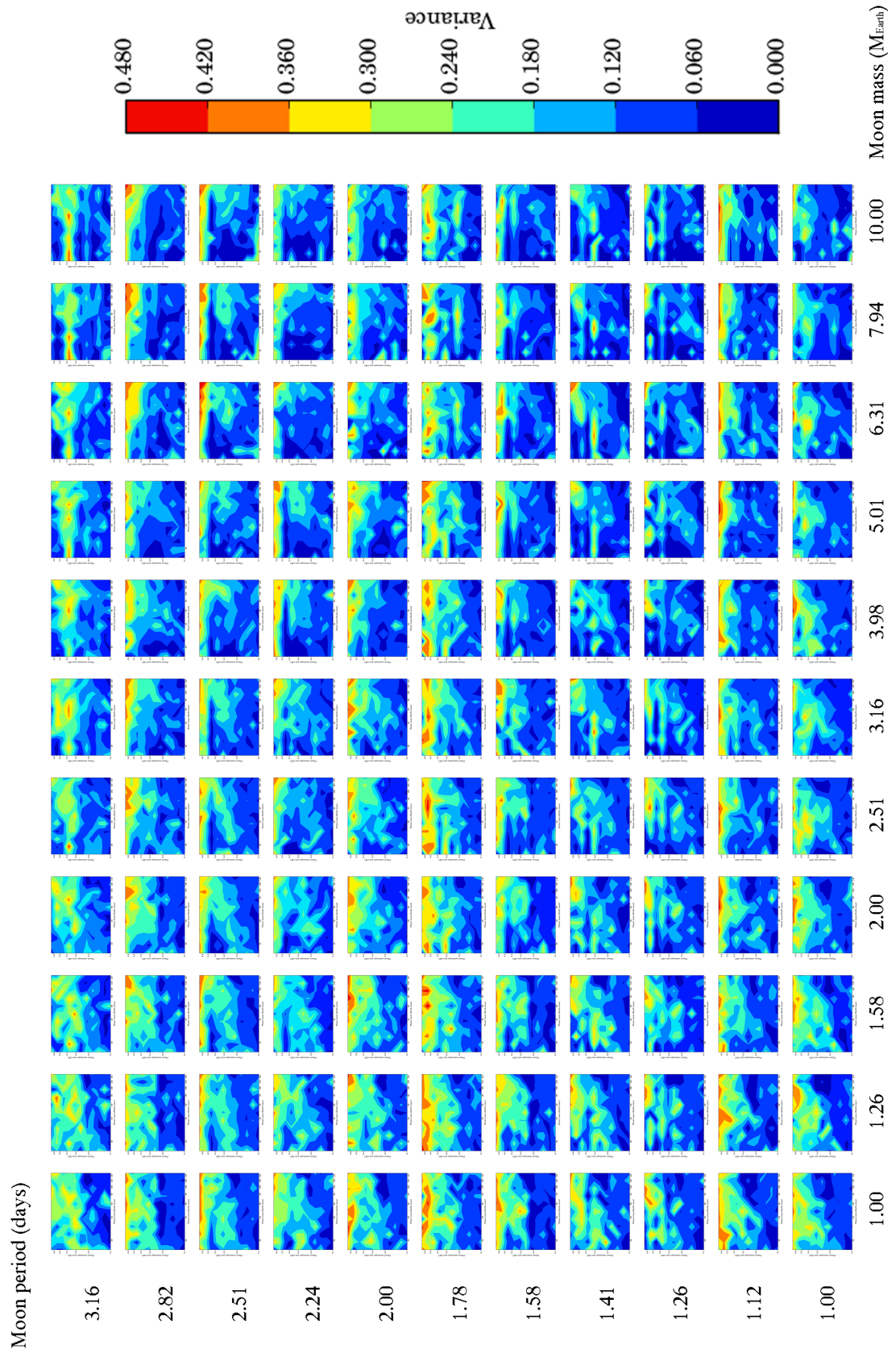


Figure 5.20: The variance of correlation plots of planet separation versus planet mass contour of the light curves with *Kepler* photometric noise.

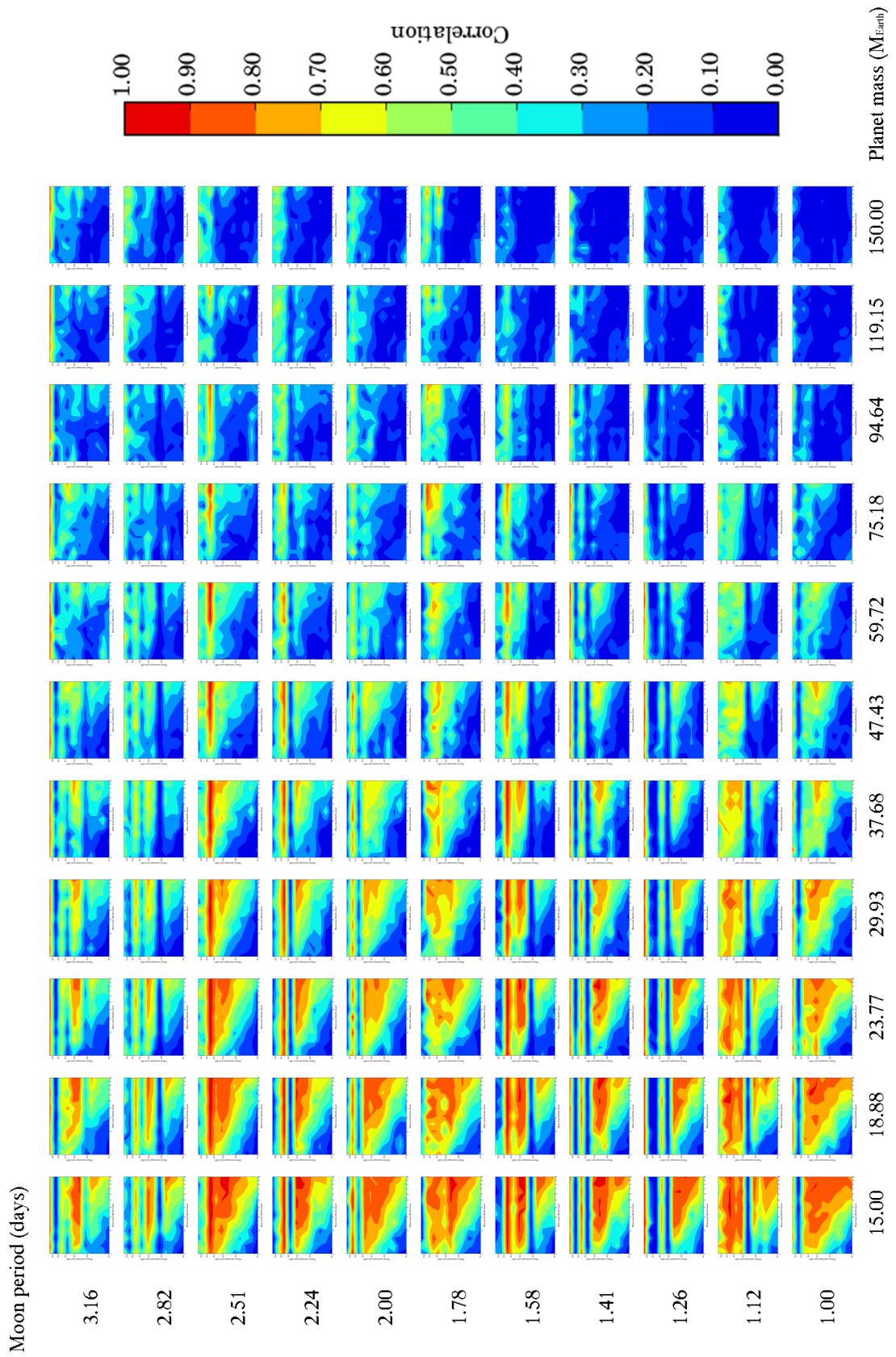


Figure 5.21: The correlation plots of planet separation versus moon mass contour of the light curves with *Kepler* photometric noise.

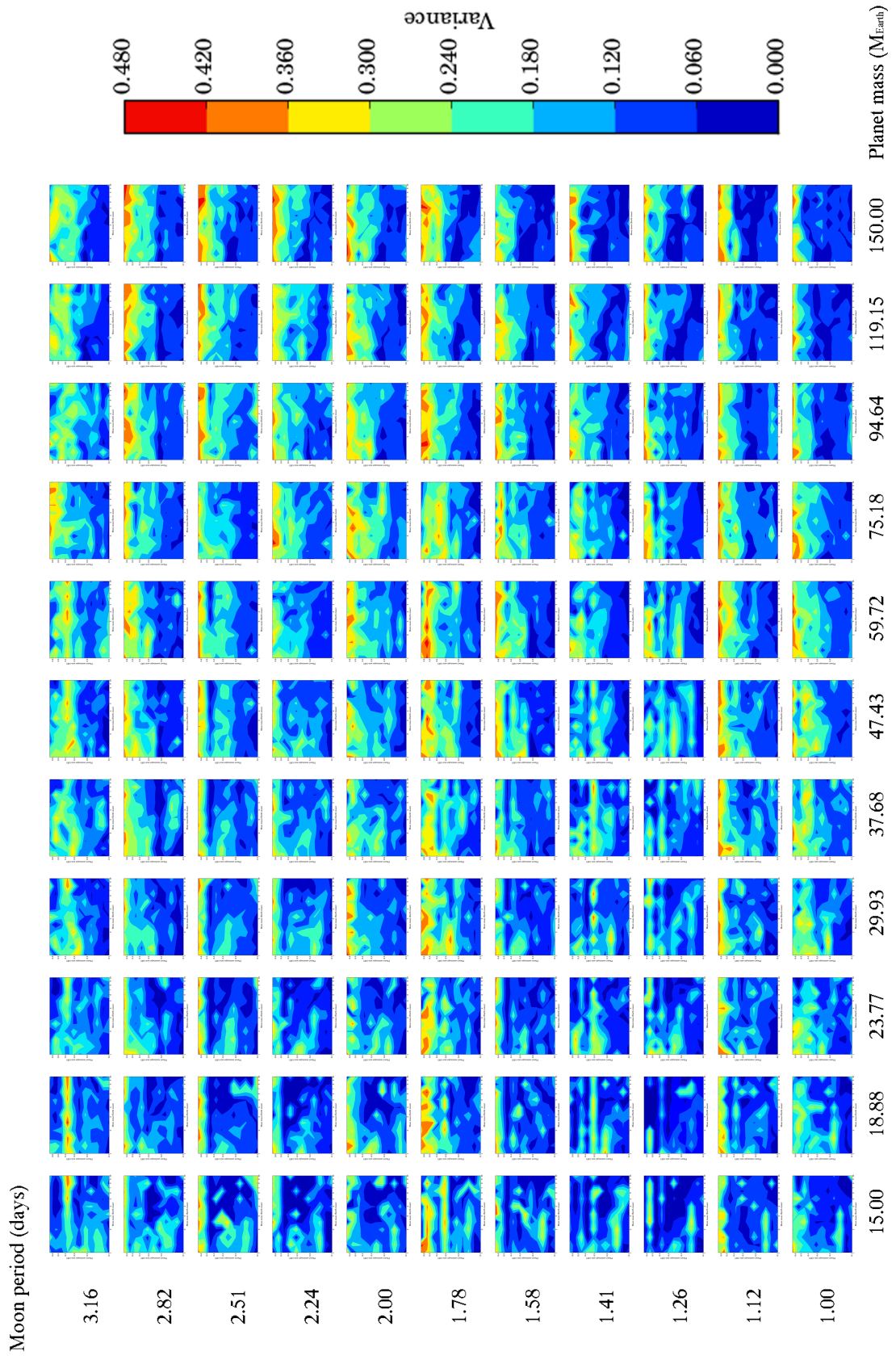


Figure 5.22: The variance of correlations plots of planet separation versus moon mass contour of the light curves with *Kepler* photometric noise.

Table 5.2: The ratio between moon periods and planet periods.

| $P_m = 1.00$  |               | $P_m = 1.12$  |               | $P_m = 1.26$  |               | $P_m = 1.41$  |               |
|---------------|---------------|---------------|---------------|---------------|---------------|---------------|---------------|
| $P_p$         | ratio         | $P_p$         | ratio         | $P_p$         | ratio         | $P_p$         | ratio         |
| 16.33         | 16.33         | 16.33         | 14.56         | 16.33         | 12.97         | 16.33         | 11.56         |
| 21.68         | 21.68         | 21.68         | 19.32         | 21.68         | 17.22         | 21.68         | 15.35         |
| 28.78         | 28.78         | 28.78         | 25.65         | 28.78         | 22.86         | 28.78         | 20.37         |
| 38.20         | 38.20         | 38.20         | 34.05         | 38.20         | 30.35         | 38.20         | 27.05         |
| 50.71         | 50.71         | 50.71         | 45.20         | 50.71         | 40.28         | 50.71         | 35.90         |
| 67.31         | 67.31         | <b>67.31</b>  | <b>59.99</b>  | 67.31         | 53.47         | 67.31         | 47.65         |
| 89.35         | 89.35         | 89.35         | 79.63         | <b>89.35</b>  | <b>70.97</b>  | 89.35         | 63.25         |
| 118.60        | 118.60        | 118.60        | 105.70        | 118.60        | 94.21         | <b>118.60</b> | <b>83.96</b>  |
| 157.43        | 157.43        | 157.43        | 140.31        | <b>157.43</b> | <b>125.05</b> | 157.43        | 111.45        |
| <b>208.97</b> | <b>208.97</b> | 208.97        | 186.25        | <b>208.97</b> | <b>165.99</b> | <b>208.97</b> | <b>147.94</b> |
| 277.39        | 277.39        | 277.39        | 247.23        | 277.39        | 220.34        | 277.39        | 196.38        |
| $P_m = 1.58$  |               | $P_m = 1.78$  |               | $P_m = 2.00$  |               | $P_m = 2.24$  |               |
| $P_p$         | ratio         | $P_p$         | ratio         | $P_p$         | ratio         | $P_p$         | ratio         |
| 16.33         | 10.31         | 16.33         | 9.19          | 16.33         | 8.19          | 16.33         | 7.30          |
| 21.68         | 13.68         | 21.68         | 12.19         | 21.68         | 10.87         | 21.68         | 9.68          |
| 28.78         | 18.16         | 28.78         | 16.18         | 28.78         | 14.42         | 28.78         | 12.86         |
| 38.20         | 24.10         | 38.20         | 21.48         | 38.20         | 19.15         | 38.20         | 17.06         |
| <b>50.71</b>  | <b>32.00</b>  | 50.71         | 28.52         | 50.71         | 25.42         | 50.71         | 22.65         |
| 67.31         | 42.47         | 67.31         | 37.85         | 67.31         | 33.74         | 67.31         | 30.07         |
| 89.35         | 56.38         | 89.35         | 50.25         | 89.35         | 44.78         | 89.35         | 39.91         |
| 118.60        | 74.83         | 118.60        | 66.70         | 118.60        | 59.44         | <b>118.60</b> | <b>52.98</b>  |
| 157.43        | 99.33         | 157.43        | 88.53         | <b>157.43</b> | <b>78.90</b>  | 157.43        | 70.32         |
| 208.97        | 131.85        | 208.97        | 117.52        | 208.97        | 104.74        | 208.97        | 93.35         |
| <b>277.39</b> | <b>175.02</b> | <b>277.39</b> | <b>155.99</b> | <b>277.39</b> | <b>139.03</b> | 277.39        | 123.91        |
| $P_m = 2.51$  |               | $P_m = 2.82$  |               | $P_m = 3.16$  |               |               |               |
| $P_p$         | ratio         | $P_p$         | ratio         | $P_p$         | ratio         |               |               |
| 16.33         | 6.50          | 16.33         | 5.80          | 16.33         | 5.17          |               |               |
| 21.68         | 8.63          | 21.68         | 7.69          | 21.68         | 6.86          |               |               |
| 28.78         | 11.46         | 28.78         | 10.21         | 28.78         | 9.10          |               |               |
| 38.20         | 15.21         | 38.20         | 13.55         | 38.20         | 12.08         |               |               |
| 50.71         | 20.19         | <b>50.71</b>  | <b>17.99</b>  | <b>50.71</b>  | <b>16.04</b>  |               |               |
| 67.31         | 26.80         | 67.31         | 23.88         | 67.31         | 21.29         |               |               |
| 89.35         | 35.57         | 89.35         | 31.70         | 89.35         | 28.25         |               |               |
| 118.60        | 47.22         | <b>118.60</b> | <b>42.08</b>  | 118.60        | 37.51         |               |               |
| 157.43        | 62.67         | 157.43        | 55.86         | 157.43        | 49.78         |               |               |
| 208.97        | 83.19         | 208.97        | 74.15         | <b>208.97</b> | <b>66.08</b>  |               |               |
| 277.39        | 110.43        | 277.39        | 98.42         | 277.39        | 87.72         |               |               |

### 5.3 Improving the detectability with long-term observation

In section 5.1 and Section 5.2, the 1,000 days simulations with 50,000 data points (every 28.8 minutes) are analysed. In theory a longer time baseline should produce a better detectability coefficient, because of more transiting events. In 2012, *Kepler*

has been approved for extension through to 2016. Therefore, 5-years photometric data from *Kepler* targets should be obtained. The 1,600 days simulation with 80,000 data points (every 28.8 minutes) is chosen to produce a sample of long-term observation. The input parameters of this simulation are listed in Table 5.3.

Table 5.3: Input parameters for the long-term observation simulation.

| <b>Star parameters</b>                       |               |
|--|---------------|
| Star mass ( $M_{\odot}$ )                    | 0.5           |
| Star radius ( $R_{\odot}$ )                  | 0.55          |
| Star apparent magnitude ( $K_p$ )            | 12.5          |
| Quadratic limb-darkening coefficient 1       | 0.4042        |
| Quadratic limb-darkening coefficient 2       | 0.3268        |
| <b>Planet parameters</b>                     |               |
| Planet mass ( $M_{\oplus}$ )                 | 18.9          |
| Planet radius ( $R_{\oplus}$ )               | 10.973        |
| Planet separation (AU)                       | 0.10-0.66     |
| Planet eccentricity                          | 0.0           |
| Planet inclination (degrees)                 | 90.0          |
| Planet argument of periapsis (degrees)       | 0.0           |
| Planet longitude of ascending node (degrees) | 0.0           |
| <b>Moon parameters</b>                       |               |
| Moon mass ( $M_{\oplus}$ )                   | 1.0-10.0      |
| Moon radius ( $R_{\oplus}$ )                 | Equation 4.61 |
| Moon period (days)                           | 2.51          |
| Moon eccentricity                            | 0.0           |
| Moon inclination (degrees)                   | 90.0          |
| Moon argument of periapsis (degrees)         | 0.0           |
| Moon longitude of ascending node (degrees)   | 0.0           |

In Figure 5.23 and Figure 5.24, the correlation and their variance contours from 5-years of observation are shown. The contours of two simulations show the same structures, but the long-term simulation has a better detectability. From this result, the number of detected exomoons should increase with length of observation. The extension to the *Kepler* mission, possible additional space-based telescope missions and long-term follow-up ground base surveys should allow the habitable exomoons to be detected or their abundance constrained.

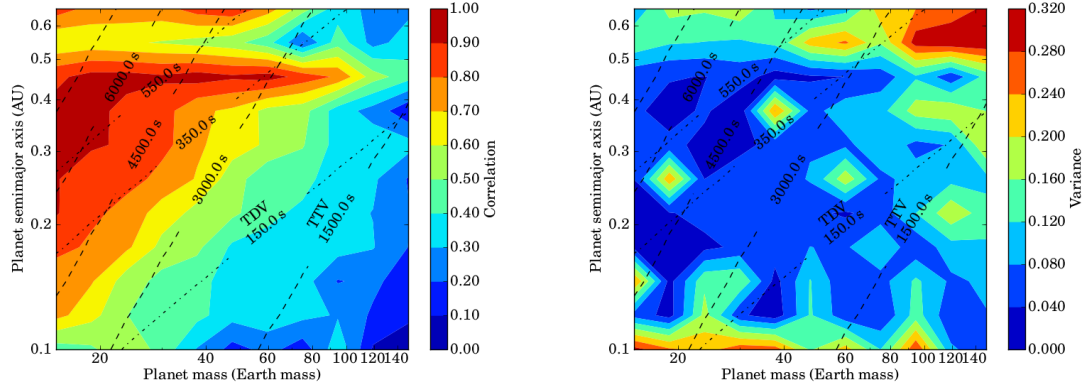


Figure 5.23: Correlation (left) and variance of correlation (right) contours between planet mass and planet separation of the long-term simulation light curves with *Kepler* photometric noise. The contour is averaged over logarithmic moon mass and moon period. The RMS amplitude of the TTV signal (dashed) and RMS amplitude of the TDV signal (dot-dashed) in units of seconds are presented.

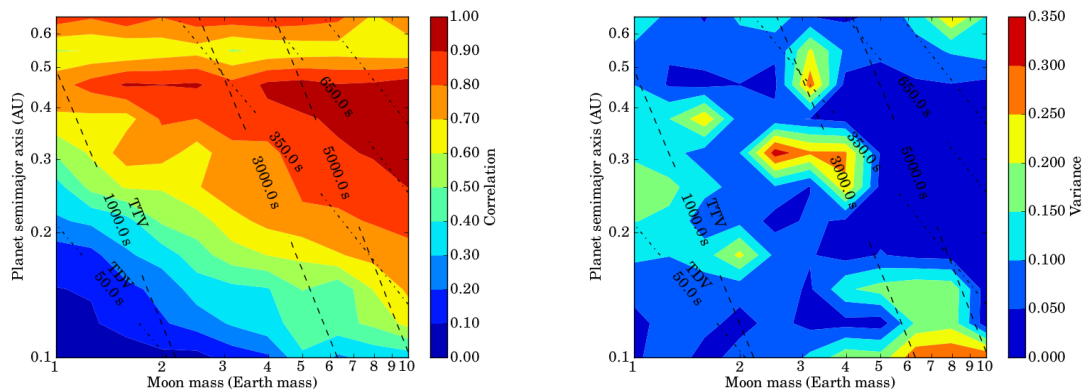


Figure 5.24: Correlation (left) and variance of correlation (right) contours between moon mass and planet separation of the long-term simulation light curves with *Kepler* photometric noise. The contour is averaged over logarithmic planet mass and moon period. The RMS amplitude of the TTV signal (dashed) and RMS amplitude of the TDV signal (dot-dashed) in units of seconds are presented.

# Chapter 6

## Conclusion and further work

### 6.1 Improvement to simulation

The simulation has been shown to successfully simulate transiting light curves with exomoons. 146,410 systems are simulated and analysed in this work. The number of simulation events is still low in order to investigate the relation between TTV and TDV RMS signals with correlation and the inter-relationship between planet and moon period. Increasing the number of light curves would increase the statistical sample.

By making the simulations more realistic, the results can be more confidently compared to real data. In this work, the planets and moons orbit around their host with circular orbit and with 90-degrees inclination. Elliptical exoplanet and exomoon orbits could make the simulations more realistic. Varying the inclination should produce the TDV-TIP signal which was not included in this work.

For a long-term simulation, the number of transit events should increase which means the statistical sample of data would increase and also planets with longer period could be analysed. 3-years simulations give enough samples to investigate planets in the HZ of an M-Dwarf. In solar-type host stars (G-type), the simulation should last more than 5 years in order to produce sufficient samples to analyse the HZ planets.

Moreover, this code can produce the light curves with *Euclid* photometric noise

(both NISP and VIS instrument). In October 2011, the *Euclid* space mission was selected by ESA to launch in 2019. An exoplanet survey is one of the primary candidates of additional surveys. Although, the additional surveys should focus on the exoplanet microlensing, the transiting exoplanet should also be detected by *Euclid*. Therefore, investigating the detectability of habitable exomoons with *Euclid* is of interest.

## 6.2 Conclusion

Since the first discovery of exoplanets in 1992, the studies of exoplanets have fascinated by astronomers. A lot of missions, both ground-based and space-based missions, have been launched and will be launched in the near future. To date, more than 750 exoplanets have been confirmed. None of them have detected moons orbiting around them. From Kipping et al. (2009), there is a potential to detect exomoons with space missions, such as *Kepler*.

The light curves of a transiting exoplanet with an exomoon were successfully implemented for the purpose of determining detectability of exomoons. The *Kepler* photometric noise was added to the light curve in order to simulate the data from *Kepler*. Measuring the detectability was done by phase-correlation between TTV and TDV signals. TTV and TDV always exhibit a 90-degree phase shift, therefore, the  $TTV^2$  signal is linear with the  $TDV^2$  signal. The Pearson product-moment correlation coefficient was used to determine the detectability of signals.

3-year *Kepler* light curves of 146,410 systems with various configurations were simulated. For each extrasolar planet system, the giant planets and their rocky satellites were placed in the habitable zone of  $0.5 M_{\odot}$  dwarf stars. Their masses and periods were selected logarithmically. For simplicity, edge-on circular orbits with 10 random initial orbital phases were used. From analysing simulated light curves, the detectability of exomoons increase significantly with the moon's mass and decrease with increasing mass of planets. Moreover, the correlation coefficient of systems with the same planet mass or moon mass decreases with the planet semi-major-axis

which can be explained by the correlation between the detectability and intensity of TDV signals which are weaker than TTV signals. Exomoon periods in resonance with planetary orbital period may prevent detection due to the constant observed planet orbital phase. For long-term observations of transit time, the detectability clearly improves.

In conclusion, the detectability of habitable exomoons is dominated by the amplitude of the TDV signal and the ratio of planet period to moon period. There is a possibility of detecting the first exomoon using the *Kepler* telescope. Exomoons in the habitable zone of an M-Dwarf system can be detected by 3-years *Kepler's* data and the number of detected extrasolar moons should increase with the number of detected transiting exoplanets in the near future.

# Bibliography

Agol E., Steffen J., Sari R., Clarkson W., 2005, MNRAS, 359, 567

Baines E. K., van Belle G. T., ten Brummelaar T. A., et al., 2007, ApJ, 661, L195

Bakos G., Afonso C., Henning T., et al., 2009, in IAU Symposium, vol. 253 of IAU Symposium, 354–357

Bakos G., Noyes R. W., Kovács G., Stanek K. Z., Sasselov D. D., Domsa I., 2004, PASP, 116, 266

Bakos G. Á., Hartman J. D., Torres G., et al., 2011, in European Physical Journal Web of Conferences, vol. 11 of European Physical Journal Web of Conferences, 1002

Bakos G. Á., Noyes R. W., Kovács G., et al., 2007, ApJ, 656, 552

Ballard S., Fabrycky D., Fressin F., et al., 2011, ApJ, 743, 200

Barnes J. W., O'Brien D. P., 2002, ApJ, 575, 1087

Batalha N. M., Borucki W. J., Koch D. G., et al., 2010, ApJ, 713, L109

Batalha N. M., Rowe J. F., Bryson S. T., et al., 2012, ArXiv e-prints, 1202.5852

Bean J. L., Seifahrt A., Hartman H., et al., 2010a, ApJ, 713, 410

Bean J. L., Seifahrt A., Hartman H., et al., 2010b, ApJ, 711, L19

Benedict G. F., McArthur B. E., Bean J. L., et al., 2010, AJ, 139, 1844

Benedict G. F., McArthur B. E., Forveille T., et al., 2002, ApJ, 581, L115

- Bond I. A., Rattenbury N. J., Skuljan J., et al., 2002, *MNRAS*, 333, 71
- Bond I. A., Udalski A., Jaroszyński M., et al., 2004, *ApJ*, 606, L155
- Bonfils X., Delfosse X., Udry S., Santos N. C., Forveille T., Ségransan D., 2005, *A&A*, 442, 635
- Borucki W. J., Koch D., Basri G., et al., 2005, in *A Decade of Extrasolar Planets around Normal Stars*, Cambridge Univ. Press, Cambridge, 36
- Borucki W. J., Koch D. G., Basri G., et al., 2011a, *ApJ*, 728, 117
- Borucki W. J., Koch D. G., Basri G., et al., 2011b, *ApJ*, 736, 19
- Borucki W. J., Koch D. G., Batalha N., et al., 2012, *ApJ*, 745, 120
- Borucki W. J., Summers A. L., 1984, *Icarus*, 58, 121
- Brown T. M., Latham D. W., Everett M. E., Esquerdo G. A., 2011, *AJ*, 142, 112
- Butters O. W., West R. G., Anderson D. R., et al., 2010, *A&A*, 520, L10
- Caldwell D. A., Kolodziejczak J. J., Van Cleve J. E., et al., 2010a, *ApJ*, 713, L92
- Caldwell D. A., van Cleve J. E., Jenkins J. M., et al., 2010b, in *Society of Photo-Optical Instrumentation Engineers (SPIE) Conference Series*, vol. 7731 of *Society of Photo-Optical Instrumentation Engineers (SPIE) Conference Series*
- Canup R. M., Ward W. R., 2006, *Nature*, 441, 834
- Catala C., Arentoft T., Fridlund M., et al., 2011, *PLATO Definition Study Report*, ESA
- Chabrier G., 2003, *PASP*, 115, 763
- Charbonneau D., Berta Z. K., Irwin J., et al., 2009, *Nature*, 462, 891
- Charbonneau D., Brown T. M., Burrows A., Laughlin G., 2007, *Protostars and Planets V*, 701–716

- Charbonneau D., Brown T. M., Latham D. W., Mayor M., 2000, *ApJ*, 529, L45
- Chauvin G., Lagrange A.-M., Dumas C., et al., 2004, *A&A*, 425, L29
- Chauvin G., Lagrange A.-M., Dumas C., et al., 2005, *A&A*, 438, L25
- Chyba C. F., 1997, *Nature*, 385, 201
- Claret A., Bloemen S., 2011, *A&A*, 529, A75
- Díaz R. F., Almenara J. M., Bonomo A., et al., 2011, in *EPSC-DPS Joint Meeting 2011*, 1243
- Domingos R. C., Winter O. C., Yokoyama T., 2006, *MNRAS*, 373, 1227
- Fewell M., 2006, *Area of Common Overlap of Three Circles*, Tech. Rep., DSTO-TN-0722 (Online). Available at: <http://hdl.handle.net/1947/4551>
- Fortney J. J., Marley M. S., Barnes J. W., 2007a, *ApJ*, 668, 1267
- Fortney J. J., Marley M. S., Barnes J. W., 2007b, *ApJ*, 659, 1661
- Forveille T., Bonfils X., Delfosse X., et al., 2011, *ArXiv e-prints*, 1109.2505
- Gaidos E., Haghighipour N., Agol E., Latham D., Raymond S., Rayner J., 2007, *Science*, 318, 210
- Gilliland R. L., Jenkins J. M., Borucki W. J., et al., 2010, *ApJ*, 713, L160
- Gonzalez G., Brownlee D., Ward P., 2001, *Icarus*, 152, 185
- Gould A., Udalski A., An D., et al., 2006, *ApJ*, 644, L37
- Green J., Schechter P., Baltay C., et al., 2011, *ArXiv e-prints*, 1108.1374
- Han C., Han W., 2002, *ApJ*, 580, 490
- Hébrard G., Evans T. M., Alonso R., et al., 2011, *A&A*, 533, A130
- Heintz W. D., 1978, *ApJ*, 220, 931

- Henry G. W., Marcy G. W., Butler R. P., Vogt S. S., 2000, *ApJ*, 529, L41
- Henry T. J., Kirkpatrick J. D., Simons D. A., 1994, *AJ*, 108, 1437
- Holman M. J., Murray N. W., 2005, *Science*, 307, 1288
- Holmberg J., Nordström B., Andersen J., 2007, *A&A*, 475, 519
- Holmberg J., Nordström B., Andersen J., 2009, *A&A*, 501, 941
- Howard A. W., Marcy G. W., Bryson S. T., et al., 2012, *ApJS*, 201, 15
- Howard A. W., Marcy G. W., Johnson J. A., et al., 2010, *Science*, 330, 653
- Huang S. S., 1959, *American Scientist*, 47, 397
- Johnson J. A., Apps K., 2009, *ApJ*, 699, 933
- Joshi M. M., Haberle R. M., Reynolds R. T., 1997, *Icarus*, 129, 450
- Kasting J. F., Whitmire D. P., Reynolds R. T., 1993, *Icarus*, 101, 108
- Kennedy G. M., Kenyon S. J., 2008, *ApJ*, 682, 1264
- Kipping D. M., 2009a, *MNRAS*, 392, 181
- Kipping D. M., 2009b, *MNRAS*, 396, 1797
- Kipping D. M., 2011, *MNRAS*, 416, 689
- Kipping D. M., Fossey S. J., Campanella G., 2009, *MNRAS*, 400, 398
- Laskar J., Joutel F., Robutel P., 1993, *Nature*, 361, 615
- Laureijs R., Amiaux J., Arduini S., et al., 2011, *Euclid Definition Study Report*,  
ESA
- Lecar M., Podolak M., Sasselov D., Chiang E., 2006, *ApJ*, 640, 1115
- Léger A., Rouan D., Schneider J., et al., 2009, *A&A*, 506, 287
- Lewis K. M., Sackett P. D., Mardling R. A., 2008, *ApJ*, 685, L153

- Lin D. N. C., 2008, *Scientific American*, 298, 50
- Lineweaver C. H., Fenner Y., Gibson B. K., 2004, *Science*, 303, 59
- Mandel K., Agol E., 2002, *ApJ*, 580, L171
- Mann A. W., Gaidos E., Lépine S., Hilton E. J., 2012, *ApJ*, 753, 90
- Mao S., Paczynski B., 1991, *ApJ*, 374, L37
- Marois C., Macintosh B., Barman T., et al., 2008, *Science*, 322, 1348
- Martoli E., McArthur B. E., Benedict G. F., Bean J. L., Harrison T. E., Armstrong A., 2010, *ApJ*, 708, 625
- Masciadri E., Raga A., 2004, *ApJ*, 611, L137
- Mayor M., Bonfils X., Forveille T., et al., 2009, *A&A*, 507, 487
- Mayor M., Marmier M., Lovis C., et al., 2011, *ArXiv e-prints*, 1109.2497
- Mayor M., Queloz D., 1995, *Nature*, 378, 355
- McArthur B. E., Endl M., Cochran W. D., et al., 2004, *ApJ*, 614, L81
- McDonald I., et al, 2012, (In perp.)
- Murray C. D., Dermott S. F., 1999, *Solar system dynamics*, New York: Cambridge University. Press
- Nielsen E. L., Close L. M., Biller B. A., Masciadri E., Lenzen R., 2008, *ApJ*, 674, 466
- Penny M. T., Kerins E., Rattenbury N., et al., 2012, *ArXiv e-prints*, 1206.5296
- Pepe F., Lovis C., Ségransan D., et al., 2011, *A&A*, 534, A58
- Pollacco D. L., Skillen I., Collier Cameron A., et al., 2006, *PASP*, 118, 1407
- Porter S. B., Grundy W. M., 2011, *ApJ*, 736, L14

- Pravdo S. H., Shaklan S. B., 2009, *ApJ*, 700, 623
- Reid I. N., Cruz K. L., Allen P., et al., 2004, *AJ*, 128, 463
- Reuyl D., Holmberg E., 1943, *ApJ*, 97, 41
- Santos N. C., Bouchy F., Mayor M., et al., 2004, *A&A*, 426, L19
- Sartoretti P., Schneider J., 1999, *A&AS*, 134, 553
- Scharf C. A., 2007, *ApJ*, 661, 1218
- Schlaufman K. C., Laughlin G., 2010, *A&A*, 519, A105
- Schlaufman K. C., Laughlin G., 2011, *ApJ*, 738, 177
- Schulze-Makuch D., Méndez A., Fairén A. G., et al., 2011, *Astrobiology*, 11, 1041
- Seager S., Mallén-Ornelas G., 2003, *ApJ*, 585, 1038
- Selsis F., Kasting J. F., Levrard B., Paillet J., Ribas I., Delfosse X., 2007, *A&A*, 476, 1373
- Simon A., Szatmáry K., Szabó G. M., 2007, *A&A*, 470, 727
- Strand K. A., 1943, *PASP*, 55, 29
- Tinetti G., Beaulieu J. P., Henning T., et al., 2011, *EChO Science Requirements Document*, ESA
- Tingley B., Sackett P. D., 2005, *ApJ*, 627, 1011
- Udalski A., Szymanski M. K., Soszynski I., Poleski R., 2008, *Acta Astron.*, 58, 69
- Udry S., Bonfils X., Delfosse X., et al., 2007, *A&A*, 469, L43
- Udry S., Santos N. C., 2007, *ARA&A*, 45, 397
- Unwin S. C., Shao M., Tanner A. M., et al., 2008, *PASP*, 120, 38
- Van Cleve J. E., Caldwell D. A., 2009, *Kepler Instrument Handbook*, KSCI 19033-001, NASA Ames Research Center

Vogt S. S., Butler R. P., Rivera E. J., Haghighipour N., Henry G. W., Williamson M. H., 2010, *ApJ*, 723, 954

von Bloh W., Bounama C., Cuntz M., Franck S., 2007, *A&A*, 476, 1365

Williams D. M., Kasting J. F., Wade R. A., 1997, *Nature*, 385, 234

Winn J. N., 2010, *ArXiv e-prints*, 1001.2010

Wolszczan A., Frail D. A., 1992, *Nature*, 355, 145

Wright J. T., Fakhouri O., Marcy G. W., et al., 2011, *PASP*, 123, 412

Yee J. C., Gaudi B. S., 2008, *ApJ*, 688, 616

# Appendix A

## List of parameters

Table A.1 provides a list of the various key parameters used throughout this dissertation.

Table A.1: List of important parameters used in this dissertation.

| <b>Parameter</b> | <b>Definition</b>                                       |
|------------------|---|
| $c$              | Speed of light in the vacuum                            |
| $G$              | Gravitational constant                                  |
| $\sigma$         | Stefan-Boltzmann constant                               |
| $M_*$            | Mass of star  |
| $M_p$            | Mass of planet  |
| $M_m$            | Mass of moon  |
| $R_*$            | Radius of star  |
| $R_p$            | Radius of planet  |
| $R_m$            | Radius of moon  |
| $a_p$            | Semi-major axis of planet                               |
| $a_m$            | Semi-major axis of moon                                 |
| $a_{pb}$         | Semi-major axis of planet around planet-moon barycentre |
| $P_p$            | Period of planet  |
| $P_m$            | Period of moon  |
| $i_p$            | Inclination of planet                                   |
| $i_m$            | Inclination of moon                                     |

*Continued on next page*

*Continued from previous page*

| Parameter  | Definition                                |
|------------|---|
| $\Omega_p$ | Longitude of ascending node of planet     |
| $\Omega_m$ | Longitude of ascending node of moon       |
| $\omega_p$ | Argument of periapsis of planet           |
| $\omega_m$ | Argument of periapsis of moon             |
| $\varpi_p$ | Positions of pericentre of planet         |
| $\varpi_m$ | Positions of pericentre of moon           |
| $T_*$      | Effective temperature of star             |
| $T_p$      | Effective temperature of planet           |
| $L_*$      | Luminosity of star                        |
| $L_\odot$  | Luminosity of the Sun                     |
| $e_p$      | Orbital eccentricity of planet            |
| $e_m$      | Orbital eccentricity of moon              |
| $f_{tp}$   | True anomaly of planet                    |
| $f_{tm}$   | True anomaly of moon                      |
| $f_{mp}$   | Mean anomaly of planet                    |
| $f_{mm}$   | Mean anomaly of moon                      |
| $t - t_p$  | Time elapsed since the planet's periapsis |
| $t - t_m$  | Time elapsed since the moon's periapsis   |
| $x_p$      | X-component of position of planet         |
| $x_m$      | X-component of position of moon           |
| $y_p$      | Y-component of position of planet         |
| $y_m$      | Y-component of position of moon           |
| $z_p$      | Z-component of position of planet         |
| $z_m$      | Z-component of position of moon           |
| $S_{sp}$   | Sky-projected star-planet separation      |
| $S_{sm}$   | Sky-projected star-moon separation        |
| $S_{pm}$   | Sky-projected planet-moon separation      |
| $P_{tran}$ | Transit probability                       |

*Continued on next page*

*Continued from previous page*

| Parameter        | Definition   |
|------------------|--|
| $\delta$         | Transit depth                                      |
| $\bar{\tau}$     | Transit duration                                   |
| $\tau_{ing}$     | Ingress duration                                   |
| $\tau_{egr}$     | Egress duration                                    |
| $t_{ing}$        | Ingress time                                       |
| $t_{egr}$        | Egress time  |
| $t_0$            | Time of minimum light                              |
| $n$              | Epoch  |
| $b$              | Impact parameter                                   |
| $T_I$            | First contact time                                 |
| $T_{II}$         | Second contact time                                |
| $T_{III}$        | Third contact time                                 |
| $T_{IV}$         | Fourth contact time                                |
| $TTV$            | TTV signal   |
| $TDV$            | TDV signal   |
| $\Delta t_{TTV}$ | Peak-to-peak amplitude of TTV signal               |
| $\Delta t_{TDV}$ | Peak-to-peak amplitude of TDV signal               |
| $\delta_{TTV}$   | RMS amplitude of the TTV signal                    |
| $\delta_{TDV}$   | RMS amplitude of the TDV signal                    |
| $v_{B\perp}$     | Projected velocity of the planet-moon barycentre   |
| $r_p$            | Distance between star and planet-moon barycentre   |
| $r_{sp}$         | Distance between star and planet                   |
| $r_{sm}$         | Distance between star and moon                     |
| $r_{bp}$         | Distance between planet-moon barycentre and planet |
| $r_{bm}$         | Distance between planet-moon barycentre and moon   |
| $I$              | Intensity of star                                  |
| $c_n$            | Non-linear limb darkening coefficients             |
| $r$              | Radial distance from the centre of the star        |

*Continued on next page*

*Continued from previous page*

| Parameter      | Definition  |
|----------------|---|
| $d$            | Center-to-center distance between the star and the planet   |
| $z$            | Ratio of star-planet distance to the stellar radius         |
| $p$            | Ratio of the planet's radius to the stellar radius          |
| $F_{total}$    | Flux of star  |
| $F_{transit}$  | Flux of planet-moon transit                                 |
| $F_{planet}$   | Flux of planetary transit                                   |
| $F_{area}$     | Flux of transit area  |
| $A_{p,t}$      | Transit area of planet                                      |
| $A_{m,t}$      | Transit area of moon  |
| $A_p$          | Ratio of transit area of planet                             |
| $A_m$          | Ratio of transit area of moon                               |
| $\alpha$       | The area of intersection between any two circles            |
| $\Gamma_{ph}$  | Photon collection rate of <i>Kepler</i>                     |
| $m$            | Apparent magnitude of star                                  |
| $R_H$          | Hill radius   |
| $r_{hab}$      | Distance where planets receive the same energy as the Earth |
| $r_{in}$       | Inner boundary of the HZ                                    |
| $r_{out}$      | Outer boundary of the HZ                                    |
| $r_{in\odot}$  | Inner boundary of the present Solar HZ                      |
| $r_{out\odot}$ | Outer boundary of the present Solar HZ                      |
| $D$            | Distance from the Earth to the star                         |
| $K_*$          | Amplitude of radial velocity signal                         |
| $\Delta TOA$   | Change in time-of-arrival in pulsar timing technique        |
| $\alpha_a$     | Variation in the sky position in astrometry technique       |
| $ESI$          | Earth Similarity Index                                      |
| $\varrho$      | ESI planetary properties                                    |
| $\varrho_0$    | ESI terrestrial reference value                             |
| $w$            | ESI weight exponent   |

*Continued on next page*

*Continued from previous page*

| <b>Parameter</b> | <b>Definition</b>                              |
|------------------|--|
| $\tau_{p-m}$     | Torque between planet and moon                 |
| $T_{p-m}$        | Total life time of a moon                      |
| $k_{2p}$         | Tidal Love number of the planets               |
| $Q_p$            | Tidal dissipation parameter                    |
| $n_p$            | Angular velocity of the planet's rotation      |
| $n_m$            | Angular velocity of the moon's orbit           |
| $a_{crit}$       | Critical semi-major axis                       |
| rmf              | Rock mass fraction                             |
| $\chi$           | Pearson product moment correlation coefficient |

# Appendix B

## Program

```
#Author: Supachai Awiphan (supachai.awiphan@student.manchester.ac.uk)
#Project: The detectability of habitable exomoons with Kepler
#University: University of Manchester
#Degree: MSc by Research (Astronomy and Astrophysics)
#Programming Language: Python 2.4
```

```
import string
import random
import numpy as np
import scipy as sp
import matplotlib as mpl
from scipy import integrate
from scipy.optimize import fsolve
from scipy.stats import pearsonr
```

```
""" ***** """
```

```
#Unit conversion
```

```
#AU to metres
```

```
def AUtoM ( AU ) :
    metreAU = ( 1.49597870700e11 ) * AU
    return metreAU
```

```
#Metres to AU
```

```
def MtoAU ( metreAU ) :
    AU = metreAU / ( 1.49597870700e11 )
    return AU
```

```
#Earth radius to metres
```

```
def RetoM ( Re ) :
```

```
    metreRe = ( 6371.00e3 ) * Re
    return metreRe

#Solar radius to metres
def RstoM ( Rs ) :
    metreRs = ( 6.955e8 ) * Rs
    return metreRs

#Earth mass to kilograms
def MetoKg ( earthMass ) :
    kgEarth = ( 5.9722e24 ) * earthMass
    return kgEarth

#Kilograms to Earth mass
def KgtoMe ( kgEarth ) :
    earthMass = kgEarth / ( 5.9722e24 )
    return earthMass

#Solar mass to kilograms
def MstoKg ( sunMass ) :
    kgSun = ( 1.988415861e30 ) * sunMass
    return kgSun

#Kilograms to solar mass
def KgtoMs ( kgSun ) :
    sunMass = kgSun / ( 1.988415861e30 )
    return sunMass

#Days to seconds
def daytoSec ( day ) :
    sec = day * 86400.0
    return sec

#Seconds to days
def sectoDay ( sec ) :
    day = sec / ( 86400.0 )
    return day

#Years to seconds
def yeartoSec ( year ) :
    sec = year * 86400.0 * 365.24222
    return sec

#Seconds to years
def sectoYear ( sec ) :
```

```

    year = sec / ( 86400.0 * 365.24222 )
    return year

#Degrees to radians
def degtoRad ( deg ) :
    rad = deg * 2. * np.pi / 360.
    return rad

#Speed of light in vacuum
c = 2.99792458e8
#Gravitational constant
G = 6.67428e - 11

""" ***** """

#Math function

#Elliptic integral of first kind
def K ( k ) :
    result = integrate.quad ( lambda x: 1. / ( np.sqrt ( 1. - k * k * np.sin ( x ) * np.sin ( x ) ) ) , 0., np.pi / 2. )
    return result [ 0 ]

#Elliptic integral of second kind
def E ( k ) :
    result = integrate.quad ( lambda x: np.sqrt ( 1. - k * k * np.sin ( x ) * np.sin ( x ) ) , 0., np.pi / 2. )
    return result [ 0 ]

#Elliptic integral of thrid kind
def PI ( n, k ) :
    result = integrate.quad ( lambda x: 1. / ( ( 1. - n * np.sin ( x ) * np.sin ( x ) ) * np.sqrt ( 1. - k * k * np.sin
( x ) * np.sin ( x ) ) ) , 0., np.pi / 2. )
    return result [ 0 ]

#Heaviside Step Function
def heaviside ( x ) :
    if x < 0:
        result = 0.
    elif x = 0:
        result = 0.5
    elif x > 0:
        result = 1.
    return result

""" ***** """

#Mandel&Algol 2002

```

```

#Mandel&Algol 2002 model
def modelMA ( z, p, gamma1, gamma2, zSP ) :
    c1 = 0.
    c2 = gamma1 + 2. * gamma2
    c3 = 0.
    c4 = - gamma2

    c0 = 1. - c1 - c2 - c3 - c4
    ohmega = c0 / ( 0. + 4. ) + c1 / ( 1. + 4. ) + c2 / ( 2. + 4. ) + c3 / ( 3. + 4. ) + c4 / ( 4. + 4. )

    a = ( z - p ) * ( z - p )
    b = ( z + p ) * ( z + p )
    k = np.sqrt ( ( 1. - a ) / 4. / z / p )
    q = p * p - z * z
    k1 = np.arccos ( ( 1. - p * p + z * z ) / 2. / z )
    k0 = np.arccos ( ( p * p + z * z - 1. ) / 2. / p / z )

#Evaluating lam_e
if 1 + p < z:
    lam_e = 0.
elif abs ( 1 - p ) < z and z <= 1 + p:
    lam_e = ( 1 / np.pi ) * ( p * p * k0 + k1 - 0.5 * np.sqrt ( 4. * z * z - ( 1. + z * z - p * p ) * ( 1. + z * z -
p * p ) ) )
elif z <= 1 - p:
    lam_e = p * p
elif z <= p - 1.:
    lam_e = 1.

#Evaluating lam_d and eta_d
#Case1
if z >= 1. + p:
    lam_d = 0.
    eta_d = 0.
elif p = 0.:
    lam_d = 0.
    eta_d = 0.

#Case2
elif z > 0.5 + abs ( p - 0.5 ) and z < 1. + p:
    lam_d = lam1 ( p, z, a, b, k, q )
    eta_d = eta1 ( p, z, a, b, k1, k0 )

#Case3
elif p < 0.5 and z > p and z < 1. - p:
    lam_d = lam2 ( p, z, a, b, k, q )
    eta_d = eta2 ( p, z )

```

```

#Case4
elif p < 0.5 and z = 1. - p:
    lam_d = lam5 ( p )
    eta_d = eta2 ( p, z )

#Case5
elif p < 0.5 and z = p:
    lam_d = lam4 ( p, k )
    eta_d = eta2 ( p, z )

#Case6
elif p = 0.5 and z = 0.5:
    lam_d = 1. / 3. - 4. / ( np.pi * 9. )
    eta_d = 3. / 32.

#Case7
elif p > 0.5 and z = p:
    lam_d = lam3 ( p, k )
    eta_d = eta1 ( p, z, a, b, k1, k0 )

#Case8
elif p > 0.5 and z >= abs ( 1. - p ) and z < p:
    lam_d = lam1 ( p, z, a, b, k, q )
    eta_d = eta1 ( p, z, a, b, k1, k0 )

#Case9
elif p < 1. and z > 0. and z <= 0.5 - abs ( p - 0.5 ) :
    lam_d = lam2 ( p, z, a, b, k, q )
    eta_d = eta2 ( p, z )

#Case10
elif p < 1. and z = 0.:
    lam_d = lam6 ( p )
    eta_d = eta2 ( p, z )

#Case11
elif p > 1. and z <= p - 1.:
    lam_d = 0.
    eta_d = 0.5

if zSP >= 0.:
    fluxModel = 1. - 1. / ( 4. * ohmega ) * ( ( 1. - c2 ) * lam_e + c2 * ( lam_d + 2. / 3. * heaviside ( p - z )
) - c4 * eta_d )
else:
    fluxModel = 1.

return fluxModel

#Mandel&Algol 2002 definition
def lam1 ( p, z, a, b, k, q ) :
    lam = 1. / ( 9. * np.pi * np.sqrt ( p * z ) ) * ( ( ( 1. - b ) * ( 2. * b + a - 3. ) - 3. * q * ( b - 2. ) ) * K ( k )
+ 4. * p * z * ( z * z + 7. * p * p - 4. ) * E ( k ) - 3. * q / a * PI ( ( a - 1. ) / a, k ) )

```

```

return lam

def lam2 ( p, z, a, b, k, q ) :
    lam = 2. / ( 9. * np.pi * np.sqrt ( 1. - a ) ) * ( ( 1. - 5. * z * z + p * p + q * q ) * K ( 1. / k ) + ( 1. - a ) *
( z * z + 7. * p * p - 4. ) * E ( 1. / k ) - 3. * q / a * PI ( ( a - b ) / a, 1. / k ) )
    return lam

def lam3 ( p, k ) :
    lam = 1. / 3. + 16. * p / 9. / np.pi * ( 2. * p * p - 1. ) * E ( 1. / 2. / k ) - ( 1. - 4. * p * p ) * ( 3. - 8. * p
* p ) / 9. / np.pi / p * K ( 1. / 2. / k )
    return lam

def lam4 ( p, k ) :
    lam = 1. / 3. + 2. / 9. / np.pi * ( 4. * ( 2. * p * p - 1. ) * E ( 2. * k ) + ( 1. - 4. * p * p ) * K ( 2. * k ) )
    return lam

def lam5 ( p ) :
    lam = 2. / 3. / np.pi * np.arccos ( 1. - 2. * p ) - 4. / 9. / np.pi * ( 3. + 2. * p - 8. * p * p )
    return lam

def lam6 ( p ) :
    lam = - 2. / 3. * np.sqrt ( ( 1. - p * p ) * ( 1. - p * p ) * ( 1. - p * p ) ) ;
    return lam

def eta1 ( p, z, a, b, k1, k0 ) :
    eta1 = 1. / 2. / np.pi * ( k1 + 2. * eta2 ( p, z ) * k0 - 1. / 4. * ( 1. + 5. * p * p + z * z ) * np.sqrt ( ( 1. - a
) * ( b - 1. ) ) )
    return eta1

def eta2 ( p, z ) :
    eta2 = p * p / 2. * ( p * p + 2. * z * z )
    return eta2

""" ***** """

#Kipping 2011

#Kipping 2011 model
def modelKP ( sP, sM, sPM, p, s, gamma1, gamma2, fluxModel, zSP ) :

    c1 = 0.
    c2 = gamma1 + 2. * gamma2
    c3 = 0.
    c4 = - gamma2
    c0 = 1. - c1 - c2 - c3 - c4

```

```

ohmega = c0 / ( 0. + 4. ) + c1 / ( 1. + 4. ) + c2 / ( 2. + 4. ) + c3 / ( 3. + 4. ) + c4 / ( 4. + 4. )
if zSP >= 0.:
    #Case1, 2, 3, 10, 11, 12, 19, 20, 21
    if sM >= s + 1.:
        fluxModel = fluxModel
    elif sM > 1. - s and sM < 1. + s:
        #Case4, 5, 6
        if sP >= p + 1.:
            AreaM = alpha ( 1., s, sM )
            FM = FII ( c1, c2, c3, c4, sM, s )
            AM = AII ( sM, s, AreaM )
            fluxModel = fluxModel - AM * FM
        elif sP > 1. - p and sM < 1. + p:
            #Case13
            if sPM >= p + s:
                AreaM = alpha ( 1., s, sM )
                FM = FII ( c1, c2, c3, c4, sM, s )
                AM = AII ( sM, s, AreaM )
                fluxModel = fluxModel - AM * FM
            #Case14 Fewell Case
            elif sPM > p - s and sPM < p + s:
                #Intersection12
                x12 = ( 1. - p * p + sP * sP ) / ( 2. * sP )
                y12 = 1. / ( 2. * sP ) * np.sqrt ( 2. * sP * sP * ( 1. + p * p ) - ( 1 - p * p ) * ( 1 - p
* p ) - sP * sP * sP * sP )
                #Intersection13
                x13a = ( 1. - s * s + sM * sM ) / ( 2. * sM )
                y13a = - 1. / ( 2. * sM ) * np.sqrt ( 2. * sM * sM * ( 1. + s * s ) - ( 1 - s * s ) * ( 1 -
s * s ) - sM * sM * sM * sM )
                cos13a = ( sP * sP + sM * sM - sPM * sPM ) / ( 2. * sP * sM )
                sin13a = np.sqrt ( 1 - cos13a * cos13a )
                x13 = x13a * cos13a - y13a * sin13a
                y13 = x13a * sin13a + y13a * cos13a
                #Intersection23
                x23a = ( p * p - s * s + sPM * sPM ) / ( 2. * sPM )
                y23a = 1. / ( 2. * sPM ) * np.sqrt ( 2. * sPM * sPM * ( p * p + s * s ) - ( p * p - s *
s ) * ( p * p - s * s ) - sPM * sPM * sPM * sPM )
                cos23a = - ( sP * sP + sPM * sPM - sM * sM ) / ( 2. * sP * sPM )
                sin23a = np.sqrt ( 1 - cos23a * cos23a )
                x23 = x23a * cos23a - y23a * sin23a + sP
                y23 = x23a * sin23a + y23a * cos23a

            #Condition 1
            if ( x12 - sM * cos13a ) * ( x12 - sM * cos13a ) + ( y12 + sM * sin13a ) * ( y12 + sM
* sin13a ) < s * s:

```

```

#Condition 2
if sP > 1:
    Alpha1 = alpha ( 1., s, sM )
    Alpha2 = alpha ( 1., p, sP )
    AreaM = Alpha1 - Alpha2
    FM = FII ( c1, c2, c3, c4, sM, s )
    AM = AII ( sM, s, AreaM )
    fluxModel = fluxModel - AM * FM
else:
    Alpha1 = alpha ( 1., s, sM )
    Alpha2 = alpha ( 1., p, sP )
    Alpha3 = alpha ( p, s, sPM )
    AreaM = np.pi * p * p + Alpha1 - Alpha2 - Alpha3
    FM = FII ( c1, c2, c3, c4, sM, s )
    AM = AII ( sM, s, AreaM )
    fluxModel = fluxModel - AM * FM
else:
#Condition 3
if ( x12 - sM * cos13a ) * ( x12 - sM * cos13a ) + ( y12 - sM * sin13a ) * ( y12 -
sM * sin13a ) < s * s:
    cord1 = np.sqrt ( ( x12 - x13 ) * ( x12 - x13 ) + ( y12 - y13 ) * ( y12 - y13 ) )
    cord2 = np.sqrt ( ( x12 - x23 ) * ( x12 - x23 ) + ( y12 - y23 ) * ( y12 - y23 ) )
    cord3 = np.sqrt ( ( x13 - x23 ) * ( x13 - x23 ) + ( y13 - y23 ) * ( y13 - y23 ) )
    r1 = 1.
    r2 = p
    r3 = s
#Condition 4
if sM * sin13a > y13 + ( y23 - y13 ) / ( x23 - x13 ) * ( sM * cos13a - x13 ) :
    AreaOverlapA = 1. / 4. * np.sqrt ( ( cord1 + cord2 + cord3 ) * ( - cord1
+ cord2 + cord3 ) * ( cord1 - cord2 + cord3 ) * ( cord1 + cord2 - cord3 ) ) + r1 * r1 * np.arcsin ( cord1 / 2. / r1
) + r2 * r2 * np.arcsin ( cord2 / 2. / r2 ) + r3 * r3 * np.arcsin ( cord3 / 2. / r3 ) - cord1 / 4. * np.sqrt ( 4. * r1
* r1 - cord1 * cord1 ) - cord2 / 4. * np.sqrt ( 4. * r2 * r2 - cord2 * cord2 ) - cord3 / 4. * np.sqrt ( 4. * r3 * r3 -
cord3 * cord3 )

    AreaM = alpha ( 1., s, sM ) - AreaOverlapA
    FM = FII ( c1, c2, c3, c4, sM, s )
    AM = AII ( sM, s, AreaM )
    fluxModel = fluxModel - AM * FM
else:
    AreaOverlapB = 1. / 4. * np.sqrt ( ( cord1 + cord2 + cord3 ) * ( - cord1
+ cord2 + cord3 ) * ( cord1 - cord2 + cord3 ) * ( cord1 + cord2 - cord3 ) ) + r1 * r1 * np.arcsin ( cord1 / 2. / r1
) + r2 * r2 * np.arcsin ( cord2 / 2. / r2 ) + r3 * r3 * np.arcsin ( cord3 / 2. / r3 ) - cord1 / 4. * np.sqrt ( 4. * r1
* r1 - cord1 * cord1 ) - cord2 / 4. * np.sqrt ( 4. * r2 * r2 - cord2 * cord2 ) + cord3 / 4. * np.sqrt ( 4. * r3 * r3 -
cord3 * cord3 )

    AreaM = alpha ( 1., s, sM ) - AreaOverlapB
    FM = FII ( c1, c2, c3, c4, sM, s )

```

```

        AM = AII ( sM, s, AreaM )
        fluxModel = fluxModel - AM * FM
    else:
        #Condition 5
        if ( x13 - sP ) * ( x13 - sP ) + y13 * y13 < p * p:
            #Condition 6
            if ( sM - s ) < ( sP - p ) :
                Alpha1 = alpha ( p, s, sPM )
                AreaM = np.pi * s * s - Alpha1
                FM = FII ( c1, c2, c3, c4, sM, s )
                AM = AII ( sM, s, AreaM )
                fluxModel = fluxModel - AM * FM
            else:
                fluxModel = fluxModel
        else:
            #Condtion 7
            if ( x23 * x23 ) + ( y23 * y23 ) < 1.:
                Alpha1 = alpha ( 1., s, sM )
                Alpha2 = alpha ( p, s, sPM )
                AreaM = Alpha1 - Alpha2
                FM = FII ( c1, c2, c3, c4, sM, s )
                AM = AII ( sM, s, AreaM )
                fluxModel = fluxModel - AM * FM
            else:
                AreaM = alpha ( 1., s, sM )
                FM = FII ( c1, c2, c3, c4, sM, s )
                AM = AII ( sM, s, AreaM )
                fluxModel = fluxModel - AM * FM

#Case15
    else:
        fluxModel = fluxModel
else:
    #Case22
    if sPM >= p + s:
        AreaM = alpha ( 1., s, sM )
        FM = FII ( c1, c2, c3, c4, sM, s )
        AM = AII ( sM, s, AreaM )
        fluxModel = fluxModel - AM * FM

    #Case23
    elif sPM > p - s and sPM < p + s:
        Alpha1 = alpha ( 1., s, sM )
        Alpha2 = alpha ( p, s, sPM )
        AreaM = Alpha1 - Alpha2
        FM = FII ( c1, c2, c3, c4, sM, s )
        AM = AII ( sM, s, AreaM )

```

```

        fluxModel = fluxModel - AM * FM
    #Case24
    else:
        fluxModel = fluxModel
else:
    #Case7, 8, 9
    if sP >= p + 1.:
        if sM > s:
            AreaM = np.pi * s * s
            FM = FIII ( c1, c2, c3, c4, sM, s )
            AM = AIII ( sM, s, AreaM )
            fluxModel = fluxModel - AM * FM
        else:
            AreaM = np.pi * s * s
            FM = FIX ( c1, c2, c3, c4, sM, s )
            AM = AIX ( sM, s, AreaM )
            fluxModel = fluxModel - AM * FM
    elif sP > 1. - p and sM < 1. + p:
        #Case16
        if sPM >= p + s:
            if sM > s:
                AreaM = np.pi * s * s
                FM = FIII ( c1, c2, c3, c4, sM, s )
                AM = AIII ( sM, s, AreaM )
                fluxModel = fluxModel - AM * FM
            else:
                AreaM = np.pi * s * s
                FM = FIX ( c1, c2, c3, c4, sM, s )
                AM = AIX ( sM, s, AreaM )
                fluxModel = fluxModel - AM * FM
        #Case17
        elif sPM > p - s and sPM < p + s:
            if sM > s:
                Alpha1 = alpha ( p, s, sPM )
                AreaM = np.pi * s * s - Alpha1
                FM = FIII ( c1, c2, c3, c4, sM, s )
                AM = AIII ( sM, s, AreaM )
                fluxModel = fluxModel - AM * FM
            else:
                Alpha1 = alpha ( p, s, sPM )
                AreaM = np.pi * s * s - Alpha1
                FM = FIX ( c1, c2, c3, c4, sM, s )
                AM = AIX ( sM, s, AreaM )
                fluxModel = fluxModel - AM * FM
    #Case18

```

```

else:
    fluxModel = fluxModel
else:
    #Case25
    if sPM >= p + s:
        if sM > s:
            AreaM = np.pi * s * s
            FM = FIII ( c1, c2, c3, c4, sM, s )
            AM = AIII ( sM, s, AreaM )
            fluxModel = fluxModel - AM * FM
        else:
            AreaM = np.pi * s * s
            FM = FIX ( c1, c2, c3, c4, sM, s )
            AM = AIX ( sM, s, AreaM )
            fluxModel = fluxModel - AM * FM
    #Case26
    elif sPM > p - s and sPM < p + s:
        if sM > s:
            Alpha1 = alpha ( p, s, sPM )
            ka0 = kappa0 ( p, s, sPM )
            ka1 = kappa1 ( p, s, sPM )
            ka2 = kappa2 ( p, s, sPM )
            AreaM = np.pi * s * s - Alpha1
            FM = FIII ( c1, c2, c3, c4, sM, s )
            AM = AIII ( sM, s, AreaM )
            fluxModel = fluxModel - AM * FM
        else:
            Alpha1 = alpha ( p, s, sPM )
            AreaM = np.pi * s * s - Alpha1
            FM = FIX ( c1, c2, c3, c4, sM, s )
            AM = AIX ( sM, s, AreaM )
            fluxModel = fluxModel - AM * FM
    #Case27
    else:
        fluxModel = fluxModel

return fluxModel

#Kipping 2011 definition
def alpha ( R, r, S ) :
    alpha = r * r * kappa0 ( R, r, S ) + R * R * kappa1 ( R, r, S ) - kappa2 ( R, r, S )
    return alpha

def kappa0 ( R, r, S ) :
    kappa0 = np.arccos ( ( S * S + r * r - R * R ) / ( 2. * S * r ) )
    return kappa0

```

```

def kappa1 ( R, r, S ) :
    kappa1 = np.arccos ( ( S * S + R * R - r * r ) / ( 2. * S * R ) )
    return kappa1

def kappa2 ( R, r, S ) :
    kappa2 = np.sqrt ( ( 4. * S * S * R * R - ( R * R + S * S - r * r ) * ( R * R + S * S - r * r ) ) / 4. )
    return kappa2

def FII ( c1, c2, c3, c4, sM, s ) :
    resulta = integrate.quad ( lambda r: 2. * r * ( 1 - c1 - c2 - c3 - c4 ) + 2. * r * c1 * np.power ( 1. - r * r, 0.25 )
    ) + 2. * r * c2 * np.power ( 1. - r * r, 0.5 ) + 2. * r * c3 * np.power ( 1. - r * r, 0.75 ) + 2. * r * c4 * ( 1. - r *
    r ) , ( sM - s ) , 1 )
    FII = resulta [ 0 ]
    FII = FII / ( 1. - c1 / 5. - 2. * c2 / 6. - 3. * c3 / 7. - 4. * c4 / 8. )
    return FII

def FIII ( c1, c2, c3, c4, sM, s ) :
    resulta = integrate.quad ( lambda r: 2. * r * ( 1 - c1 - c2 - c3 - c4 ) + 2. * r * c1 * np.power ( 1. - r * r, 0.25 )
    ) + 2. * r * c2 * np.power ( 1. - r * r, 0.5 ) + 2. * r * c3 * np.power ( 1. - r * r, 0.75 ) + 2. * r * c4 * ( 1. - r *
    r ) , ( sM - s ) , ( sM + s ) )
    FIII = resulta [ 0 ]
    FIII = FIII / ( 1. - c1 / 5. - 2. * c2 / 6. - 3. * c3 / 7. - 4. * c4 / 8. )
    return FIII

def FIX ( c1, c2, c3, c4, sM, s ) :
    resulta = integrate.quad ( lambda r: 2. * r * ( 1 - c1 - c2 - c3 - c4 ) + 2. * r * c1 * np.power ( 1. - r * r, 0.25 )
    ) + 2. * r * c2 * np.power ( 1. - r * r, 0.5 ) + 2. * r * c3 * np.power ( 1. - r * r, 0.75 ) + 2. * r * c4 * ( 1. - r *
    r ) , 0, ( sM + s ) )
    FIX = resulta [ 0 ]
    FIX = FIX / ( 1. - c1 / 5. - 2. * c2 / 6. - 3. * c3 / 7. - 4. * c4 / 8. )
    return FIX

def AII ( sM, s, AreaM ) :
    am = ( sM - s ) * ( sM - s )
    AII = AreaM / ( np.pi * ( 1 - am ) )
    return AII

def AIII ( sM, s, AreaM ) :
    am = ( sM - s ) * ( sM - s )
    bm = ( sM + s ) * ( sM + s )
    AIII = AreaM / ( np.pi * ( bm - am ) )
    return AIII

def AIX ( sM, s, AreaM ) :

```

```

bm = ( sM + s ) * ( sM + s )
AIX = AreaM / ( np.pi * bm )
return AIX

```

```

""" ***** """

```

### **#Insturmental flux**

```

def magCal ( flux, mag, instru, n ) :
    if instru = 1:          #Euclid VIS
        t = 540.
        pixel = ( 0.1 * 3 ) * ( 0.1 * 3 )
        zeroPoint = 25.58
        readoutN = 4.5
        thermalN = 0
        darkN = 0.00056
        bias = 380
        back = 21.5
    if instru = 2:          #Euclid NISP Y
        t = 90.
        pixel = ( 0.3 * 3 ) * ( 0.3 * 3 )
        zeroPoint = 24.25
        readoutN = 7.5
        thermalN = 0.26
        darkN = 0.1
        bias = 380
        back = 21.3
    if instru = 3:          #Euclid NISP J
        t = 90.
        pixel = ( 0.3 * 3 ) * ( 0.3 * 3 )
        zeroPoint = 24.29
        readoutN = 7.5
        thermalN = 0.02
        darkN = 0.1
        bias = 380
        back = 21.3
    if instru = 4:          #Euclid NISP H
        t = 54.
        pixel = ( 0.3 * 3 ) * ( 0.3 * 3 )
        zeroPoint = 24.92
        readoutN = 9.1
        thermalN = 0.02
        darkN = 0.1
        bias = 380
        back = 21.4

```

```

if instru = 5:          #Kepler
    t = 1765.5
    pixel = ( 3.98 * 5 ) * ( 3.98 * 5 )
    backN = 334.
    zeroPoint = 25.1
    readoutN = 95.
    thermalN = 0.
    darkN = 0.25
    bias = 700.
    fluxMag = np.power ( 10., - 0.4 * ( mag - zeroPoint ) ) * t
if instru < 5:
    fluxNoise = np.random.poisson ( np.sqrt ( np.power ( 10., -0.4 * ( mag - zeroPoint ) ) * t + np.power (10.
, -0.4 * ( back - zeroPoint ) ) * pixel * t + readoutN *9. + thermalN * t * 9. + darkN * t * 9. ) , 1 )
    flux = ( flux * fluxMag ) + fluxNoise + bias
if instru = 5:
    fluxNoise = np.random.poisson ( np.sqrt ( np.power ( 10., - 0.4 * ( mag - zeroPoint ) ) * t + readoutN +
thermalN * t + darkN * t * 25 + backN * t, 1)
    flux = ( flux * fluxMag ) + fluxNoise + bias
return flux

```

"""" \*\*\*\*\* """"

### Main program

#### #Input file

```

print "\n ***** \nFile\n ***** "
fileName = raw_input ( "Input file name\t\t: " )

```

```

data = np.loadtxt ( fileName, skiprows = 0 )

```

#### #Star Mass ( Ms )

```

massS = data [ :, 0 ]

```

#### #Planet Mass ( Me )

```

massP = data [ :, 1 ]

```

#### #Planet Period ( Day )

```

periodP = data [ :, 2 ]

```

#### #Star Radius ( Rs )

```

radiusS = data [ :, 3 ]

```

#### #Planet Radius ( Re )

```

radiusP = data [ :, 4 ]

```

#### #Planet Eccentricity

```

eccP = data [ :, 5 ]

```

#### #Planet Inclination ( Degree )

```

incP = data [ :, 6 ]

```

#### #Planet Argument of periapsis ( Degree )

```

argP = data [ :, 7 ]
#Planet Ascending node ( Degree )
ascP = data [ :, 8 ]
#Limb darkening 1
gamma1 = data [ :, 9 ]
#Limb darkening 2
gamma2 = data [ :, 10 ]
#Moon Mass ( Me )
massM = data [ :, 11 ]
#Moon Period ( Day )
periodM = data [ :, 12 ]
#Moon Radius ( Day )
radiusM = data [ :, 13 ]
#Moon Eccentricity
eccM = data [ :, 14 ]
#Moon Inclination ( Degree )
incM = data [ :, 15 ]
#Moon Argument of periapsis ( Degree )
argM = data [ :, 16 ]
#Moon Ascending node ( Degree )
ascM = data [ :, 17 ]
#Magnitude
mag = data [ :, 18 ]
#Instrument
instru = data [ :, 19 ]

#Number of data
n = 50000

#Observe time ( Day )
ObsTime = 1000

#Default value
flux = np.zeros ( n )
mAnoP = np.zeros ( n )
tAnoP = np.zeros ( n )
mAnoM = np.zeros ( n )
tAnoM = np.zeros ( n )
rSB = np.zeros ( n )
rPB = np.zeros ( n )
rMB = np.zeros ( n )
xSM = np.zeros ( n )
ySM = np.zeros ( n )
zSM = np.zeros ( n )
xSP = np.zeros ( n )

```

```

ySP = np.zeros ( n )
zSP = np.zeros ( n )
sP = np.zeros ( n )
sM = np.zeros ( n )
sPM = np.zeros ( n )
Z = np.zeros ( n )
fluxN = np.zeros ( n )

#Time generate ( Day )
time = np.linspace ( 0.0, ObsTime, n )

#Find semimajor axis ( m )
semiMajP = sp.power ( ( ( ( MstoKg ( massS ) + MetoKg ( massP ) ) * G * daytoSec ( periodP ) * daytoSec (
periodP ) ) / ( 4 * np.pi * np.pi ) ) , float ( 1 ) / 3 )
semiMajM = sp.power ( ( ( ( MetoKg ( massP ) + MetoKg ( massM ) ) * G * daytoSec ( periodM ) * daytoSec (
periodM ) ) / ( 4 * np.pi * np.pi ) ) , float ( 1 ) / 3 )

for i in range ( massS.size ) :

    #Radius ratio
    p = RetoM ( radiusP [ i ] ) / RstoM ( radiusS [ i ] )
    s = RetoM ( radiusM [ i ] ) / RstoM ( radiusS [ i ] )

    #Random initial planet phase and find planet phase
    rand1 = random.random ( )
    epochP = time / periodP [ i ] + rand1
    phaseP = epochP%1.
    Mp = phaseP * 2. * np.pi

    #Random initial moon phase and find moon phase
    rand2 = random.random ( )
    epochM = time / periodM [ i ] + rand2
    phaseM = epochM%1.
    Mm = phaseM * 2. * np.pi

    for j in range ( n ) :

        #Solve mean anomaly from phase
        mAnoPFunc = lambda x: x - eccP [ i ] * np.sin ( x ) - Mp [ j ]
        mAnoP [ j ] = fsolve ( mAnoPFunc, Mp [ j ] )
        tAnoP [ j ] = 2. * np.arctan ( np.sqrt ( ( 1. + eccP [ i ] ) / ( 1. - eccP [ i ] ) ) * np.tan ( mAnoP [ j ] / 2. ) )

        #Solve mean anomaly from phase
        mAnoMFunc = lambda x: x - eccM [ i ] * np.sin ( x ) - Mm [ j ]
        mAnoM [ j ] = fsolve ( mAnoMFunc, Mm [ j ] )

```

```

tAnoM [j] = 2. * np.arctan ( np.sqrt ( ( 1. + eccM [i] ) / ( 1. - eccM [i] ) ) * np.tan ( mAnoM [j] / 2. ) )

#Find star, planet and moon positions
rSB [j] = ( semiMajP [i] * ( 1. - eccP [i] * eccP [i] ) ) / ( 1. + eccP [i] * np.cos ( tAnoP [j] ) )
rMB [j] = ( semiMajM [i] * ( 1. - eccM [i] * eccM [i] ) ) / ( 1. + eccM [i] * np.cos ( tAnoM [j] ) )
rPB [j] = ( rMB [j] * massM [i] ) / massP [i]

xSM [j] = rSB [j] * np.cos ( tAnoP [j] + degtoRad ( argP [i] ) ) + rMB [j] * np.cos ( tAnoM [j] + degtoRad ( argM [i] ) ) * np.cos ( degtoRad ( argP [i] ) + degtoRad ( ascM [i] ) ) - rMB [j] * np.sin ( degtoRad ( incM [i] ) ) * np.sin ( tAnoM [j] + degtoRad ( argM [i] ) ) * np.sin ( degtoRad ( argP [i] ) + degtoRad ( ascM [i] ) )

ySM [j] = rSB [j] * np.cos ( degtoRad ( incP [i] ) ) * np.sin ( tAnoP [j] + degtoRad ( argP [i] ) ) - rMB [j] * np.sin ( degtoRad ( incP [i] ) ) * np.cos ( degtoRad ( incM [i] ) ) * np.sin ( tAnoM [j] + degtoRad ( argM [i] ) ) + rMB [j] * np.cos ( degtoRad ( incP [i] ) ) * np.sin ( degtoRad ( incM [i] ) ) * np.sin ( tAnoM [j] + degtoRad ( argM [i] ) ) * np.cos ( degtoRad ( argP [i] ) + degtoRad ( ascM [i] ) ) + rMB [j] * np.cos ( degtoRad ( incP [i] ) ) * np.cos ( tAnoM [j] + degtoRad ( argM [i] ) ) * np.sin ( degtoRad ( argP [i] ) + degtoRad ( ascM [i] ) )

zSM [j] = rSB [j] * np.sin ( degtoRad ( incP [i] ) ) * np.sin ( tAnoP [j] + degtoRad ( argP [i] ) ) + rMB [j] * np.cos ( degtoRad ( incP [i] ) ) * np.sin ( degtoRad ( incM [i] ) ) * np.sin ( tAnoM [j] + degtoRad ( argM [i] ) ) + rMB [j] * np.sin ( degtoRad ( incP [i] ) ) * np.sin ( degtoRad ( incM [i] ) ) * np.sin ( tAnoM [j] + degtoRad ( argM [i] ) ) * np.cos ( degtoRad ( argP [i] ) + degtoRad ( ascM [i] ) ) + rMB [j] * np.sin ( degtoRad ( incP [i] ) ) * np.cos ( tAnoM [j] + degtoRad ( argM [i] ) ) * np.sin ( degtoRad ( argP [i] ) + degtoRad ( ascM [i] ) )

xSP [j] = rSB [j] * np.cos ( tAnoP [j] + degtoRad ( argP [i] ) ) - rPB [j] * np.cos ( tAnoM [j] + degtoRad ( argM [i] ) ) * np.cos ( degtoRad ( argP [i] ) + degtoRad ( ascM [i] ) ) + rPB [j] * np.sin ( degtoRad ( incM [i] ) ) * np.sin ( tAnoM [j] + degtoRad ( argM [i] ) ) * np.sin ( degtoRad ( argP [i] ) + degtoRad ( ascM [i] ) )

ySP [j] = rSB [j] * np.cos ( degtoRad ( incP [i] ) ) * np.sin ( tAnoP [j] + degtoRad ( argP [i] ) ) + rPB [j] * np.sin ( degtoRad ( incP [i] ) ) * np.cos ( degtoRad ( incM [i] ) ) * np.sin ( tAnoM [j] + degtoRad ( argM [i] ) ) - rPB [j] * np.cos ( degtoRad ( incP [i] ) ) * np.sin ( degtoRad ( incM [i] ) ) * np.sin ( tAnoM [j] + degtoRad ( argM [i] ) ) * np.cos ( degtoRad ( argP [i] ) + degtoRad ( ascM [i] ) ) - rPB [j] * np.cos ( degtoRad ( incP [i] ) ) * np.cos ( tAnoM [j] + degtoRad ( argM [i] ) ) * np.sin ( degtoRad ( argP [i] ) + degtoRad ( ascM [i] ) )

zSP [j] = rSB [j] * np.sin ( degtoRad ( incP [i] ) ) * np.sin ( tAnoP [j] + degtoRad ( argP [i] ) ) - rPB [j] * np.cos ( degtoRad ( incP [i] ) ) * np.sin ( degtoRad ( incM [i] ) ) * np.sin ( tAnoM [j] + degtoRad ( argM [i] ) ) - rPB [j] * np.sin ( degtoRad ( incP [i] ) ) * np.sin ( degtoRad ( incM [i] ) ) * np.sin ( tAnoM [j] + degtoRad ( argM [i] ) ) * np.cos ( degtoRad ( argP [i] ) + degtoRad ( ascM [i] ) ) - rPB [j] * np.sin ( degtoRad ( incP [i] ) ) * np.cos ( tAnoM [j] + degtoRad ( argM [i] ) ) * np.sin ( degtoRad ( argP [i] ) + degtoRad ( ascM [i] ) )

sM [j] = np.sqrt ( xSM [j] * xSM [j] + ySM [j] * ySM [j] ) / RstoM ( radiusS [i] )
sP [j] = np.sqrt ( xSP [j] * xSP [j] + ySP [j] * ySP [j] ) / RstoM ( radiusS [i] )
sPM [j] = np.sqrt ( ( xSP [j] - xSM [j] ) * ( xSP [j] - xSM [j] ) + ( ySP [j] - ySM [j] ) * ( ySP [j] - ySM [j] ) ) / RstoM ( radiusS [i] )

#Planetary transit component

```

```

flux [ j ] = modelMA ( sP [ j ] , p, gamma1 [ i ] , gamma2 [ i ] , zSP [ j ] )

#Moon transit component
flux [ j ] = modelKP ( sP [ j ] , sM [ j ] , sPM [ j ] , p, s, gamma1 [ i ] , gamma2 [ i ] , flux [ j ] , zSP [ j ] )

#Add instrument noise ( Kepler )
flux [ j ] = magCal ( flux [ j ] , mag [ i ] , instru [ i ] , n )

#Find median of flux
fluxMedian = np.median ( flux )

#Find number of data in each transit event
period = periodP [ i ]
nTransit = int ( ObsTime / period ) + 1
nDataTransit = int ( period * n / ObsTime )

#Find new ephemeris from O - C diagram
tFlux = np.zeros ( 3 )
tTime = np.zeros ( 3 )
minSlope = np.zeros ( nTransit )
maxSlope = np.zeros ( nTransit )
igTime = np.zeros ( nTransit )
egTime = np.zeros ( nTransit )

shift = 0

for j in range ( nTransit ) :
    if j < nTransit - 1:
        for k in range ( nDataTransit - 3 ) :
            for l in range ( 3 ) :
                tFlux [ l ] = flux [ j * nDataTransit + shift + k + 1 ]
                tTime [ l ] = time [ j * nDataTransit + shift + k + 1 ]
            fitPara = np.polyfit ( tTime, tFlux, 1 )
            slope = fitPara [ 0 ]
            if slope > maxSlope [ j ] :
                maxSlope [ j ] = slope
                egTime [ j ] = ( fluxMedian - fitPara [ 1 ] ) / fitPara [ 0 ]
            elif slope < minSlope [ j ] :
                minSlope [ j ] = slope
                igTime [ j ] = ( fluxMedian - fitPara [ 1 ] ) / fitPara [ 0 ]
        if ( j + 1 ) * nDataTransit + shift < n and ( j ) * nDataTransit + shift > 0:
            if abs ( time [ ( j + 1 ) * nDataTransit + shift ] - egTime [ j ] ) < 5. * ObsTime / n:
                shift = shift + 5
            elif abs ( - time [ ( j ) * nDataTransit + shift ] + igTime [ j ] ) < 5. * ObsTime / n:
                shift = shift - 5

```

```

    if j = nTransit - 1:
        nTransit = nTransit - 1

tt = np.zeros ( nTransit )
td = np.zeros ( nTransit )

for j in range ( nTransit ) :
    tt [ j ] = ( egTime [ j ] + igTime [ j ] ) / 2.
    td [ j ] = egTime [ j ] - igTime [ j ]

for j in range ( nTransit - 1 ) :
    tt [ j + 1 ] = tt [ j + 1 ] - ( j + 1 ) * period - tt [ 0 ]

tt [ 0 ] = 0.

ep = range ( nTransit )
fitParafit = np.polyfit ( ep, tt, 1 )
period = period + fitParafit [ 0 ]

#Find new number of data in each transit event
nTransit = int ( ObsTime / period ) + 1
nDataTransit = int ( period * n / ObsTime )

#Find TTV and TDV signals
tFlux = np.zeros ( 3 )
tTime = np.zeros ( 3 )
minSlope = np.zeros ( nTransit )
maxSlope = np.zeros ( nTransit )
igTime = np.zeros ( nTransit )
egTime = np.zeros ( nTransit )

for j in range ( nTransit ) :
    if j < nTransit - 1:
        for k in range ( nDataTransit - 3 ) :
            for l in range ( 3 ) :
                tFlux [ l ] = flux [ j * nDataTransit + k + 1 ]
                tTime [ l ] = time [ j * nDataTransit + k + 1 ]
                fitPara = np.polyfit ( tTime, tFlux, 1 )
                slope = fitPara [ 0 ]
                if slope > maxSlope [ j ] :
                    maxSlope [ j ] = slope
                    egTime [ j ] = ( fluxMedian - fitPara [ 1 ] ) / fitPara [ 0 ]
                elif slope < minSlope [ j ] :
                    minSlope [ j ] = slope

```

```

igTime [ j ] = ( fluxMedian - fitPara [ 1 ] ) / fitPara [ 0 ]

if j = nTransit - 1:
    nTransit = nTransit - 1

tt = np.zeros ( nTransit )
td = np.zeros ( nTransit )

for j in range ( nTransit ) :
    tt [ j ] = ( egTime [ j ] + igTime [ j ] ) / 2. - ( j ) * period
    td [ j ] = egTime [ j ] - igTime [ j ]

avgtt = tt.mean ( )
avgtd = td.mean ( )

for j in range ( nTransit ) :
    tt [ j ] = tt [ j ] - avgtt
    td [ j ] = td [ j ] - avgtd

#Find correlation
r = sum ( ( tt * tt - sum ( tt * tt ) / nTransit ) * ( td * td - sum ( td * td ) / nTransit ) ) / np.sqrt ( sum ( (
tt * tt - sum ( tt * tt ) / nTransit ) * ( tt * tt - sum ( tt * tt ) / nTransit ) ) * sum ( ( td * td - sum ( td * td ) /
nTransit ) * ( td * td - sum ( td * td ) / nTransit ) ) )

#Output
print "\n ***** \nSystem information\n ***** \n"
print "Star mass\t", massS [ i ]
print "Planet mass\t", massP [ i ]
print "Moon mass\t", massM [ i ]
print "Planet period\t", periodP [ i ]
print "Moon period\t", periodM [ i ]
print "Correlation coefficients:\t", r

```